UNIVERSITY OF SOUTHAMPTON

FACULTY OF SCIENCE, ENGINEERING & MATHEMATICS

Optoelectronics Research Centre

Direct UV-Written Waveguide Devices

by

Faisal Rafiq Mahamd Adikan

Thesis for the degree of Doctor of Philosophy

June 2007

UNIVERSITY OF SOUTHAMPTON

ABSTRACT

Optoelectronics Research Centre

Doctor of Philosophy

Direct UV-Written Waveguide Devices

Faisal Rafiq Mahamd Adikan

This thesis describes a series of experimental studies concerning waveguide structures based on the direct UV and direct grating writing fabrication techniques. The latter approach allows simultaneous definition of waveguide structures and Bragg gratings.

The first result of this work describes the fabrication and characterisation of small angle X-couplers that exhibit low polarisation and wavelength dependence. Maximum and minimum coupling ratios of 95% (±0.8%) and 1.9% (±1%) respectively with typical excess loss of 1.0dB (±0.5dB) were recorded. Device modelling using Beam Propagation Method (BPM) and an analytical model showed good agreement with experimental results over a broad crossing angle and wavelength range.

By introducing refractive index asymmetry in 2° X-couplers, it was possible to tune the response to give a 50:50 coupling ratio. Multiple UV exposure experiments investigated the ‘proximity effect’ and provided further proof of the ability of UV writing to produce raised waist index X-couplers.

A first order Bragg grating electrically tunable via liquid crystal index modification with a maximum tunability of 141 GHz at 1562nm (TM polarised) and 114 GHZ at 1561.8nm (TE polarised) using electro-patterned ITO-coated glass electrodes is also presented. The 141GHz tuning range effectively covers up to five 25 GHz WDM channel spacing and was achieved with 170Vpp sinusoidal 1 kHz supply voltage. Hysteretic behaviour of the tuning curves was observed and is believed to be related to the dynamics of the disclination line formed along the waveguide axis with increase or decrease in supply voltage.

Finally, a description of the successful demonstration of UV-written single channels, y-splitters, and Bragg gratings into a novel flat fibre substrate is provided. Utilising a series of Bragg gratings enabled assessment of the core layer uniformity and birefringence.

Contents

Abstract i

Fire Related Issues ii

Acknowledgments iii

1 Introduction 1

1.1 Thesis Structure 3

References 6

2 Integrated Optics 7

2.1 Planar Waveguides: Device Functions & Applications 10

    2.1.1 Next Generation Technologies? 12

2.2 S-bends, X-couplers & Bragg Gratings: Applications 13

2.3 Summary 16

References 18

3 Fabrication of Silica-Based Planar Waveguide Devices 21

3.1 Planar Deposition Techniques 23

    3.1.1 Thermal Oxidation 24

    3.1.2 Sol Gel 25

    3.1.3 Plasma Enhanced Chemical Vapour Deposition (PECVD) 26

    3.1.4 Flame Hydrolysis Deposition (FHD) 27

3.2 Waveguide Definition Techniques 30

    3.2.1 Photolithography & Etching 30

    3.2.2 Ion Exchange 31

    3.2.3 Femtosecond Direct Writing 32

3.3 Direct UV Writing 32

3.4 Summary 35

References 36

4 Photosensitivity 39

4.1 Photosensitivity Mechanism 40

4.2 Photosensitivity Dynamics 43

4.3 Photosensitivity Enhancement 44

4.3.1 Stability Issues …… 45
4.4 Summary …… 47
References …… 48

5 Waveguide, X-coupler & Bragg Grating Theory 50
5.1 The Slab Waveguide …… 50
5.1.1 Marcatili Method …… 57
5.1.2 Effective Index Method …… 59
5.1.3 Beam Propagation Method …… 60
5.2 Analytical Model for Direct UV Written X-couplers …… 62
5.3 Bragg Grating Theory …… 67
5.4 Summary …… 70
References …… 71

6 Small Angle X-couplers 73
6.1 S-bends …… 73
6.1.1 Experiment …… 78
6.1.2 Results & Discussion …… 79
6.2 Small Angle X-couplers …… 82
6.2.1 Analytical & BPM Modelling …… 84
6.2.2 Experiment …… 86
6.2.3 Results & Discussion …… 87
6.3 Tuning of Coupling Ratio via Asymmetry …… 90
6.3.1 Experiment …… 90
6.3.2 Results & Discussion …… 90
6.4 Summary …… 92
References …… 93

7 Bragg Gratings as an Assessment Tool 95
7.1 Producing the Bragg Grating …… 95
7.2 Experiment …… 99
7.3 Results & Discussion …… 100
7.4 Proximity Effect …… 102
7.5 Summary …… 105
References …… 107

8 Tunable Bragg Gratings via a Liquid Crystal Overlay 108
8.1 Liquid Crystals …………………………………………………………………. 110
8.2 Device Assembly ……………………………………………………………….. 112
8.3 Experiment ……………………………………………………………………… 114
8.4 Results & Discussion …………………………………………………………… 116
8.5 Anomalous Polarisation Behaviour ……………………………………………….. 119
8.6 Effect of Supply Voltage Waveform …………………………………………… 122
8.7 Effect of Power Supply Frequency ……………………………………………... 122
8.8 Electrode Offset …………………………………………………………….... 123
8.9 Thermal Effects ……………………………………………………………..... 124
8.10 Applications …………………………………………………………………… 126
8.11 Summary ………………………………………………………………………..... 126
References ……………………………………………………………………….. 128

9 Flat Fibre Technology 130
9.1 MCVD Process ……………………………………………………………... 131
9.2 Making the Flat Fibre ……………………………………………………………. 132
9.3 Adding Waveguide Structures ………………………………………………… 134
9.4 Propagation Loss Measurement – Experiment ……………………………….... 135
    9.4.1 Results & Discussion ………………………………………………….. 136
9.5 Substrate Analysis via Bragg Gratings …………………………………….... 138
9.6 Summary ………………………………………………………………………. 140
References ……………………………………………………………………….. 142

10 Conclusions & Future Work 143
10.1 Future Work …………………………………………………………………… 144
References ……………………………………………………………………….. 148

Appendix A ORC FHD System Upgrade i
Appendix B FHD In Malaysia vi
List of Publications xi

Journal Papers

Flat Fibre Patent Application

Awards

i. House of Common Engineering 2006 Section Prize
ii. SPIE Educational Scholarship Award 2004

Magazine Excerpts & Journal Appearance

i. Flat Fibre in Materials World

ii. Flat Fibre in The Engineer

iii. Interview appearance in Nature Photonics

The People

List of Tables

Chapter 2 Integrated Optics Page
2.1 Materials technology for integrated optical devices. 8
2.2 Typical optical or waveguide parameters of the various materials. 9
2.3 An example of the photonics value chain. 10

Chapter 3 Fabrication of Silica Based Planar Waveguide Devices
3.1 Summary of effect of dopants relative to pure silica. 29
3.2 DUW/DGW parameters and the corresponding device characteristics. 35

Chapter 6 Small Angle X-couplers
6.1 Comparison between various X-coupler experimental studies. 83

Chapter 7 Bragg Gratings as an Assessment Tool
7.1 FHD substrate specifications. 99
7.2 Absolute index increase for a given fluence level. 101

Chapter 8 Tunable Grating via Liquid Crystal Overlay
8.1 Nematic LC BDH 18523 specifications. 112

Constants

Symbol	Name	Value (unit)
μ_0	Magnetic permeability of free space	$4\pi \times 10^{-7}$ (H/m)
ε_0	Electric permittivity of free space	8.85×10^{-12} (F/m)
h	Planck’s constant	6.63×10^{-34} (m^2 kg/s)
eV	Electron volt	1.60×10^{-19} (joules)
c	Speed of light in vacuum	2.99×10^{8} (m/s)

Chemical Names

SiO_2:Si	silica-on-silicon
$LiNbO_3$	lithium niobate
InGaAs	indium gallium arsenide
InP	indium phosphide
$SiCl_4$	silicon tetrachloride
$GeCl_4$	germanium tetrachloride

List of Figures

Chapter 2 Integrated Optics Page

2.1 Three types of planar waveguides: (a) rib, (b) ridge, and (c) buried. 10
2.2 (a) S-bend in a buried channel configuration, with the core layer sandwiched between two cladding layers; (b) Occurrence of transition and radiation (or bend) loss due to a curved waveguide. 13
2.3 (a) Schematic of X-coupler; (b) β is the crossing angle. 14
2.4 Schematic of three main functions of X-couplers: (a) power coupler; (b) 50% power splitter; (c) passive crossover. 14
2.5 Illustration of periodic refractive index perturbation in a channel waveguide, forming a grating structure. 15
2.6 Illustration of the operational properties of a reflection grating. 16

Chapter 3 Fabrication of Silica Based Planar Waveguide Devices

3.1 Schematic and photo of three layer silica-on-silicon sample. 23
3.2 Thin film deposition process steps. 23
3.3 Summary of sol gel processing. 25
3.4 PECVD deposition chamber and process schematic. 26
3.5 Schematic and photo of the deposition step of FHD. 28
3.6 The etching method process flow. 30
3.7 An illustration of (a) direct UV writing set up; (b) direct grating writing set up; (c) interference pattern generated by the crossed beam; (d) photo of direct grating writing. 33

Chapter 4 Photosensitivity

4.1 An illustration showing the tetrahedral structure of silica. 41
4.2 Colour centre model photosensitivity mechanism. 42

Chapter 5 Waveguide, X-coupler & Bragg Grating Theory

5.1 (a) Reflection and refraction at a plane interface, (b) light propagation in an index structure via total internal reflection (TIR) with evanescent field extending into the cladding layers. 51
5.2 Slab waveguide indicating a transverse field distribution E_y. z is direction of propagation. 52
5.3 Graphical solutions to equations [5.29] and [5.30]. 56
5.4 Marcatili's depiction of a channel waveguide index profile. 57
5.5 (a) Graphical solution of transcendental equation [5.37], (b) effect of asymmetry on the dispersion relationship for the fundamental TE mode. 60
5.6 Obtaining the effective index of the core by successively implementing the Effective Index method onto the various slab waveguides. 61
5.7 Schematic representation of the X-coupler and various supermodes. 63
5.8 Examples of calculated supermode field distribution. 66
5.9 (a) Output powers as a function of crossing angle; (b) output powers as a function of normalised profile height h ($\beta = 1°$). 67
5.10 Reflection spectra versus normalised wavelength (λ/λmax) for uniform gratings with various κL values. 70

Chapter 6 Small Angle X-couplers

6.1 A schematic showing various s-bend parameters. 74
6.2 (a) Cosine bend governed by $f(x) = (D/2)\ (1-\cos(\pi x/L))$; (b) the continuously varying curvature of the cosine bend. 77
6.3 Graphs showing modelled results of pure bend loss and transition losses using measured waveguide parameters. 77
6.4 Illustration of the main elements of an experimental set up for s-bend loss 78

measurements.
6.5 Optimised launch into channel waveguide with some scattered light in the slab waveguide as viewed by the IR camera situated along the output end of the sample. 79
6.6 Fibre-to-fibre loss with respect to s-bend curve radius. 80
6.7 X-coupler parameters. 82
6.8 Examples of BPM simulation of 1° crossing angle X-couplers with various waist index values. 85
6.9 Microscope and surface profiler images of a UV written X-coupler that has been etched to reveal the device structure. 86
6.10 Coupling ratio behaviour with respect to X-coupler crossing angle. 87
6.11 Wavelength dependencies of X-couplers for 3 different crossing angles. 88
6.12 Typical through and coupled power spectrum showing intensity dips at around 1370, 1480 and 1600nm. 89
6.13 Graph showing the coupling ratio against crossing angle using polarised input light, highlighting the low polarisation dependence of the structure. 89
6.14 A schematic representation of the fabricated UV written X-couplers with 2° crossing angle. 90
6.15 Coupling ratio and insertion loss of X-couplers with various second s-bend UV writing fluence values highlighting the effects of index asymmetry of the structure (solid and dotted lines: for indicative purpose only). 91
6.16 Wavelength dependencies of asymmetric X-couplers. 92

Chapter 7 Bragg Gratings as Assessment Tool

7.1 Schematic of the Direct Grating Writing technique. 96
7.2 Graph showing (a) reflection and (b) transmission spectra of a series of 1mm gratings direct UV-written with UV beam power of 50mW and 50% duty cycle. 98
7.3 Illustration of the experimental set up to assess planar Bragg grating reflection spectra. 99
7.4 Effective indexes versus UV writing fluence. Sample used: DN423/1. 100
7.5 Experimental layout of UV-written Bragg gratings and the previously defined channels for proximity effect characterisation (d: waveguide width). 103
7.6 Example of the gratings' reflection spectra used for the proximity effect experiment. 103
7.7 Effective indexes at various spacing and fluence values. 104
7.8 Normalised profile height, *h* versus UV writing fluence. 105

Chapter 8 Tunable Grating via Liquid Crystal Overlay

8.1 Illustration of the molecular order in a nematic liquid crystal. 110
8.2 Illustration of (a) homeotropic and (b) homogeneous alignment. 111
8.3 Refractive index of the LC18523 with temperature at λ=1550nm (taken from [20]). 112
8.4 A schematic representation of the assembled device showing the liquid crystal overlay in between the electro-patterned ITO electrodes and the waveguide containing Bragg gratings. 114
8.5 Photographs showing the HeNe scattering footprint of an etched segment of the sample containing planar Bragg gratings viewed from the top of the sample. 115
8.6 Device tuning curves for both TM and TE polarised light showing hysteresis between points A and B. 116
8.7 Grating reflection spectra at the two threshold points for increasing voltage values. 117
8.8 Grating spectrum observed in reflection with the fitted Lev-Mar curves shown. 118
8.9 Disclination line dynamics with applied voltage seen via 90° cross polarisers (data was taken from experiments by Benjamin Snow). 119
8.10 Schematic depiction of expected LC alignment at initial and final voltage states, showing the anticipated refractive index 'seen' by TM and TE polarised light. 120
8.11 Transmission images from the output facet of the LC device at different instances during the increasing voltage sequence with TE polarised input light. 121
8.12 λ_B shift for TE polarised input at low voltages. 121
8.13 TE tuning curve with various supply voltage waveform. 122
8.14 A graph showing the effect of supply voltage frequency on tuning range. 123
8.15 HeNe scattering from the waveguide showing non-optimised electrode position 123

(offset).
8.16 Graph showing the effect of electrode position with respect to waveguide on the tunability of the device. 124
8.17 Graphs showing λ_B as a function of temperature for: (a) experimental set up under room temperature conditions, (b) thermal behaviour of the assembly. 125
8.18 Effect of applying voltage across ITO electrodes at random points and duration along the experimental run, indicating that very little thermal effect is taking place. 126

Chapter 9 Flat Fibre Technology

9.1 Schematic representation of the preform fabrication stage of MCVD. 131
9.2 Schematic representation of the fibre drawing stage of MCVD. 132
9.3 (a) Cross section; and (b) perspective views of the novel flat fibre sample. 133
9.4 Extended lengths of the flexible glass planar substrate. 134
9.5 Image captures of (a) straight channel waveguide and (b) the two output arms of 100µm y-splitters, both illuminated at λ = 633nm. 134
9.6 Photographs of the pigtailed assembly for propagation loss measurements. 136
9.7 Schematic diagram of the optical set up for free space and fibre coupled propagation loss measurement. 136
9.8 Cutback loss measurement results relating detected transmitted light to flat fibre length (curves with broken lines represent the linear fit). 137
9.9 SEM image of the core of the flat fibre with the arrow pointing to the boundary where the layers meet. 137
9.10 First demonstration of Bragg reflection in a flat fibre sample. The inset shows the ASE spectra of the input light and the Bragg gratings reflection. 138
9.11 Mean effective refractive index variation across the cross section of the sample core layer. 139
9.12 Birefringence of the flat fibre core layer with mean birefringence of ~$3.3\text{x}10^{-4}$. 140

Chapter 10 Conclusions & Future Work

10.1 (a) Waveguide dimensions generated from red luminescence study, (b) detection of green and red luminescence that complement each other along the UV beam path. 145
10.2 (a) Bubble switch architecture employing X-coupler and groove geometry. (b) A distributed stress/strain sensor where the peak Bragg wavelength (and possibly the reflection amplitude) of the gratings is modified by applying force onto the waist region of the X-coupler. 146
10.3 Conceptual depiction of a fully flexible flat fibre distributed sensor. 147

Appendix A ORC FHD System Upgrade

A.1 Schematic representation of the FHD system. ii
A.2 Corrosion in the FHD chamber. iii
A.3 Top view of gas piping and electrical connections of the new FHD chamber control box. iv, v

Appendix B FHD In Malaysia

B.1 Various defects/pores found on the fabricated 3-layer samples. vii
B.2 (a) HeNe set up for NA measurements and mode profiling, and (b) shows a typical mode profile of a waveguide with the data generated by the HeNe curve fitting program. viii, ix
B.3 Numerical aperture of UV written channels with increasing UV writing fluence levels. x

Abbreviations

AOM	Acousto-optic Modulator
ASE	Amplified Spontaneous Emission
BPM	Beam Propagation Method
CTE	Coefficient of Thermal Expansion
CVD	Chemical Vapour Deposition
DBR	Distributed Bragg Reflector
DFB	Distributed Feedback
DGW	Direct Grating Writing
DTI	Department of Trade & Industry
DUW	Direct UV Writing
DWDM	Dense Wavelength Division Multiplexing
EDFA	Erbium Doped Fibre Amplifier
EDWA	Erbium Doped Waveguide Amplifier
FBG	Fibre Bragg Grating
FHD	Flame Hydrolysis Deposition
GODC	Germanium Oxygen Deficient Centre
IP	Internet Protocol
IR	Infrared
ISP	Internet Service Provider
LC	Liquid Crystal
LED	Light Emitting Diode
LEV-MAR	Levenberg-Marquardt
MCVD	Modified Chemical Vapour Deposition
MFC	Mass Flow Controller
MMI	Multimode Interference
MOST	Media Oriented Systems Transport
MUX	Multiplexer
NOV	Neutral Oxygen Vacancy
OADM	Optical Add Drop Multiplexer
OSA	Optical Spectrum Analyser
OVD	Outside Vapour Deposition
PECVD	Plasma Enhanced Chemical Vapour Deposition
PL	Photoluminescence
ROADM	Reconfigurable Optical Add Drop Multiplexer
SEM	Scanning Electron Microscopy
UV	Ultraviolet
VoIP	Voice Over IP
WDM	Wavelength Division Multiplexing

Acknowledgments

I am honoured to be part of this institution. Working at the Optoelectronics Research Centre has been tremendous and I have greatly enjoyed my stay here. My deepest gratitude goes to my supervisors – Prof. Peter Smith and Dr. Corin Gawith – for their support, advice, understanding, and more importantly, for making the decision to take me on board in the first place.

I am extremely grateful to Dr. James Gates for his part in the later stages of my research. Also, to other members of the group – past and present – Dr. Ian Sparrow, Dr. Gregory Emmerson, Dr. Denis Guilhot, Huw Major, Christopher Holmes, Benjamin Snow, Mario Ramirez, Dr. Samuel Watts, Dr. Lu Ming, and Dr. Dmytro Kundys.

Special thanks to Eve Smith and Dr. Eleanor Tarbox for their part in ensuring that I got everything done on time and efficiently.

I would also like to thank my colleagues at the ORC who have taught me so much, and for their assistance: Dr. Francesco Poletti, Rodrigo Amezcua, Andrew Webb, Dr. Jayanta Sahu, Dr. Neil Broderick, Ed Weatherby, Mark Lessey, Niel Fagan, Simon Butler, Dr. Peter Lanchester, Trevor Austin, Timothy McIntyre, Chris Nash, Kevin Sumner, Prof. David Payne, Neil Sessions, Mukhzeer Shahimin, Robert Simpson, Prof. Rob Eason, Tleyane Sono, and Robert Standish. Also, thank you to Rachel Abbott for her part in promoting the flat fibre.

I am also grateful to Prof. Harith Ahmad, Dr. Christos Riziotis, Dr. Malgosia Kaczmarek, Dr. Andriy Dyadyusha, Dr. Daniel Jaque and Dr. Mohd. Adzir Mahdi.

To my friends in the ORC, the Southampton Malaysian community, my colleagues in the University of Malaya, my wife Mazarisusanty Ibrahim and our two kids, Muaz Rafiq and Maisarah Rafiq, and to my family back home, I thank you. Big thanks to my parents, Mahamd Adikan Hasan and Patimah Ahmed, for their part in shaping me to be the person I am today.

Finally, my gratitude goes to my sponsors – Ministry of Science, Technology, and Innovation (MOSTI), Government of Malaysia, and the University of Malaya (UM), particularly the officers who have been instrumental in ensuring that everything is in order – Mr. Lai Ah Su (UM), Mrs. Rina Haiges (MOSTI), and Mrs. Khairiatun Zin (MOSTI).

Chapter 1

Introduction

The increasingly important role played by optical based technologies in general, and integrated optics in particular, is reflected in recent announcements of governmental backing, and market projections. For example, in 2005, the UK Science and Innovation Minister, Lord Sainsbury, announced a £100 million funding initiative under the Department of Trade and Industry (DTI) Technology Programme. Among the specific areas covered were a number of optical technologies such as next generation lasers, highlighting the field's importance. This recognition of optics was followed by a recent report published by the DTI, aptly titled 'Photonics: A UK strategy for success', in which several strategic recommendations were underlined to advance the industry further, in order to strengthen the UK's position in this important part of the world economy [1]. According to the US-based Optoelectronics Industry Development Association (OIDA), the overall global market growth of optoelectronics components and enabled products grew by the impressive figure of 39% in 2004, spurring heightened research interests [2].

However, with the burst of the Internet 'bubble' in year 2000, the optics industry had been forced to reinvent itself in order to experience and sustain growth by finding new applications for optical based technologies. Industrial analysts agree that the correct strategy lies in both re-examining the current business model, and in finding ways to package and price services more profitably, or to lower capital and operational costs associated with product development, roll-out and maintenance. This approach and the recent initiatives in developing reconfigurable telecommunication networks that would increase both the network's scalability and reach resulted in increased interest in integrated optics technology. One market research report projected an average annual growth of 18% in the global demand and consumption of integrated optical circuits (discrete components), increasing from USD 4.05 billion in 2001 to USD 9.47 billion in 2006 [3]. Such growth is fuelled by the large scale integration (hence increased complexity) offered by integrated optics technology as well as the ability to mass produce compact devices via fully-automated manufacturing as opposed to the labour intensive fibre based conventional alternatives. The 'burst bubble' event, although unfortunate, also fuelled a number of ventures into new markets for optical based technologies including optical sensors.

The concept of integrated optics was first introduced by S.E. Miller in 1969 [4]. It is not difficult to see why the idea was quick to find acceptance, particularly when it has the potential to be analogous to the far-reaching effects microelectronics had on the global market and technological developments. Integrated optics still has a long way to go to achieving this impact, not least in terms of the variety of material systems utilised to achieve a particular functionality. Among the many platforms, the most dominant material for optically passive functionalities that include basic signal routing, power splitting, and wavelength filtering, is silica, which is the same base material that is used for optical fibres.

Silica-based planar devices can be fabricated via numerous techniques (as described in **Chapter 3** of this thesis). One of these is direct UV writing, which was demonstrated as early as 1974 [5], but only later found application in the silica platform in the early 90's [6]. From then onwards, research based on the technique saw a marked increase, with the annual rate of journal publications rising from one in 1993 to sixteen in 2002 [7]. Direct UV writing is analogous to the computer numerical control (CNC) milling machining of metal parts. It involves defining waveguide structures by exposing a photosensitive silica sample to UV light. By translating the sample underneath the focussed UV beam, waveguide structures such as straight channels and y-splitters can be formed. The versatility of the technique was further enhanced by the introduction of the direct grating writing approach, which was developed here in the Optoelectronics Research Centre (ORC) [8]. This latest capability meant that waveguide structures and Bragg gratings could be defined simultaneously, allowing rapid prototyping of novel devices.

This work aims to explore further developments in terms of novel devices based on this in-house direct UV writing technique. A secondary goal has been the use of Bragg gratings in experiments to determine important substrate characteristics. Some of the results presented here stemmed from prior studies performed by my colleagues within the research group (an example being the liquid crystal planar Bragg grating described in **Chapter 9**). During my PhD studies, I have spent 5 weeks in the University of Malaya in Malaysia performing silica-on-silicon deposition while the in-house flame hydrolysis deposition system in the ORC was being upgraded. This was part of our initial plans to extend the capabilities of rare-earth doped devices following the demonstration of a neodymium-doped direct UV-written laser in 2004 [9]. However, progress in deposition studies was abruptly ended by the October 30th Mountbatten fire in 2005 (see **Fire Related Issues** (page ii of this thesis)).

Following on from this unfortunate event, a number of alternative research avenues were sought, and subsequently achieved, mainly by collaborating with research groups within the ORC, and external institutions. The novel flat fibre substrate (**Chapter 9**) resulted from one such collaboration.

1.1 Thesis Structure

I have structured the thesis as follows.

In **Chapter 2** an overview of integrated optics is presented, highlighting the motivation behind the mercurial development of the field as well as the challenges that need to be addressed in order to emulate the successes of electronics. There is a wide array of material system and design approaches that address specific needs such as light generation, passive components and detection. I have provided a brief comparison between these material systems in terms of their fabrication techniques, level of refractive index contrast achievable, and also the specific advantageous attributes displayed by each of them. A number of market reports and projections were also quoted, stressing the ubiquity of the technologies. Following from these, a closer look at practical implementation of the silica-based structures that were investigated in this research was presented. These structures are s-bends, X-couplers, and Bragg gratings. Further elaborations in terms of modelling and experimental work are presented in later chapters (see below).

Chapter 3 provides a review covering substrate fabrication methods and channel definition techniques. The topic covers fabrication methods such as flame hydrolysis deposition, plasma enhanced chemical vapour deposition, and sol-gel. This is followed by a review of channel definition techniques including ion exchange, photolithography and etching, and direct UV writing. Direct UV writing is chosen as our channel definition technique and is exceptionally valuable in device prototyping as the technique requires no masks, does not involve a multi-stage process such as the one via photolithography and etching, and does not need clean room facilities. It does however require the samples to be photosensitive.

The topic of photosensitivity is the subject of **Chapter 4**. The chapter describes the two complementary models that explain the mechanisms leading to photosensitivity – the colour centre model and glass compaction. The point to make here is that much debate is still taking place regarding the exact physical/chemical phenomenon that causes photosensitivity and it is most likely to be due to the combination of all these effects. Knowledge of the exact cause of photosensitivity is important but not crucial for this research as we are primarily interested in utilising this effect for producing waveguide devices. One critical stage that we employ in processing our samples prior to UV writing is hydrogen loading, a low temperature high pressure technique that diffuses hydroxyl species into the glass matrix, allowing an increase in photosensitivity.

Chapter 5 presents theoretical treatment of slab and channel waveguides. Electrical and magnetic field distribution as well as parameters governing single mode operation are obtained via solutions to Maxwell’s equations. This is followed by modelling of waveguide bends, relating bend radius to pure bend loss as well as the calculation of transition losses due to modal mismatches. A brief description of an analytical model of X-couplers, developed by Durr and Renner [10], is also covered in this chapter, where the empirical formula provided in their work was used to compare simulated and measured coupling behaviour of fabricated small angle X-couplers. I have also employed a commercially available beam propagation method simulation suite for the X-coupler work presented in **Chapter 6**. For completeness, a brief description of this technique is provided. **Chapter 5** concludes with a theoretical treatment of Bragg gratings, which were employed in work presented in **Chapters 7**, **8** and **9**.

As mentioned above, **Chapter 6** describes experimental work and analysis of UV-written s-bends and X-couplers. A comparative study on s-bends formed by joining two partial circles (circular s-bends) and cosine bends concludes that the cosine bends systematically display ~0.3dB lower fibre-to-fibre loss to that of the circular bends. This is attributed to transition losses of the circular bends. Following from this result, subsequent experiments involving the s-bend structure, including X-couplers and y-splitters, all utilise the cosine bend.

The fabrication and characterisation of small angle X-couplers is also presented in **Chapter 6**. It is found that direct UV writing is ideal in producing a raised waist index profile, an attribute which is important in ensuring good device performance. Good agreement between modelled and measured data was also obtained, with the X-couplers showing very low polarisation and wavelength sensitivity.

Up to this point, all the UV writing experiments described made use of the single-beam set up, and therefore the devices/structures fabricated do not contain Bragg gratings. In the remainder of this thesis, measurements and devices involving the gratings are described.

Chapter 7 elaborates the use of Bragg gratings as assessment tools. By interrogating the Bragg reflection, we were able to determine a number of sample attributes including photosensitivity. **Chapter 7** also describes the first experimental quantification of proximity effects in UV-written silica-on-silicon, which involves characterising the index increase resulting from multiple UV exposures.

An electrically tunable planar Bragg grating using a liquid crystal overlay is described in **Chapter 8**. A tuning range encompassing at least five 25GHz spaced wavelength division multiplexed channels was achieved by applying 170Vpp across indium tin oxide electrodes. The use of an anisotropic nematic liquid crystal allows the modification of the overall structure's effective index, which in turn is reflected in the peak Bragg wavelength shift. Such a device could be implemented in reconfigurable switching architectures.

I have described our patent-applied-for flat fibre technology in **Chapter 9**. The flat fibre substrate combines the inherent advantages of both standard optical fibres and planar silica-on-silicon. Functional structures including straight channels, y-splitters and Bragg gratings were successfully UV-written through ~ 350μm thick cladding layer. Assessment of the core layer uniformity and the waveguide birefringence were also made.

Chapter 10 concludes this thesis. On-going research based on the devices presented here is also described, along with some suggestions for future work.

Finally, I have also provided a brief description of the effort in upgrading our in-house flame hydrolysis deposition system, and silica-on-silicon deposition work in the Photonics Laboratory at the University of Malaya (Malaysia) in the **Appendix** section of this thesis.

References:

[1] DTI document entitled: "Photonics: A UK strategy for success," 2006.
This document can be obtained from:
http://www.dti.gov.uk/sectors/electronicsit/ukphotonicsstrategy/page30715.html

[2] O. I. D. A. (OIDA), "Opto Market Performs Well in 2004," in *OIDA News*, vol. 14, 2005, p. 1.
This document can be obtained from:
http://www.oida.org/pdfs/oidanews/oidanews0905.pdf

[3] V. Thomson, "Seeing the light – Optoelectronics market focus," in *CHIP*, 2002.

[4] D. Marcuse, *Integrated Optics*, IEEE Press, New York, 1972.

[5] E. A. Chandross, C. A. Pryde, W. J. Tomlinson, and H. P. Weber, "Photolocking-A new technique for fabricating optical waveguide circuits," *Applied Physics Letters*, vol. 24, pp. 72-74, 1974.

[6] M. Svalgaard, C. V. Poulsen, A. Bjarklev, and O. Poulsen, "Direct UV writing of buried singlemode channel waveguides in Ge-doped silica films," *Electronics Letters*, vol. 30, pp. 1401-1403, 1994.

[7] M. Svalgaard, "Direct UV-written integrated optical components," *Optical Fiber Communication Conference (OFC)* 23-27 Feb. 2004, Los Angeles, CA, USA, paper FK2.

[8] G. D. Emmerson, S. P. Watts, C. B. E. Gawith, V. Albanis, M. Ibsen, R. B. Williams, and P. G. R. Smith, "Fabrication of directly UV-written channel waveguides with simultaneously defined integral Bragg gratings," *Electronics Letters*, vol. 38, pp. 1531-1532, 2002.

[9] D. A. Guilhot, G. D. Emmerson, C. B. E. Gawith, S. P. Watts, D. P. Shepherd, R. B. Williams, and P. G. R. Smith, "Single-mode direct-ultraviolet-written channel waveguide laser in neodymium-doped silica on silicon," *Optics Letters*, vol. 29, pp. 947-949, 2004.

[10] F. Durr and H. Renner, "Analytical design of X-couplers," *Journal of Lightwave Technology*, vol. 23, pp. 876-885, 2005.

Chapter 2

Integrated Optics

It can be argued that integrated optics could be as revolutionary to classical optics as microelectronics is to electrical engineering. To date, the technological advancement of the field has resulted in the miniaturisation of traditional bulk optics and the introduction of multi-functional modules. From a historical perspective, the concept of integrated optics was first coined by S.E. Miller in 1969 who foresaw that technologically, integrated optical devices offer long term stability, increased immunity to thermal and environmental influences, and eliminate the alignment issues inherent in bulk or fibre based optics. So significant were the ideas that within three years, the IEEE[1] published a reprint book on integrated optics containing principal ideas and contributions within the field from leading research workers, including Miller. In the book, he remarked that the growing interest in optical integration ran strong and that involvement in the field is 'fruitful professionally and profitable economically' [1]. The argument is that integration is the key towards transforming optics, just as integrated circuits on silicon transformed electronics, thus leading to a larger acceptance of the technology.

Another important motivation fuelling this technological progression lies in the inherent challenges faced in designing electronic circuits that can operate efficiently in the high frequency range offered by optical technologies (in the Tb/s regions). This stems from the frequency dependent attenuation level of metallic conductors that make up the interconnections within these electronic circuits.

It can also be argued that the economic attractiveness of integrated optics lies in the possibility of fully automated mass production. Low cost fabrication methods derived from the well established micro-electronics industry also played a role in expanding the field further. Having said that, there are challenges associated with the technology that offset these advantages such as the complexity of fibre-pigtailing the finished products, which tend to be labour intensive. Increasing the manufacturing yield or throughput of batch

---

[1] IEEE: The Institute of Electrical and Electronics Engineers.

manufactured integrated optical devices is also an issue where current typical yields of current devices tend to be in the region of 50-60% [2].

One of the biggest hurdles to overcome if integrated optics is to emulate the electronics success story is in combining the various material systems currently being used onto a single platform (what is termed as monolithic integration). This stems from the predominantly material specific device functions of optical components such as InGaAs[2] for detectors, $LiNbO_3$[3] for modulators, SiO_2:Si[4] for passive devices and interconnects. One expert suggested that the current state of integration in optics is similar to that of electronics in the 1970s [2]. Table 2.1, derived from reference [3], elucidates the above remarks, and Table 2.2 describes the typical optical characteristics of the various materials.

Table 2.1 Materials technology for integrated optical devices [taken from [3]].

Material	Properties	Fabrication	Advantages	Application
SiO_2:Si	Cheap and versatile fabrication	Thermal oxidation, CVD, or FHD	Versatile, builds from the Microelectronic technology	Passive devices (couplers, MUX), sensors, filters
Lithium niobate	Electro-optic, acousto-optic, non-linear, birefringent	Metallic diffusion, proton exchange	Active control of light, anisotropic	Switches, modulators
III-V compounds (InP, GaAs)	Electro-optic	Epitaxial growth	High level of integration	Detectors
Polymers	Electro-optic, thermo-optic	Spin, dip coating	Wide range of physical properties	Sensors

CVD: chemical vapour deposition; FHD: flame hydrolysis deposition; MUX: multiplexer; InP: indium-phosphide.

In this chapter, a review of the applications of these integrated devices is presented, with the aim of highlighting the breadth and importance of the technology. The emphasis will be, but not exclusively on, those devices that are based on the silica-on-silicon

---

[2] InGaAs: indium gallium arsenide.

[3] $LiNbO_3$: lithium niobate.

[4] SiO_2:Si: silica-on-silicon.

platform. This is the substrate used throughout this work. Needless to say, there are a wide range of components and devices that fall under the term integrated optics, and a similarly wide range of fields in which they are used.

Table 2.2 Typical optical or waveguide parameters of the various materials.

Material (*typical refractive index*)$^+$	**Index contrast** Δn	**Waveguide fabrication**	**Typical propagation loss**	**Refs.**
SiO_2:Si (SiO_2 ~ 1.4 - 1.5, Si ~ 3.3 – 3.5)	5 - 7 (x 10^{-3})	i. photolithography & etching ii. direct UV writing	0.03 - 0.1dB/cm	[4-6]
Lithium niobate ($LiNbO_3$ ~ 2.2)	~ 10^{-3}	i. zinc/titanium in-diffusion ii. proton exchange	0.1 – 1dB/cm	[7]
Indium phosphide (InP ~ 3.3)	Up to 0.1	i. photolithography & etching	> 1dB/cm	[3]
Polymers (n ~ 1.3 – 1.6)	Up to 10^{-3}	i. photolithography & etching ii. laser ablation iii. moulding/embossing	0.01dB/cm (λ= 840nm) 0.1dB/cm (λ = 1550nm)	[8]

$^+$ Typical refractive index values are usually quoted for λ = 633nm.

An abridged version of the table reported in the UK's Department of Trade and Industry (DTI) document [9] describing the photonics value chain, in which integrated optics based solutions play a major role, is shown in Table 2.3. It often helps to classify these integrated optical devices as either optically passive or active devices. Obviously, central to all these technologies is their ability to guide light. This role is performed by planar waveguides, often simply referred to as waveguides. Waveguides not only guide light, but are also required in performing critical operations such as power splitting, and coupling. The terms planar waveguide devices, and planar lightwave circuits are also commonly used to denote integrated optical devices.

Table 2.3 An example of the photonics value chain [taken from [9]].

Materials & Process Equipment	**Components**	**Modules**	**Service Providers**	**Content & Applications**	**Enabled Products**	**End User**
Silica/Silicon	Lasers	LCDs	Telecoms	Telecoms	Computers	Business
GaAs	Fibres	Telecoms	Energy	Surveillance	Phones	Consumer
InP	Filters	LEDs	Medical	Sensing	Cameras	Government
Polymer	Detectors	Solar cell		Entertainment	Lighting	Military
	Mux/Demux	Imaging			Displays	Medical

LCD: liquid crystal display; LED: light emitting diode; ISP: internet service provider; VoIP: voice over internet protocol.

2.1 Planar Waveguides: Device Functions & Applications

There are three main types of waveguides named after their basic structural properties namely rib, ridge, and buried waveguides as illustrated in Fig. 2.1. The physics that dictates light guidance within these waveguides will be further discussed in Chapter 5. But for now it is sufficient to state that the waveguides fulfil the requirements needed to confine and guide light with sufficiently low losses. Most importantly, they have a core refractive index that is higher than the surrounding material (cladding). We use the buried waveguide type throughout this work (Fig. 2.1(c)).

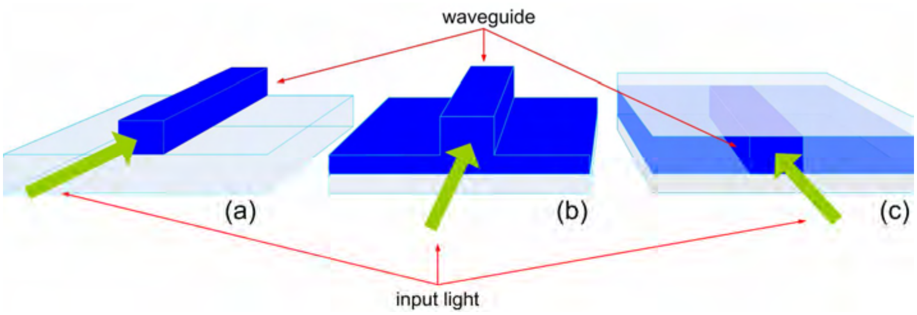

Figure 2.1 Three types of planar waveguides: (a) rib, (b) ridge, and (c) buried.

As mentioned earlier, all three waveguide types perform the same task which is to confine and guide light onto processing blocks or components that execute either optically passive or active functions. Apart from the basic function of confining and guiding light, there exist several other elements or basic functions that serve as building blocks in many optical devices. These are outlined below:

- Interconnects: as the name suggests, these serve to optically connect two points/elements on an optical chip. If there is an offset needed between the two i.e. the two elements are not aligned to each other, then s-bends would be utilised (please refer to Section 2.2). In our case, we refer to these interconnects as channel waveguides.
- Power splitters: these usually split power from a single channel waveguide between two output ones. The simplest form of these elements is commonly referred to as y-splitters (or y-branch) due to their distinct y shape. An extension of this element would have more than two output branches and as such, the term 1xN splitter was adopted for generality where N is the number of output branches. Other similar elements that perform the same task are directional couplers, X-couplers (please refer to Section 2.2), and multimode interference (MMI) couplers.
- Filters/Reflectors: perform the task of reflecting light into a channel waveguide. If the band pass of such a reflector is of a particular wavelength, then this could also be viewed as performing the role of a filter. The simplest implementation of this is by using a mirror. However, a more attractive and widely used technique is by using a grating, which is inherently a wavelength selective element (please refer to Section 2.2).

A more exhaustive list of these basic functions can be found in reference [3].

More often than not, a combination of these functions forms the make-up of a completed device. Optically passive waveguide devices include simple channel waveguides, couplers, attenuators, filters, multiplexers, and 1xN switches. These devices comprise a number of discrete waveguide components with different functionalities integrated into a compact functional module. For example, some optical add/drop multiplexers utilise splitters and gratings. Optically active waveguide devices include planar waveguide lasers and planar waveguide amplifiers, where lasing (stimulated emission) and optical gain are necessary. The ability to integrate multiple functionalities onto a single chip results in modules comprising both optically active and passive waveguide devices such as transparent splitters and combiners [10, 11], distributed feedback lasers (DFB) [12], and multi-wavelength light sources or laser arrays [13, 14]. The emphasis placed on high performance multifunctional optical modules saw the utilisation of spot size converters [15, 16], spatial mode filters [17], gain equalisation filters [18] and waveguide mode lockers [19, 20]. This said, monolithic integration of all the required optically passive and active devices remains a challenge due to the various material-based functionalities, as mentioned earlier.

The telecommunications industry is not the only area where ubiquitous application of integrated optical devices takes place, and this was highlighted in Table 2.3. For example, solutions based on integrated optics such as lab-on-chip and micro-fluidics are now gaining an increasing foothold on the biosensor market, which is forecast to swell to £5.7 billion in 2007, with an annual growth rate of around 10 per cent [21]. In the increasingly important field of defence and homeland security, integrated optical sensors perform the role of detecting chemical and bio-hazardous substances such as anthrax. One of the biggest markets yet is in the consumer electronics and entertainment sector. Light emitting diode lighting, data storage technologies such as DVDs and Blu-ray are a few examples of the technologies found within this sector.

2.1.1 Next Generation Technologies?

Given the myriad developmental activities in the field, this progressive trend is expected to continue well into the next decade. There are a number of recent developments that are making waves within the research community in particular, including:

- Silicon optics: The potential for monolithic integration with microelectronics provides the main thrust in work in this field. Interest in the field grew tremendously following the demonstration of a silicon laser in late 2004 by Bahram Jalali of the University of California [22]. However, optical pumping is still a limitation and efforts in combining electrically pumped laser sources onto a silicon waveguide configuration are under way, including the recent demonstration by Fang et al [23].
- Surface plasmons: As a phenomenon, surface plasmons, which denotes electromagnetic surface waves that have their intensity maximum in the surface and exponentially decaying fields perpendicular to it, were first reported as early as 1957 [24]. Research on the field re-emerged with the advent of fabrication methods and the recent increasingly important role played by sensors, which is where the technology is likely to find wide deployment.

Whether these technologies will find applications in the various industries in the near future is yet to be seen. We will next turn our attention to a few waveguide structures that form an integral part of this research – s-bends, X-couplers, and planar Bragg gratings.

Theoretical treatment and experimental results on these devices are presented in Chapters 5 and 6 respectively.

2.2 S-bends, X-couplers & Bragg gratings: Applications

These simple but important optically passive waveguide structures are incorporated into optical modules to improve performance and in many cases, perform key tasks. S-bends are utilised as spatial mode filters [17] and spot-size converters [25, 26]. In semiconductor lasers, s-bends are used to increase the threshold for the first order mode, preventing multi-mode operation. Swint et al [17] measured an increase of 5-10% in threshold power to that of the conventional straight waveguide by using a cosine s-bend. Spatial mode filters in general exploit the fact that higher order modes have a larger fraction of their mode field propagating outside the core. By increasing loss in that region through higher leakage, higher order modes are attenuated [27]. Waveguide bends introduce transition and radiation (or bend) losses, hence increasing attenuation especially onto weakly confined modes. S-bends also result in distortion of the input field, especially in the outer portion of the curved structure. This leads to mode expansion and is advantageous in countering mode mismatch especially in fibre-waveguide coupling. Suzaki et al [25] employed 70º and 120º tilt angled bent waveguides as spot size converters to provide low optical feedback from the facets of a high gain semiconductor optical amplifier and to improve fibre-coupling efficiency of a 4µm spot size. The abovementioned mechanisms are shown in Fig 2.2.

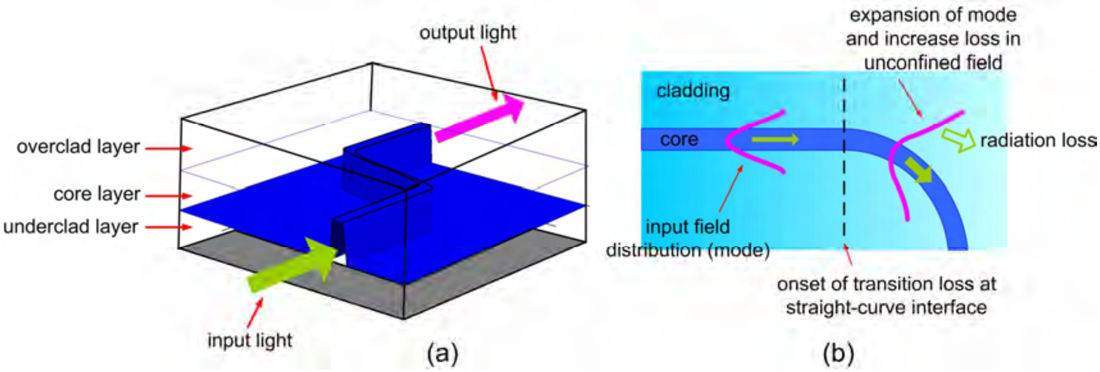

Figure 2.2 (a) S-bend in a buried channel configuration, with the core layer sandwiched between two cladding layers; (b) Occurrence of transition and radiation (or bend) loss due to a curved waveguide.

S-bends are also utilised in variable attenuator designs [28], tailored DFB lasers with chirped gratings [29] and propagation loss characterisation [4]. Tomljenovic-Hanic et al [28] for example, uses thermo-optical effects to effectively change the refractive index profile of an s-bend waveguide to effectively mimic change of effective index due to change in bend radius. The variable buried polymer-based attenuator uses an s-bend with a bend radius of 7mm.

X-couplers provide an important potential route towards increasing chip density. A schematic of an X-coupler is shown in Fig. 2.3. Notice that the structure consists of two intersecting s-bends.

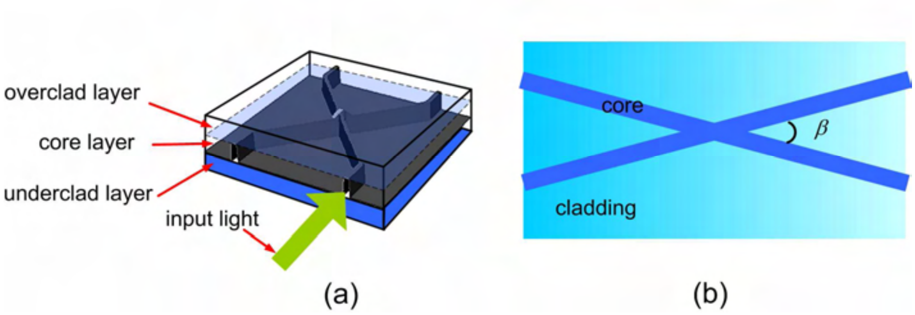

Figure 2.3 (a) Schematic of X-coupler; (b) β is the crossing angle.

The three main functions performed by X-couplers, namely as a power coupler, a 50:50 splitter or as a passive crossing, are depicted in Fig. 2.4. The arrows indicate the power flow from the input waveguide across the structure.

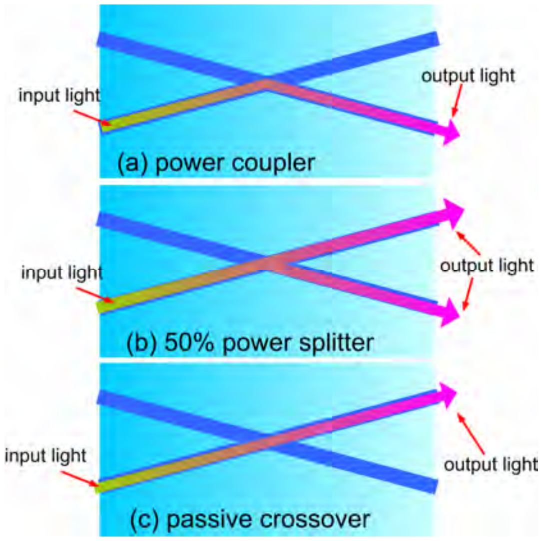

Figure 2.4 Schematic of three main functions of X-couplers: (a) power coupler; (b) 50% power splitter; (c) passive crossover.

Perpendicular intersections between waveguides are common and are frequently employed due to their low crosstalk[5]. However, further increase in chip density could only be achieved if the intersection angles are made smaller [30, 31]. Work by Przyrembel et al [32] on crossed waveguides on a silica-on-silicon sample with 0.7% index difference found that the angles at which low crosstalk values (< -25dB) are attainable, are about a factor of 3 smaller (~5º-8º) than the angles conventionally used (> 20º). The authors used 6μm wide curved waveguides with 10mm curve radius. Modelling work by Agrawal et al [33] on a 2μm wide $LiNbO_3$ waveguide having core and underclad refractive indices of 2.305 and 2.30 respectively also discovered that zero crosstalk occurs at intersecting angles of ~ 5º - 6º. It is also of interest to determine the angles at which near perfect (~100%) power coupling between the excited channel and the passive one can be achieved. This property would be of much use in the design of routing devices such as power couplers, optical add-drop multiplexers (OADM) and switches without the need for a finite interaction length, hence leading towards higher integration. Theoretical and experimental results on UV-written small angle X-couplers are presented in Chapters 5 and 6 respectively.

Another important waveguide structure is the planar Bragg grating, which is a periodic (spatial) perturbation of refractive index along a waveguide, usually along the plane that is orthogonal to the waveguide axis or signal direction [34, 35], as illustrated in Fig. 2.5.

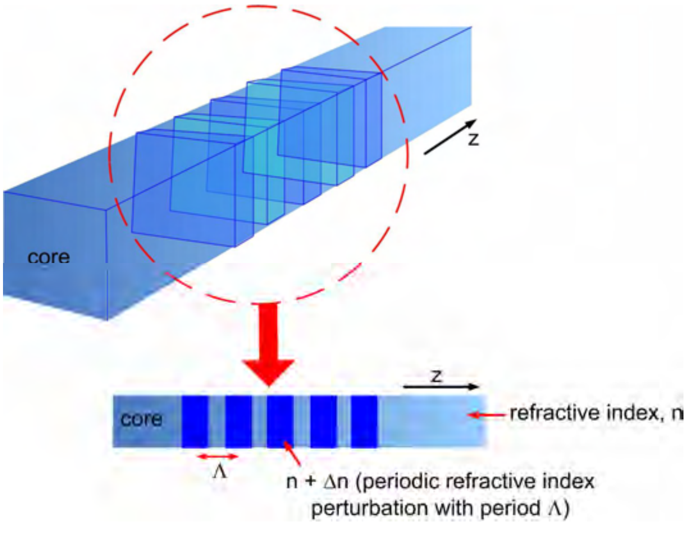

Figure 2.5 Illustration of periodic refractive index perturbation in a channel waveguide, forming a grating structure.

---

[5] Crosstalk in this case is defined as the ratio between the coupled power and the total output power of the device i.e. sum of through and coupled powers. This definition can also be found in Chapter 6 (Table 6.1).

In general, a Bragg grating could be classified as a wavelength selective filter or reflector. It performs the function by coupling the incident mode (usually forward propagating mode) to other modes, whether backward propagating modes (reflection or short-period gratings) or forward propagating modes (transmission or long-period gratings). The coupled modes can be guided, cladding or radiation modes, depending on the design of the grating. A schematic of a reflection grating is shown in Fig. 2.6, illustrating a broadband signal (λ_{broad}) being input into a channel inscribed with a grating structure. The output of the device is the broadband signal with a dip (λ_{broad} - λ_{Bragg}) centred at the Bragg wavelength.

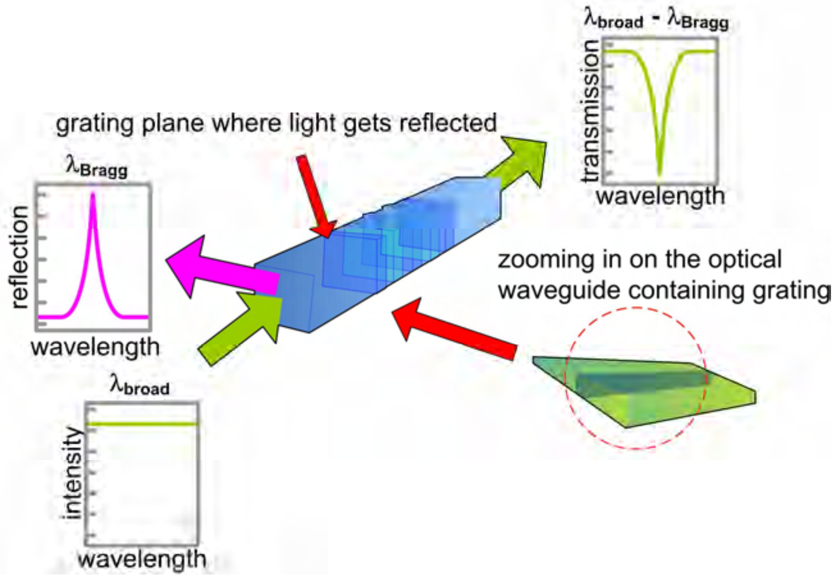

Figure 2.6 Illustration of the operational properties of a reflection grating.

Numerous physical grating parameters can be varied in order to achieve a required spectral response. These include the strength of the induced index change, the length and period of the index perturbation, apodisation and fringe tilt. The types of Bragg gratings are usually determined by the variation of the induced refractive index change along the waveguide axis.

Gratings play a major role in waveguide lasers and amplifiers. They replace reflective mirrors in DFB and DBR configurations, and provide double- or multi-pass capabilities in laser or amplifier configurations.

2.3 Summary

An overview of integrated optics has been presented covering the motivations and challenges faced by engineers in advancing the field. The description has highlighted the value chain of this technology and provided a few examples of integrated optics based solutions. A brief introduction to X-couplers and Bragg gratings, two of the devices that form an integral part of this thesis was also presented.

In the following chapter, a review of how these integrated devices are fabricated will be presented, with a brief treatment of how the technologies that we utilise – direct UV writing – relate to the rest of the field. A closer look as to why silica remains the most suitable substrate for passive optical devices in comparison to other material systems will also be discussed.

References:

[1] D. Marcuse, *Integrated Optics*, IEEE Press, New York, 1972.

[2] This was mentioned by G. Maxwell in his talk during the Centre of Integrated Photonics (CIP) Open Day in 2006. Graeme is currently CIP's Vice President of Hybrid Research & Development. His responsibility includes hybrid integration of active and passive components at CIP, including hybrid device design, planar silica fabrication and assembly of hybrid devices. He is a renowned authority on hybrid integration and PLC technology and was part of the management team that built up the business case to establish CIP.
For a full biography, see: http://www.ciphotonics.com/cip_people_GM.htm

[3] G. Lifante, *Integrated photonics: Fundamentals*: Wiley, England 2003.

[4] Y. Hibino, H. Okazaki, Y. Hida, and Y. Ohmori, "Propagation loss characteristics of long silica-based optical waveguides on 5 inch Si wafers," *Electronics Letters*, vol. 29, pp. 1847-1848, 1993.

[5] N. Takato, K. Jinguji, M. Yasu, H. Toba, and M. Kiwachi, "Silica-based single-mode waveguides on silicon and their application to guided-wave optical interferometers," *Journal of Lightwave Technology*, vol. 6, pp. 1003-1010, 1988.

[6] M. Svalgaard and M. Kristensen, "Directly UV-written silica-on-silicon planar waveguides with low loss," *Electronics Letters*, vol. 33, pp. 861-863, 1997.

[7] L. Ming, "Fabrication and applications of zinc indiffused waveguides in periodically poled lithium niobate," PhD thesis, University of Southampton, 2005.

[8] L. Eldada and L. W. Shacklette, "Advances in polymer integrated optics," *IEEE Journal on Selected Topics in Quantum Electronics*, vol. 6, pp. 54-68, 2000.

[9] DTI document entitled: "Photonics: A UK strategy for success," 2006.
This can be obtained from:
http://www.dti.gov.uk/sectors/electronicsit/ukphotonicsstrategy/page30715.html

[10] Y. Jaouen, L. du Mouza, D. Barbier, J.-M. Delavaux, and P. Bruno, "Eight-wavelength Er-Yb doped amplifier: Combiner/splitter planar integrated module," *IEEE Photonics Technology Letters*, vol. 11, pp. 1105-1107, 1999.

[11] D. Barbier, M. Rattay, F. Saint Andre, G. Clauss, M. Trouillon, A. Kevorkian, J. M. P. Delavaux, and E. Murphy, "Amplifying four-wavelength combiner, based on erbium/ytterbium-doped waveguide amplifiers and integrated splitters," *IEEE Photonics Technology Letters*, vol. 9, pp. 315-317, 1997.

[12] B. K. Das, R. Ricken, and W. Sohler, "Integrated optical distributed feedback laser with Ti:Fe:Er:LiNbO$_3$ waveguide," *Applied Physics Letters*, vol. 82, pp. 1515-17, 2003.

[13] T. Tanaka, Y. Hibino, T. Hashimoto, M. Abe, R. Kasahara, and Y. Tohmori, "100-GHz spacing 8-channel light source integrated with external cavity lasers on planar lightwave circuit platform," *Journal of Lightwave Technology*, vol. 22, pp. 567-573, 2004.

[14] J. Hubner, S. Guldberg-Kjaer, M. Dyngaard, Y. Shen, C. L. Thomsen, S. Balslev, C. Jensen, D. Zauner, and T. Feuchter, "Planar Er- and Yb-doped amplifiers and lasers," *Applied Physics B: Lasers and Optics*, vol. 73, pp. 435-438, 2001.

[15] T. Mizuno, T. Kitoh, M. Itoh, T. Saida, T. Shibata, and Y. Hibino, "Optical spotsize converter using narrow laterally tapered waveguide for planar lightwave circuits," *Journal of Lightwave Technology*, vol. 22, pp. 833-839, 2004.

[16] M. Kohtoku, S. Oku, Y. Kadota, Y. Shibata, and Y. Yoshikuni, "Spotsize converters integrated with deep ridge waveguide structure," *Electronics Letters*, vol. 34, pp. 2403-2404, 1998.

[17] R. B. Swint, T. S. Yeoh, V. C. Elarde, J. J. Coleman, and M. S. Zediker, "Curved Waveguides for Spatial Mode Filters in Semiconductor Lasers," *IEEE Photonics Technology Letters*, vol. 16, pp. 12-14, 2004.

[18] Y. P. Li, C. H. Henry, E. J. Laskowski, C. Y. Mak, and H. H. Yaffe, "Waveguide EDFA gain equalisation filter," *Electronics Letters*, vol. 31, pp. 2005-2006, 1995.

[19] T. Tanaka, H. Takahashi, M. Oguma, T. Hashimoto, Y. Hibino, Y. Yamada, Y. Itaya, J. Albert, and K. O. Hill, "Integrated external cavity laser composed of spot-size converted LD and UV-written grating in silica waveguide on Si," *Electronics Letters*, vol. 32, pp. 1202-1203, 1996.

[20] S. Kawanishi, K. Hattori, H. Takara, M. Oguma, O. Kamatani, and Y. Hibino, "Actively modelocked ring laser using Er-doped silica-based planar waveguide amplifier," *Electronics Letters*, vol. 31, pp. 363-364, 1995.

[21] Biosensor Market, R&D and Commercial Implication www.fuji-keizai.com/e/report/biosensor2004_e.html < 28th September 06>

[22] O. Boyraz and B. Jalali, "Demonstration of a silicon Raman laser," *Optics Express*, vol. 12, pp. 5269-5273, 2004.

[23] A. W. Fang, P. Hyundai, O. Cohen, R. Jones, M. J. Paniccia, and J. E. Bowers, "Electrically pumped hybrid AlGaInAs-silicon evanescent laser," *Optics Express*, vol. 14, pp. 9203-9210, 2006.

[24] H. Raether, *Surface plasmons on smooth and rough surfaces and on gratings*: Springer-Verlag, Germany, 1988.

[25] Y. Suzaki, K. Magari, Y. Kondo, Y. Kawaguchi, Y. Kadota, and K. Yoshino, "High-gain array of semiconductor optical amplifier integrated with bent spot-size

converter (BEND SS-SOA)," *Journal of Lightwave Technology*, vol. 19, pp. 1745-1750, 2001.

[26] J. Salzman, H. Olesen, A. Moller-Larsen, O. Albrektsen, J. Hanberg, J. Norregaard, B. Jonsson, and B. Tromborg, "Distributed feedback lasers with an S-bent waveguide for high-power single-mode operation," *IEEE Journal of Selected Topics in Quantum Electronics*, vol. 1, pp. 346-355, 1995.

[27] K. Takada, M. Oguma, H. Yamada, S. Mitachi, and M. Golling, "Gain distribution measurement of an erbium-doped silica-based waveguide amplifier using a complex OLCR," *IEEE Photonics Technology Letters*, vol. 9, pp. 1102-1103, 1997.

[28] S. Tomljenovic-Hanic and W. Krolikowski, "New design for a variable optical attenuator based on a bent channel waveguide," *Applied Physics B: Lasers and Optics*, vol. 77, pp. 19-23, 2003.

[29] H. Hillmer, A. Grabmaier, S. Hansmann, H. L. Zhu, H. Burkhard, and K. Magari, "Tailored DFB laser properties by individually chirped gratings using bent waveguides," *IEEE Journal of Selected Topics in Quantum Electronics*, vol. 1, pp. 356-362, 1995.

[30] P. Gerard, P. Benech, and R. Rimet, "Intersecting waveguide modelization for any angle and guiding conditions with the radiation spectrum method," *Optics Communications*, vol. 124, pp. 165-174, 1996.

[31] A. Neyer, W. Mevenkamp, L. Thylen, and B. Lagerstrom, "A beam propagation method analysis of active and passive waveguide crossings," *Journal of Lightwave Technology*, vol. T-3, pp. 635-642, 1985.

[32] G. Przyrembel and B. Kuhlow, "Waveguide crossings with low crosstalk at small angles," *Electronics Letters*, vol. 38, pp. 1533-1535, 2002.

[33] N. Agrawal, L. McCaughan, and S. R. Seshadri, "A multiple scattering interaction analysis of intersecting waveguides," *Journal of Applied Physics*, vol. 62, pp. 2187-2193, 1987.

[34] K. O. Hill and G. Meltz, "Fiber Bragg grating technology fundamentals and overview," *Journal of Lightwave Technology*, vol. 15, pp. 1263-1276, 1997.

[35] T. Erdogan, "Fiber grating spectra," *Journal of Lightwave Technology*, vol. 15, pp. 1277-1294, 1997.

Chapter 3

Fabrication of Silica-Based Planar Waveguide Devices

Following from the overview presented in Chapter 2, here we will discuss the various ways in which silica based waveguide devices are fabricated. The first question is: why does silica remain the material of choice when it comes to passive optical devices? The obvious reason is that it is the same material as optical fibres, making the two compatible in many respects. Secondly, silica samples are fabricated using techniques that were derived from the already mature micro-electronics industry, resulting in relatively inexpensive production costs. This is also part of the reason why silica planar samples are fabricated on silicon host substrates, leading to the name silica-on-silicon (SiO_2:Si). In addition to their wide availability, silicon wafers offer the advantages of a high degree of planarity, ready adhesion of deposited silica, have excellent heat dissipation properties and a high melting point (>1400ºC [1]) that enable them to withstand the levels of temperatures involved during deposition/consolidation of the glass layer [2, 3]. Their compatibility with microelectronics also means that they can be utilised as the optical bench on which to mount optoelectronic chips such as laser diodes and detectors, and then couple these to the silica waveguide ends [4]. Apart from silicon, fused silica wafers are also utilised as the host substrate. However, this tends to be a more expensive option as silica wafers are not mass produced. Another difficulty associated with silica host substrates is the problem of cracking due to differing thermal expansion coefficients between doped- and un-doped silica layers. This could result in low yields and would therefore add to the costs of developing such technology.

Next, we should ask ourselves what constitutes an ideal planar substrate that is suitable for supporting optical waveguides. The propagation loss must be suitably low if practical waveguide circuitries are to be realised. Good uniformity in terms of waveguide geometry (layer flatness) and refractive index profile is also required to minimise performance variation. Propagation loss is caused by both absorption and scattering.

Absorption is a feature resulting from impurities in the silica matrix introduced during fabrication (extrinsic losses) and/or the inherent characteristics of the silica material itself (intrinsic losses). The term impurities in this case could imply either dopants added during the fabrication run to modify certain feature of the silica, or contaminants. An example of intrinsic losses is the infra-red absorption band of silica at $\lambda > 1580$nm (loss in excess of 1dB/km). However, this effect plays little role within the operating wavelengths of interest. Absorption due to OH ions dissolved in glass falls under extrinsic losses and these absorption peaks are at 720, 880, 950, 1130, 1240 and 1380nm [5], with peaks at 1240 and 1380 being the largest and most detrimental. For example, the loss due to 1ppm of OH impurity at 1380nm is ~ 4dB/km. Another form of loss is due to Rayleigh scattering which causes radiative losses, where guided light radiates into the cladding and is eventually lost. Rayleigh scattering results from inhomogeneities within the silica which are dimensionally smaller than the wavelength of light. Loss due to this type of scattering is proportional to λ^{-4} and decreases rapidly with increase in wavelength. In pure fused silica for example, scattering losses at 1300 and 1550nm were calculated to be 0.31dB/km and 0.15dB/km respectively [5]. In terms of layer uniformity, a planar substrate should display thickness variation and surface roughness of better than 0.1μm and 0.1nm respectively [6].

3-layer silica-on-silicon samples were utilised throughout this work. A schematic representation and image of the substrate are shown in Fig. 3.1. The typical refractive index value for the core layer is 1.45 with relative index difference, Δ of 0.3%. Relative index difference in this case is defined as [2]:

$$\Delta = \left(\frac{n_{core}^2 - n_{clad}^2}{2n_{core}^2} \right) \qquad [3.1]$$

where n_{core} and n_{clad} are the core and cladding refractive index respectively. For weakly guiding waveguides where $n_{core} \approx n_{clad}$, then Δ is $<< 1$ and the above expression can be accurately approximated by:

$$\Delta \approx \left(\frac{n_{core} - n_{clad}}{n_{core}} \right) \qquad [3.2]$$

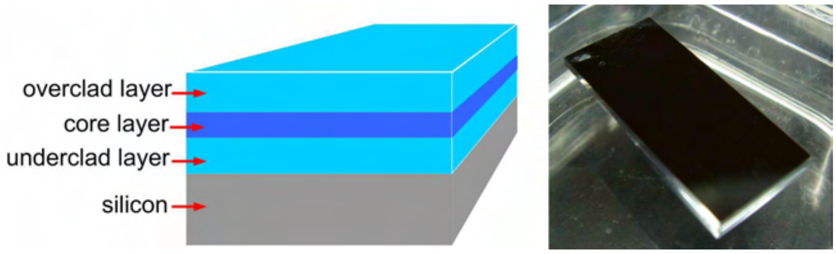

Figure 3.1 Schematic and photo of a three layer silica-on-silicon sample.

3.1 Planar Deposition Techniques

Various aspects of planar sample thin film deposition are described here. Knowledge gained in these methods will also be useful in gauging the significance of the flat fibre work presented in Chapter 9. Donald L. Smith's book on thin film deposition techniques [7] provides an excellent reference and is often quoted here. In general, all thin-film processes involve the sequential steps shown in Fig. 3.2.

A source of material is first provided. Then the material is transported to the target (a wafer or preform tube) where deposition takes place. Sometimes the film is subsequently annealed or consolidated, and finally it is analysed to evaluate the success of the process [7]. Thin film processes that employ solid source materials that are vaporised through heat or energetic beam of electrons, photons (laser ablation) or positive ions (sputtering) are categorised as physical vapour deposition (PVD). Those employing chemical means to convert solids to vapours, or supplies of source materials in the form of gas or evaporated liquids fall under the chemical vapour deposition (CVD) category.

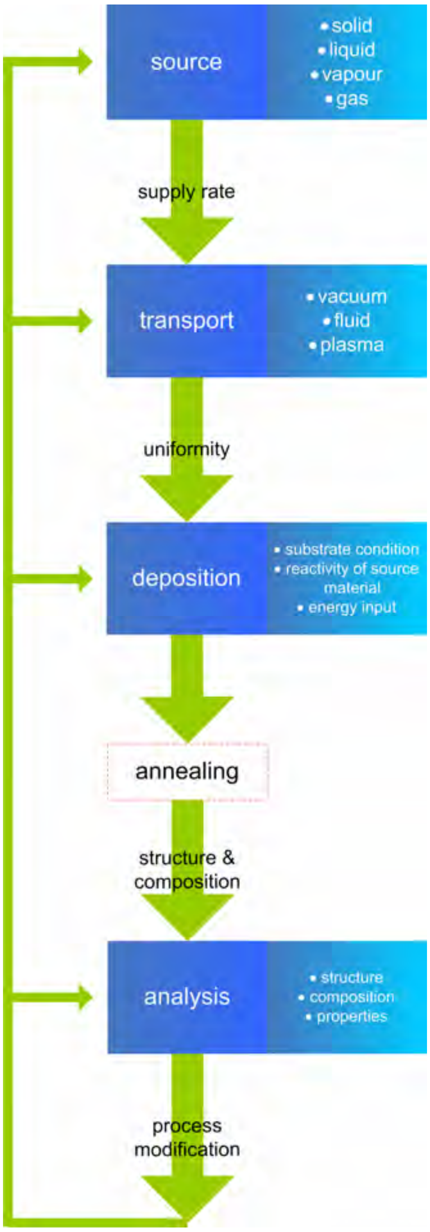

Figure 3.2 Thin film deposition process steps. In all steps, process monitoring is essential.

To date, the majority of planar waveguide device fabrication and manufacturing approaches are borrowed from those developed for the well established integrated microelectronics circuits industry. Low loss and reproducible waveguides are made by using techniques traditionally used for very large scale integrated circuits, usually based on multi-layer combinations of deposited silicon or silica. The most common deposition techniques are plasma enhanced chemical vapour deposition (PECVD) and flame hydrolysis deposition (FHD). PECVD and FHD are widely used in fabricating silica-on-silicon samples. In PECVD, a radio frequency (RF) discharge creates a low pressure plasma in an appropriate gas mixture that is used to initiate chemical reactions that produce silica layers. FHD involves the production of soot through the injection of halide[1] reagents into a hydrogen/oxygen flame. Silica can be produced via either direct oxidation or hydrolysis, depending on the flame temperature. Other techniques that are employed in producing silica substrates, which are not categorised as deposition techniques, include thermal oxidation and sol-gel.

3.1.1 Thermal Oxidation

Thermal oxidation is probably the simplest technique for creating silica films by means of oxidising the surface of a silicon wafer [8]. The oxidation process is achieved by placing silicon wafers into a high temperature and high pressure oxygen or water vapour environment. Typical operating temperatures vary and are within the regions of 700 - 1000ºC. The deposition rate is a function of the substrate temperature, ambient pressure and reagent flow rate, with [8] reporting a rate of < 1µm/minute for phosphosilicate (SiO_2-P_2O_5) glass layers with a silicon substrate temperature below 1000ºC. The formed silica layer is also often referred to as thermal oxide or buffer layer. The disadvantages of this technique include difficulty in adding dopants into subsequent layers (core and overclad) [9] mainly due to the thermal gradient needed and the consumption of the available native silicon species on the surface of the host substrate, and also the advent of unwanted diffusion of dopant molecules between layers of different compositions of the sample [3]. As such, this technique is mainly used in fabricating the buffer layer for use as an underclad, serving to isolate the waveguides in the core layer from the high refractive index silicon layer, thus protecting from mode leakage into the high index silicon layer (silicon typically has a refractive index in excess of 3). For example, our samples that were purchased from the Centre of Integrated Photonics (CIP) have a thermal oxide underclad layer of 15.9µm. In

---

[1] A halide consists of one part halogen atom and the other part an element or radical that is less electronegative than the halogen, to make a fluoride, chloride, bromide, or iodide compound. Many salts for example are halide.

addition to being utilised as the underclad layer, in some cases, the thermal oxide layer is used in conjunction with FHD (see below) i.e. the host substrate silicon has a thin thermal oxide layer so as to assist in FHD soot adhesion. This thin layer is typically about 5µm thick.

3.1.2 Sol Gel

This technique is based on the synthesis of glass via solution chemistry. In this case glass is formed not directly at high temperatures from a melt, but at low temperatures (< 1200ºC) from suitable compounds by chemical polymerisation in a liquid phase [8]. In this way a gel is first formed from which glass may be obtained both by gradual removal of liquid and densification through thermal treatment (annealing/sintering). The main steps of sol gel processing are summarised in Fig. 3.3 [8].

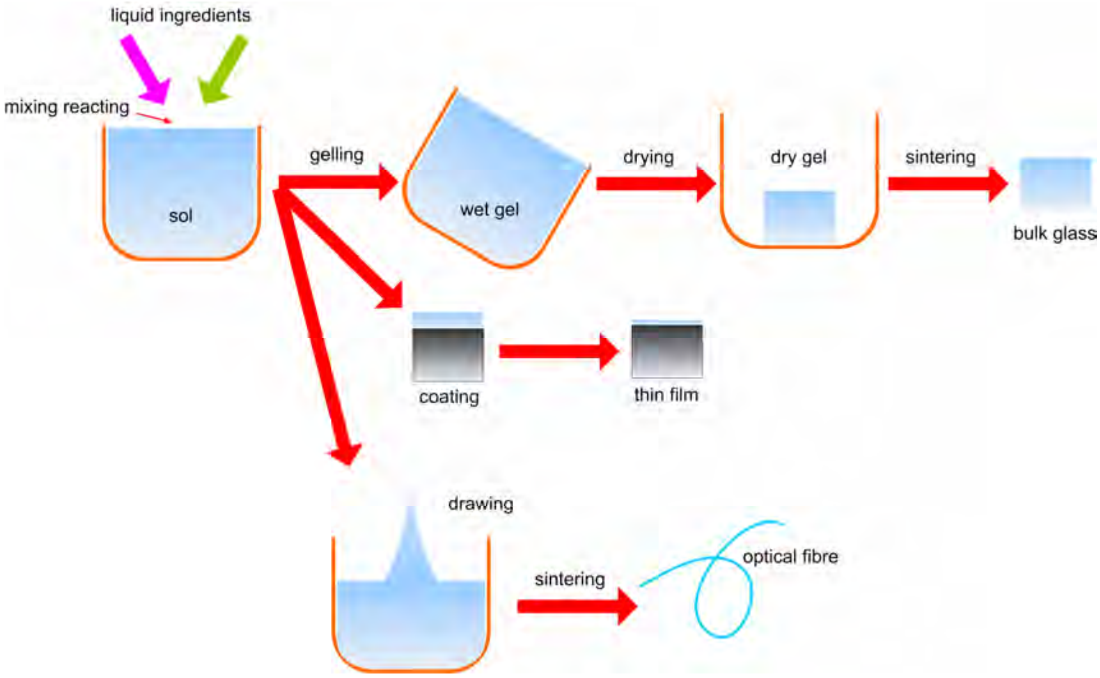

Figure 3.3 Summary of sol gel processing (taken from [8]).

The various forming operations have to occur before or during the gelling stage (e.g. forming a thin coating, or spinning a fibre). The drying/sintering stage simply consolidates the original shape produced at low temperatures. To produce thin films using this method, dip coating and spinning/spraying approaches can be utilised. In dip coating, a sheet of glass is immersed in a solution of suitable precursors and then slowly withdrawn, leaving a thin film clinging onto it. This is then reacted with water vapour to induce hydrolysis and polymerisation. The glass is then baked at ~ 500ºC. Layers up to 3000Å can be fabricated via this approach in each cycle.

The main difficulty of this technique is preventing cracking of the layers as they dry [1, 8], particularly when forming glass films. This is a result of non-uniform shrinkage of the drying body, leading to stress. The drying stage also takes longer compared to the consolidation stage in other methods (such as FHD), with [8] stating that this could reach ‘hundreds of hours even for small specimens with surface areas of a few square centimetres’.

3.1.3 Plasma Enhanced Chemical Vapour Deposition

Plasma Enhanced Chemical Vapour Deposition (PECVD) was initially developed for the microelectronics industry. It utilises energy provided by RF or microwaves to dissociate the reactants, creating high energy plasma that would then facilitate thin film deposition. The main advantage of this technique is that depositions can be carried out at low temperatures due to the additional energy provided by the plasma. A schematic diagram of the PECVD deposition chamber and process is shown in Fig. 3.4.

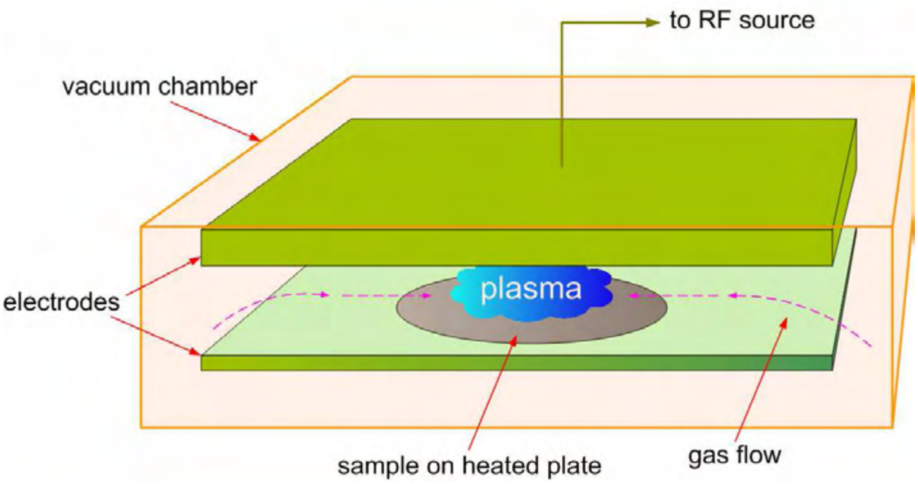

Figure 3.4 PECVD deposition chamber and process schematic.

The chemical reactions taking place during PECVD are as follow [9]:

a) when oxygen is used: $SiH_4 + O_2 \rightarrow SiO_2 + 2H_2$;

b) when nitrous oxide is used as the oxygen source:

    i. $SiH_4 + 2N_2O \rightarrow SiO_2 + 2H_2 + 2N_2$; or

ii. $SiH_4 + 4N_2O \rightarrow SiO_2 + 4N_2 + 2H_2O$.

In general terms, gas phase precursors are delivered into a deposition chamber where free electrons are accelerated by the applied field [9]. Collisions between the excited electrons and the precursor molecules results in the production of a plasma. The highly reactive reagents are incident onto the substrate where their energy is dissipated and adsorption takes place. A stable film is formed as a result from this. This is followed by an annealing stage to densify the film formed [10]. The annealing stage is also important in removing H-centre absorptions, also identified as harmonics of hydrogen bond resonances. Grand et al [11] measured these absorption peaks to have losses of 10.5dB/cm and 1.5dB/cm at 1506nm (Si-H and N-H bonds) and at 1400nm (O-H bond) respectively pre-annealed. These peaks were successfully removed by annealing at 1000ºC for 3 hours. A similar approach was taken by Hoffmann et al [12] (annealing > 1100ºC). Durandet et al [13] ensured that the N-H absorption was eliminated by using O_2 instead of N_2O. In PECVD, the parameters affecting film growth include reactant pressure and flow, the RF power, substrate temperature and biasing [14]. Layer doping with phosphorous, germanium and boron is performed to modify the optical and mechanical properties of the layers. These dopants are introduced into the main precursor in the form of phosphine (PH_3), germane (GeH_4) and borane (BH_3). PECVD deposition rate is typically 2000-5000 Å per minute [1].

3.1.4 Flame Hydrolysis Deposition

In flame hydrolysis deposition (FHD), vapour precursors are introduced in a flame where they undergo chemical reactions to form soot particles which are then collected on a planar substrate to form a low density porous layer [15]. The vapour precursor in this case is silicon tetrachloride ($SiCl_4$). The porous layer is then consolidated to form a dense glassy layer. This is achieved by heating the samples at temperatures exceeding 1200ºC. The exact consolidation temperature is dependent on a number of factors, particularly the dopants used, and the temperature dynamics (i.e. whether a slow ramp rate is employed or otherwise). A schematic view of FHD is shown in Fig. 3.5. A more detailed model of the system developed in the ORC, and the upgrade carried out during this PhD in isolating the control box of the FHD rig from the corrosive by-product of the deposition process is presented in Appendix A. I have also described some deposition work performed in the University of Malaya in October 2004 (Appendix B), as part of my effort to familiarise myself with the processes involved in FHD and to ensure a sufficient number of samples for UV writing experiments while the FHD system in the ORC was being upgraded

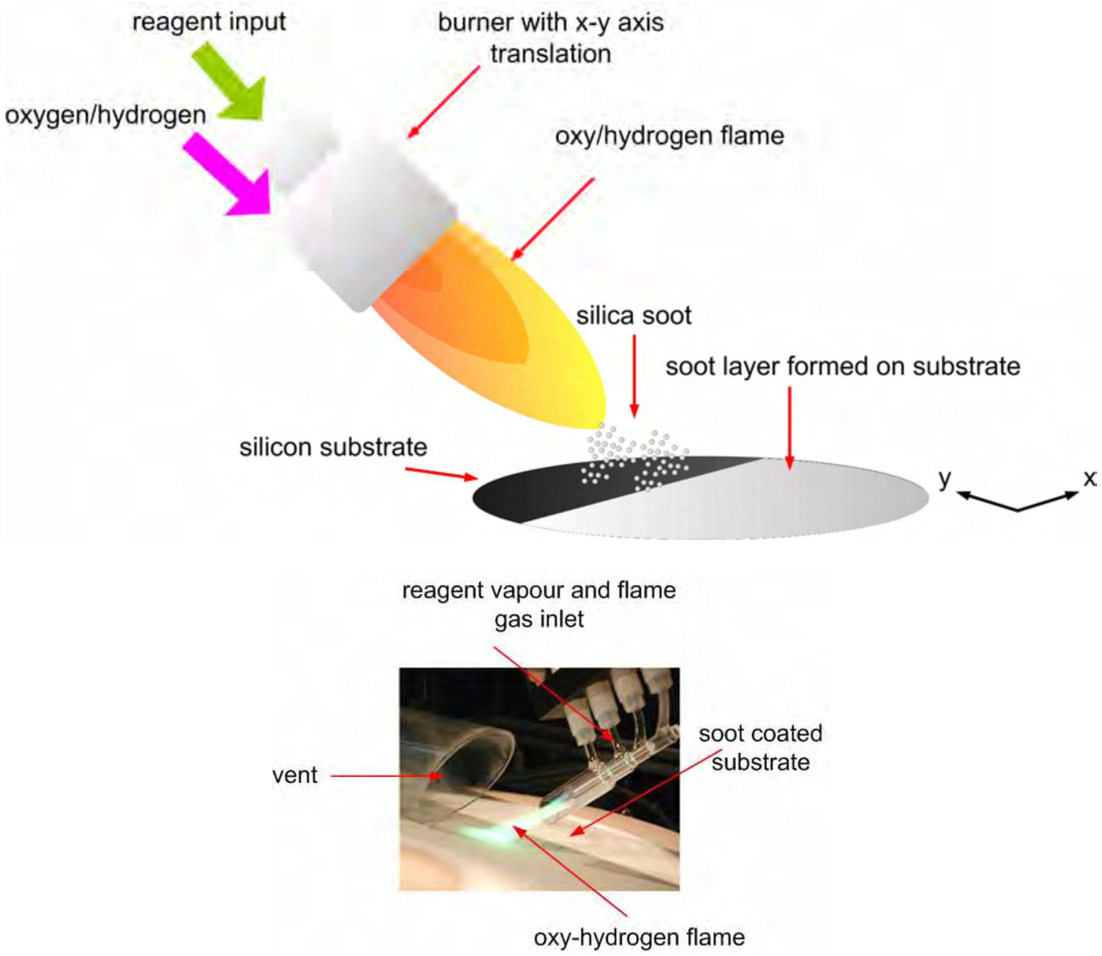

Figure 3.5 Schematic and photo of the deposition step of FHD. The soot is then consolidated to form a glassy layer.

The formation of silica soot from the reaction in an oxy-hydrogen flame is the basis for well established fibre fabrication techniques. Two such techniques are the modified chemical vapour deposition (MCVD) [16] and outside vapour deposition (OVD) [17]. Both MCVD and OVD involve the formation of silica soot by passing the relevant reagents onto a reaction zone created by a translating oxy-hydrogen burner. Glass layers are subsequently formed inside a cylindrical preform tube (MCVD) or surrounding a mandrel (OVD).

Flame hydrolysis as a method to produce pure silica soot was first reported in 1942 by J.F. Hyde [18]. In his invention, Hyde fabricated vitrified silica by passing vapours of a hydrolysable silicon compound such as $SiCl_4$, through a gas oxy-burner flame [17]. Further development of this technique was carried out by Keck and Schultz [19], and Schultz [20]. The first reported implementation of the technique onto a planar form was in 1983 when

Kawachi et al [21] fabricated low-loss SiO_2-TiO_2 planar waveguides with a propagation loss value of 0.1 dB/cm using flame hydrolysis deposition.

The chemical reactions taking place during FHD are as follow:

a) Flame temperature ≥ 1200ºC (direct oxidation): $SiCl_4 + O_2 \rightarrow SiO_2 + 2Cl_2$;

b) Flame temperature < 1200ºC (hydrolysis): $SiCl_4 + 2H_2O \rightarrow SiO_2 + 4HCl$.

More often than not, a flame temperature of > 2000ºC is utilised, ensuring direct oxidation will take place. Dopants are introduced to control the processing properties (viscosity, glass transition temperature) and more importantly the optical properties (refractive index, photosensitivity) of the FHD layers. The effect of the three commonly used dopants relative to pure silica is summarised in Table 3.1.

Table 3.1 Summary of effect of dopants relative to pure silica [22, 23].

Dopant	Product & chemical reaction	Effect
germanium	germanosilicate glass (SiO_2:GeO_2) $GeCl_4 + O_2 \rightarrow GeO_2 + 2Cl_2$	Thermal expansion: increase; Glass melting point: decrease; Refractive index: increase; Photosensitivity: increase.
phosphorous	phosphosilicate glass (SiO_2:P_2O_5) $2POCl_3 + 2H_2O \rightarrow P_2O_5 + 6HCl$	Thermal expansion: increase; Glass melting point: decrease; Refractive index: increase; Photosensitivity: decrease.
boron	borosilicate glass (SiO_2:B_2O_3) $4BCl_3 + 6H_2O \rightarrow 2B_2O_3 + 12HCl$	Thermal expansion: increase; Glass melting point: decrease; Refractive index: decrease; Photosensitivity: increase.

During deposition, the silicon host substrate is heated (>200ºC) to avoid the presence of liquid water as silica is hygroscopic [22], and to assist in soot adhesion.

3.2 Waveguide Definition Techniques

Waveguide definition refers to the creation of a refractive index structure within a substrate. This refractive index structure is tailored to allow light to be guided. The physics dictates that the waveguide must have a higher refractive index than its surroundings. Generally speaking, there are two main routes towards defining waveguide structures in PECVD or FHD silica-on-silicon substrates for integrated optical or planar lightwave circuits. The de-facto technique uses a combination of photolithography and etching (usually referred to simply as the etching technique). The alternative method, which is adopted in this work, is direct UV writing. As such, a more comprehensive description of the latter technique is given in Section 3.3. A further channel definition technique is ion exchange and this technique produces graded index waveguides.

3.2.1 Photolithography & Etching

The etching method process flow is shown in Fig. 3.6.

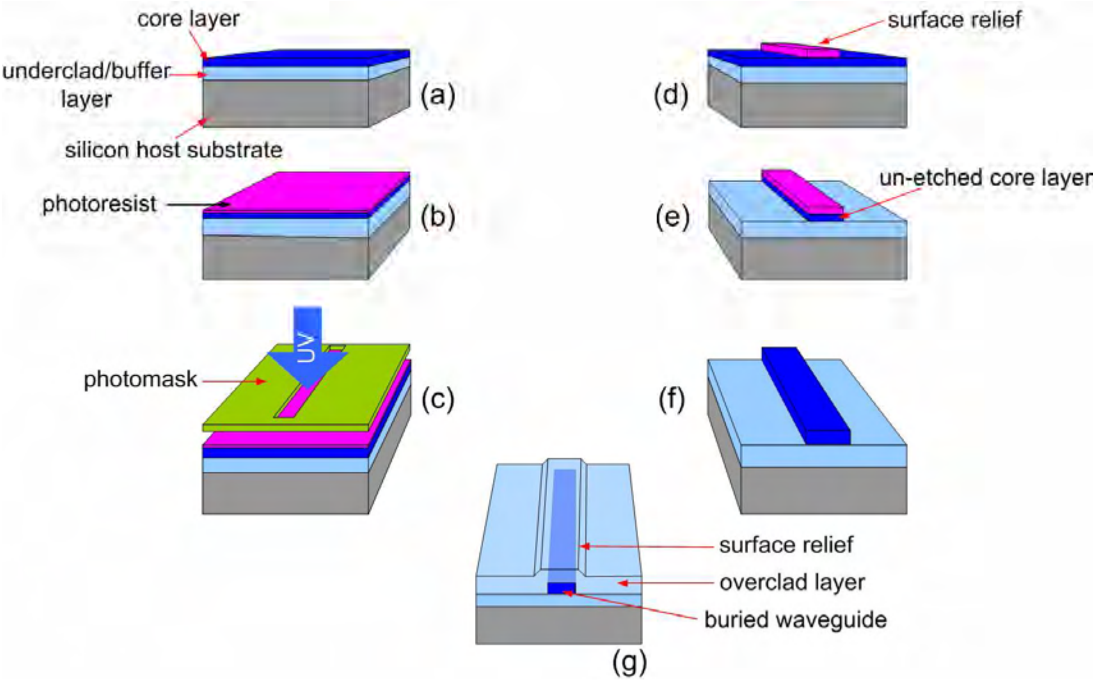

Figure 3.6 The etching method process flow.

A two layer substrate containing the core and underclad layers is first fabricated via PECVD or FHD (a). Then, the core layer is coated with photoresist by means of spin coating (b). UV light is subsequently illuminated onto a photo or transmission mask that contains the required waveguide design (c). The photo mask is designed in such a way so as to allow UV light to pass through it and subsequently irradiate regions in the photoresist layer where the resultant waveguides are required to be. Cross-linking of the polymer based resist takes place where it was UV exposed. This is followed by washing away the un-exposed resist, leaving a patterned core layer (d). The next process is to define the pattern onto the core layer by means of etching (e). A further processing stage removes the remaining photoresist layer (f). An overclad layer is then deposited to cover the patterned or surface relief features (g).

This technique is well suited for mass production. The ability to fabricate large numbers of identical devices leads to very low price per device, and relaxes the requirement for high yield production runs. Contrary to UV writing, this technique does not require the sample core layer to be photosensitive, which is an added advantage. On the other hand, for prototyping or fabrication of a handful of devices, this technique proves to be long and expensive. There are costs associated with the design and production of the masks, mask aligners, and clean room facilities. Furthermore, fabrication errors could be introduced in any of the numerous processing stages of the device/prototype. In addition to this, care must be taken to reduce sidewall roughness of the defined structures in order to minimise scattering-induced propagation loss. There are also problems with step coverage where voids could occur due to the inability to ‘cover’ minute features in the structures with the overclad layer, for example, in close vicinities to where two waveguides intersect [13].

3.2.2 Ion Exchange

The first ion exchanged waveguides were reported by Izawa and Nakagome in 1972 [24], where they described the formation of a high refractive index region beneath a glass layer by electrically induced migration of ions. In their case the glass substrate used was borosilicate and the salt solution was thallium nitrate. They found that thallium would diffuse into the glass matrix, replacing some of the alkaline Na^+ and K^+ ions. Subsequent work in this field saw the introduction of thermal diffusion as opposed to the electrical alternative, as well as a two-step field-assisted diffusion process [25].

The refractive index of the waveguide is dependent on the type and concentration of the different alkali ions used. Waveguides with Δn ranging from 10^{-3} up to as large as 10^{-1} with propagation losses of less than 0.1dB/cm have been reported [26]. Clearly, the use of such diffusion techniques result in graded index planar waveguides and requires precise control of the deposition parameters to successfully produce the required index profile.

3.2.3 Femtosecond Direct Writing

Femtosecond laser writing is a recently-developed direct writing technique that relies on ablation of the target substrate, causing the creation of waveguide structures. Use of this technique on glass substrates was first reported by Davis et al in 1996 [27] where buried channels with an index increase as large as 0.035 were observed. Following from this, a number of useful structures were fabricated via the method, including y-splitters [28] and X-couplers [29]. The technique is attractive in its ability to define waveguides in a variety of materials and the formation of 3D structures. This is still a relatively new field and there are still a number of issues to be addressed, not least in reducing the propagation loss of the resulting glass waveguide.

3.3 Direct UV Writing

Direct UV writing (DUW) is a technique to define wave guiding channels on photosensitive materials. It relies on a photosensitive reaction of the material to UV light irradiation. UV light is absorbed by the material and a corresponding index increase is created in the IR region. Historically, the concept was first proposed by Chandross et al [30], and it was referred to as 'photolocking'. In their work, 4μm optical waveguides with an index increase as large as $1x10^{-2}$ were formed in doped polymer film[2] when irradiated with a laser with λ=364nm, having losses of 0.20±0.05dB/cm at λ=633nm. They described that the technique produces 'smooth interfaces and low optical losses' by avoiding edge roughness introduced by solvent development or sputtering. This was followed by their work on couplers and gratings in 1975 where they used a different dopant (naphthalenethiol) for better dimensional resolution, resulting in short-period grating couplers (Λ=0.28μm) with coupling strength of up to 15dB/cm [31]. In 1979, Stewart et al [32] reported their study on photo-chromic material, observing that the material absorbs UV light, causing it to 'colour' and display change in refractive index, highlighting the possibility of '2D and planar waveguide components to be optically written and erased'. Direct UV writing on a silica-on-silicon platform was first reported in 1994 when Svalgaard described his work on direct UV-written buried single mode channel waveguides in germanium-doped silica films with an index increase in the region of 10^{-3} [33]. This is followed by work on practical devices such as directional couplers and power splitters in 1997 [34, 35] having low excess losses of the

---

[2] The polymer used was derived from 1:1 copolymer of methyl methacrylate and glycidyl methacrylate. The dopant is ethyl 2-(1-naphthyl) acrylate which has strong absorption in the 300-380nm region.

order of 0.2dB. The first reported experimental work from Smith's group in the ORC was in 2002 when Gawith reported direct UV-written buried channel waveguide lasers in direct-bonded inter-substrate ion-exchanged neodymium-doped germano-borosilicate glass [36]. This was followed by Emmerson, in the same year, who described the simultaneous definition of channel and Bragg gratings via the more advanced Direct Grating Writing (DGW) technique (see below) [37].

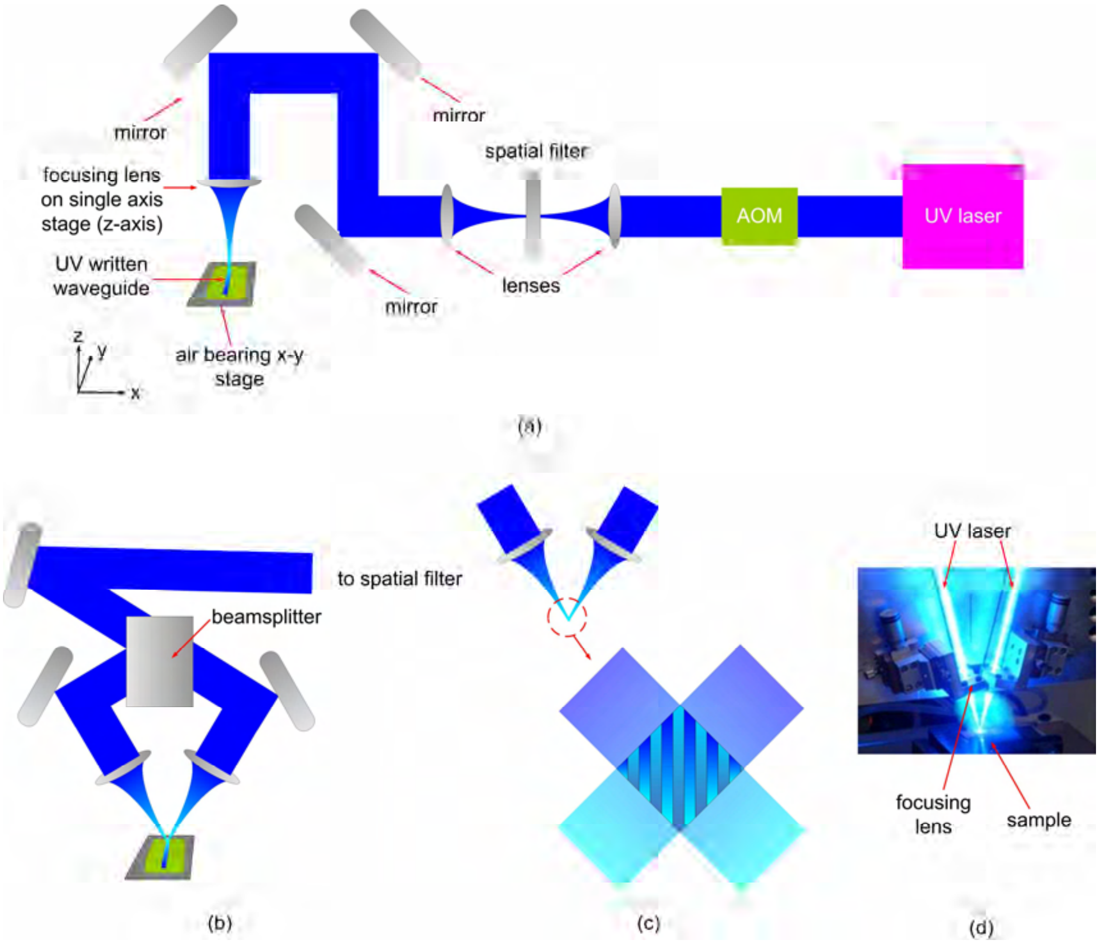

Figure 3.7 An illustration of (a) direct UV writing set up; (b) direct grating writing set up; (c) interference pattern generated by the crossed beam; (d) photo of direct grating writing. (AOM: acousto-optic modulator).

In our experiments, channel waveguides and devices were fabricated by use of a 244nm frequency doubled argon-ion laser (Coherent Sabre-Fred and later replaced by a Lexel laser). The laser beam is focussed down to circular spot measuring ~4μm (in diameter) and the sample underneath it is then translated relative to this writing spot, with the path translation defining the channel waveguide structure.

The DGW technique involves utilising the interference pattern generated by crossed UV beams and allows us to define simultaneously channel waveguides and grating structures. The UV interference pattern is generated by crossing two tightly focussed coherent UV beams at a fixed point in space. A photosensitive sample is then aligned with this interference spot and translated relative to it. If the writing laser is not modulated during the writing process (i.e. continuously on), the effect of the interference pattern is averaged out, producing channel waveguides similar to those produced using DUW. An interference pattern is produced on the sample if the writing spot laser is modulated with a frequency between subsequent exposures being the period of the interference pattern required. Such an approach enables simultaneous production of channel waveguides and gratings. The schematic diagrams and photo of the DUW and DGW set up is shown in Fig. 3.7.

Both DUW and DGW arrangements consist of a combination of high precision 3-D air bearing translation stages, a spatial mode filter stabilised UV beam source and a computer control system. The output of the UV laser is controlled/modulated using a Brewster angled fused-silica acousto-optic modulator. Spatial filtering[3] results in partial clipping of the beam spot, converting beam pointing fluctuations into intensity variations. Beam pointing stability is pertinent in interferometer set ups. Once filtered, the beam can be steered to either the single beam (DUW) or crossed beam (DGW) arrangement. The translation stages consist of cross mounted Aerotech air bearing stages with a translation span of 50cm x 50cm. The motion of the stages is operated through an extended computer numerical control process based on the Aerotech U600 control system, allowing structures to be defined using G-code programming language, where G-code is the universal computing language used in computer numerical controlled (CNC) machining applications.

The various parameters of the DUW/DGW set up that could be user-controlled and the corresponding characteristics of the devices written that would be affected by such parameters are underlined in Table 3.2.

---

[3] The spatial filter includes two UV coated mirrors to ‘decouple’ the laser from the system, a pinhole to ensure only the first order diffracted beam is used, collimating and focusing lenses, and two more pinholes to filter the Airy disc pattern surrounding the central beam to be used.

Table 3.2 DUW/DGW parameters and the corresponding device characteristics.

Parameter	DUW	DGW	Corresponding device parameter
Stage translation speed	✓	✓	Induced refractive index increase i.e. channel strength
UV laser power	✓	✓	Induced refractive index increase i.e. channel strength
Beam spot size	✓		Channel width
Beam duty cycle		✓	Gratings strength (see Chapter 7)
Interference pattern detuning		✓	Gratings period (see for example [38])

The magnitude of the refractive index change also depends on the composition of the glassy material forming the core and any processing prior to UV writing, for example hydrogen loading (see Chapter 4).

3.4 Summary

A review of fabrication techniques commonly utilised in producing silica-on-silicon substrates was presented. The techniques involve source reagents in vapour form being transported to the reaction site where chemical reactions take place with the assistance of either high energy plasma or oxy-hydrogen flame. In the PECVD case, a glassy layer is formed via energy dissipation and adsorption on the substrate. In the FHD, a porous soot layer is formed which is then consolidated to form a dense glassy layer.

The chapter then discusses the two main methods in defining light guiding channels onto the substrates – the conventional photolithography and etching method, and the newer technique of direct UV writing. Both techniques possess certain advantages and disadvantages. The former is well suited for mass production whereas the latter is ideal for prototyping and research.

The following chapter will discuss photosensitivity, which is a prerequisite for channel definition via direct UV writing.

References:

[1] D. Guilhot, "UV-written devices in rare-earth doped silica-on-silicon grown by FHD," PhD thesis, University of Southampton, 2004.

[2] F. Ladoucer and J. D. Love, *Silica-based buried channel waveguides and devices*, Chapman & Hall, United Kingdom, 1996.

[3] G. D. Emmerson, "Novel direct UV-written devices," PhD thesis, University of Southampton, 2003.

[4] M. Kawachi, "Recent progress in silica-based planar lightwave circuits on silicon," *IEE Proceedings-Optoelectronics*, vol. 143, pp. 257-262, 1996.

[5] A. Ghatak and K. Thyagarajan, *Introduction to Fiber Optics*, 2nd ed, Cambridge Press, USA, 2000.

[6] C. Riziotis, "Advanced Bragg grating based integrated optical devices for wavelength division multiplexing systems," PhD thesis, University of Southampton, 2002.

[7] D. L. Smith, *Thin film deposition: principles and practice*, McGraw-Hill Inc., New York, 1995.

[8] R. W. Cahn, P. Haasen, and E. J. Kramer, *Materials science and technology: Glasses and amorphous materials*, VCH, Germany, 1991.

[9] I. J. G. Sparrow, "Development and applications of UV-written waveguides," PhD thesis, University of Southampton, 2005.

[10] H. Ou, "Different index contrast silica-on-silicon waveguides by PECVD," *Electronics Letters*, vol. 39, pp. 212-213, 2003.

[11] G. Grand, J. P. Jadot, H. Denis, S. Valette, A. Fournier, and A. M. Grouillet, "Low-loss PECVD silica channel waveguides for optical communications," *Electronics Letters*, vol. 26, pp. 2135-2137, 1990.

[12] M. Hoffmann, P. Kopka, and E. Voges, "Low-loss fiber-matched low-temperature PECVD waveguides with small-core dimensions for optical communication systems," *IEEE Photonics Technology Letters*, vol. 9, pp. 1238-1240, 1997.

[13] A. Durandet, A. Perry, R. Boswell, F. Ladouceur, J. Love, M. Faith, F. Kemeny, X. Ma, and M. Austin, "Silica buried channel waveguides fabricated at low temperature using PECVD," *Electronics Letters*, vol. 32, pp. 326-327, 1996.

[14] R. F. Bunshah, "Critical issues in plasma-assisted vapor deposition processes," *IEEE Transactions on Plasma Science*, vol. 18, pp. 846-854, 1990.

[15] P. Tandon and H. Boek, "Experimental and theoretical studies of flame hydrolysis deposition process for making glasses for optical planar devices," *Journal of Non-Crystalline Solids*, vol. 317, pp. 275-289, 2003.

[16] S. R. Nagel, J. B. MacChesney, and K. L. Walker, "Overview of the modified chemical vapor deposition (MCVD) process and performance," *IEEE Journal of Quantum Electronics*, vol. QE-18, pp. 459-476, 1982.

[17] M. G. Blankenship and C. W. Deneka, "Outside vapor deposition method of fabricating optical waveguide fibers," vol. QE-18, pp. 1418-1423, 1982.

[18] J. F. Hyde, "Method of making a transparent article of silica," patent number 2272342, U. S. Patent Office, 1942.

[19] D. B. Keck and P. C. Schultz, "Method of producing optical waveguide fibers," patent number 3711262, U. S. Patent Office, 1973.

[20] P. C. Schultz, "Method of producing glass by flame hydrolysis," patent number 3859073, U.S. Patent Office, 1975.

[21] M. Kawachi, M. Yasu, and T. Edahiro, "Fabrication of SiO_2-TiO_2 glass planar optical waveguides by flame hydrolysis deposition," *Electronics Letters*, vol. 19, pp. 583-584, 1983.

[22] S. P. Watts, "Flame hydrolysis deposition of photosensitive silicate layers suitable for the definition of waveguiding structures through direct ultraviolet writing," PhD thesis, University of Southampton, 2001.

[23] A. Othonos and K. Kalli, *Fiber Bragg Gratings - Fundamentals and applications in telecommunications and sensing*, Artech House, USA, 1999.

[24] T. Izawa and H. Nakagome, "Optical waveguide formed by electrically induced migration of ions in glass plates," *Applied Physics Letters*, vol. 21, pp. 584-586, 1972.

[25] R. V. Ramaswamy and S. I. Najafi, "Planar, buried, ion-exchanged glass-waveguides: diffusion characteristics," *IEEE Journal of Quantum Electronics*, vol. QE-22, pp. 883-891, 1986.

[26] C. B. E. Gawith, "Novel active waveguide devices in direct-bonded structures," PhD thesis, University of Southampton, 2001.

[27] K. M. Davis, K. Miura, N. Sugimoto, and K. Hirao, "Writing waveguides in glass with a femtosecond laser," *Optics Letters*, vol. 21, pp. 1729-1731, 1996.

[28] D. Homoelle, S. Wielandy, A. L. Gaeta, N. F. Borrelli, and C. Smith, "Infrared photosensitivity in silica glasses exposed to femtosecond laser pulses," *Optics Letters*, vol. 24, pp. 1311-1313, 1999.

[29] K. Minoshima, A. M. Kowalevicz, I. Hartl, E. P. Ippen, and J. G. Fujimoto, "Photonic device fabrication in glass by use of nonlinear materials processing with a femtosecond laser oscillator," *Optics Letters*, vol. 26, pp. 1516-1518, 2001.

[30] E. A. Chandross, C. A. Pryde, W. J. Tomlinson, and H. P. Weber, "Photolocking-A new technique for fabricating optical waveguide circuits," *Applied Physics Letters*, vol. 24, pp. 72-74, 1974.

[31] W. J. Tomlinson, H. P. Weber, C. A. Pryde, and E. A. Chandross, "Optical directional couplers and grating couplers using a new high-resolution photolocking material," *Applied Physics Letters*, vol. 26, pp. 303-306, 1975.

[32] C. Stewart, W. J. Stewart, and B. Rogers, "Optical waveguide components in planar photochromic structures," *Proceedings of the Optical Communication Conference*, Amsterdam, Netherlands, 1979, paper 15.5/1-4.

[33] M. Svalgaard, C. V. Poulsen, A. Bjarklev, and O. Poulsen, "Direct UV writing of buried singlemode channel waveguides in Ge-doped silica films," *Electronics Letters*, vol. 30, pp. 1401-1403, 1994.

[34] M. Svalgaard and M. Kristensen, "Directly UV-written silica-on-silicon planar waveguides with low loss," *Electronics Letters*, vol. 33, pp. 861-863, 1997.

[35] M. Svalgaard, "Direct writing of planar waveguide power splitters and directional couplers using a focused ultraviolet laser beam," *Electronics Letters*, vol. 33, pp. 1694-1695, 1997.

[36] C. B. E. Gawith, A. Fu, T. Bhutta, H. Ping, D. P. Shepherd, E. R. Taylor, P. G. R. Smith, D. Milanese, and M. Ferraris, "Direct-UV-written buried channel waveguide lasers in direct-bonded intersubstrate ion-exchanged neodymium-doped germano-borosilicate glass," *Applied Physics Letters*, vol. 81, pp. 3522-3524, 2002.

[37] G. D. Emmerson, S. P. Watts, C. B. E. Gawith, V. Albanis, M. Ibsen, R. B. Williams, and P. G. R. Smith, "Fabrication of directly UV-written channel waveguides with simultaneously defined integral Bragg gratings," *Electronics Letters*, vol. 38, pp. 1531-1532, 2002.

[38] G. D. Emmerson, C. B. E. Gawith, S. P. Watts, R. B. Williams, P. G. R. Smith, S. G. McMeekin, J. R. Bonar, and R. I. Laming, "All-UV-written integrated planar Bragg gratings and channel waveguides through single-step direct grating writing," *IEE Proceedings: Optoelectronics*, vol. 151, pp. 119-122, 2004.

Chapter 4

Photosensitivity

Photosensitivity is defined as the permanent change in the index of refraction of a material when exposed to light with characteristic wavelength and intensity [1]. As mentioned in Chapter 3, this physical effect forms the basis of all the work involving direct UV writing in this thesis. The physical mechanisms underlying photosensitivity are not well understood and could be a combination of photochemical, photomechanical and thermo-chemical means. However, according to Othonos and Kalli [1], the current consensus on the mechanism of photosensitivity in silica glass is ‘the formation of colour centres that gives way to compaction of UV irradiated glass’, creating refractive index increase. Kristensen suggested in [2] that the colour or defect centre model is termed as the microscopic model whereas glass compaction is considered as macroscopic and stresses that ‘there is absolutely no consensus on how large a fraction of the refractive index change can be related to absorption changes and how much is simply compaction’.

Historically, photosensitivity in optical fibres was first discovered, albeit accidentally, by Hill [3] who, with his group of researchers, were investigating non-linear effects by pumping 488nm light into germanium-doped core fibres with 0.1-0.2 numerical aperture and 2.5µm core diameter. This eventually led to the discovery of self organised gratings via observation of the standing wave formed with the ~4% Fresnel reflection[1] at the fibre output facets. It was found that the input light was reflected back by the narrowband reflector with ~20% reflectivity. However, it was not until Meltz and co-workers [4] introduced the side inscription method in 1989, and used it to define in-fibre gratings, that interest in photosensitivity and its applications was heightened. In their work, the gratings

---

[1] Fresnel reflection occurs at the air-glass interfaces at the input and output facets of an optical fibre or channel waveguide (i.e. reflection at the interface between two media having different refractive indices).

The intensity reflection coefficient is given by: $[(n_1-n_2)^2/(n_1+n_2)^2]$ where n_1 and n_2 are the respective refractive indices of the two media.

were inscribed by illuminating the core from the side of the fibre with coherent 244nm UV radiation. Using this method, which they named the transverse holographic method, the grating period is determined by the incident wavelength and the included angle between the beams, making definition of gratings more flexible compared to the standing wave approach which was length limited by saturation effects. Another important step in progressing the field was by increasing photosensitivity levels and, in 1993, an index increase as high as $5.9\text{x}10^{-3}$ in GeO_2 fibres was reported by Lemaire et al [5]. This was made possible by sensitising the fibre prior to UV exposure by hydrogen loading (see Section 4.3).

4.1 Photosensitivity Mechanism

As mentioned earlier, the precise mechanism leading to the refractive index increase of material irradiated with UV sources is yet to be understood fully. This comes as no surprise, as the models proposed are dependent on the material itself, in our case germanium-doped silica, as well as the radiation band and laser intensity. As such, variations in fabrication methods, composition and post-processing directly impact the molecular structure of the doped silica matrix and ultimately define the material behaviour [6]. However, the two main models for the case of germanium-doped silica generally adopted in explaining photosensitivity are the defect centre (or colour centre) model and the glass compaction (or stress change) model. No general consensus has been reached as to which of the two is more accurate due to the varying levels of agreement, both qualitative and quantitatively, between the models and data obtained from experiments [2]. It is most likely that the index increase observed resulted from the combination of both effects.

The colour centre model argues that the colour or defect centres within the material are responsible for changes in the UV absorption spectrum of the glass, creating index change in the IR region via the causality principle. This increase can be quantified by obtaining the effective index change through Bragg grating reflectivity studies.

In order to understand the ‘defects’ notation, we first look at the structure of pure amorphous silica. The silica matrix consists of a silicon atom that is connected to four oxygen atoms forming a tetrahedral structure as shown in Fig. 4.1.

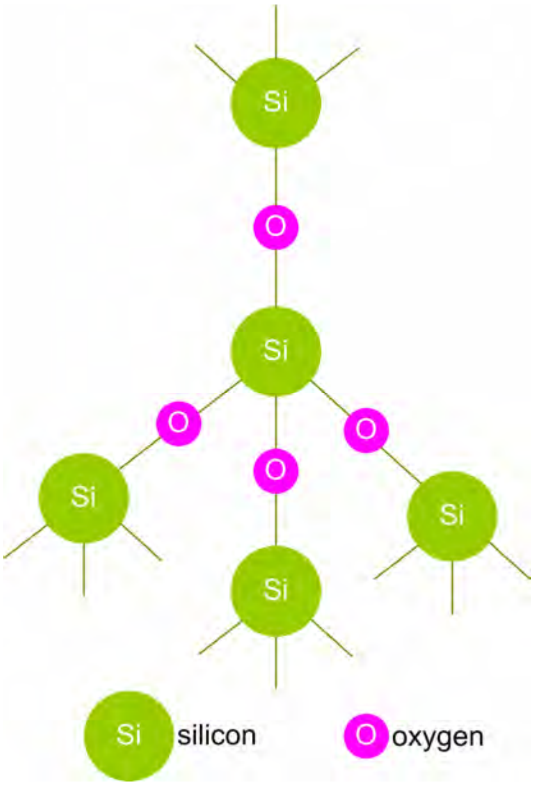

Figure 4.1 An illustration showing the tetrahedral structure of silica.

These tetrahedral structures form a quasi-periodic lattice, the irregularities within which are generally termed as 'defects'. Defects in a pure silica matrix can be in the form of silicon-to-silicon bonds (known as wrong bonds) and they are usually created during the fabrication of the glass itself [1]. Kashyap, in his book [7], stated that the inefficiencies of standard fibre fabrication methods such as OVD and MCVD result in the creation of sub-oxides and that the glass matrix is inhomogeneous on a microscopic scale. The three possible wrong bond defects for the case of germanosilicate glasses are Si-Si, Si-Ge and Ge-Ge. In principal, defects are not typically desired as they introduce absorption bands, leading to transmission losses.

However, these defects are instrumental from the photosensitivity point of view as they would form colour centres, absorbing UV light, and leading to an increase in the refractive index of the glass. When incorporated into glass, germanium manifests itself in the form of neutral oxygen vacancy (NOV) Ge-Si and Ge-Ge wrong bonds, and Ge2+ defects (also known as GeO), all of which are collectively known as germanium oxygen-deficient centres (GODCs) [1], as shown in Fig 4.2. These GODCs are linked to the 240nm (UV) absorption band. Specifically, according to Malo [8], the NOV wrong bond defects are associated with 240-242nm (~5eV) absorption peaks. Svalgaard mentioned in [9] that NOV absorption peaks at 245nm whereas Ge2+ has an absorption peak at 241nm, and the strong

240nm band absorption is the result of the overlap between the two peaks. The Ge(1) and Ge(2) defects, which are trapped electron centres, display absorption peaks around 280nm (4.4eV) and 213nm (5.8eV) respectively. In addition to this, the presence of phosphorous within the glass matrix, which is necessary in glass processing (as described in Chapter 3), also forms defects with absorption peaks around 193nm and 240nm. The 193nm absorption peak makes it possible to define index structures via excimer lasers. UV irradiation of the GODCs causes the formation of GeE', and the liberated electron from a GeE' site is free to move within the glass matrix, eventually becoming recaptured at the original defect site, at another GeE' hole site or forming Ge(1) and Ge(2) defects. The GeE' defects can be classified further as being either Ge(0) or Ge(3) and in both cases, the defects contain a hole trapped next to Ge at an oxygen vacancy site.

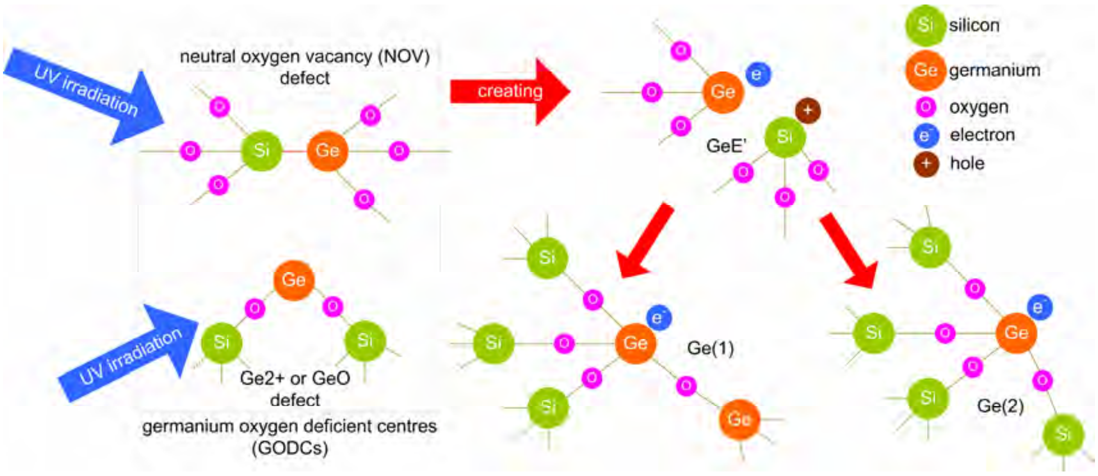

Figure 4.2 Colour centre model photosensitivity mechanism [7].

The glass compaction model is based on laser-irradiation induced density changes that result in refractive index changes [1]. This compaction is thermally reversible and is a function of both structural volume changes and the volume of oxygen ions present in the glass. UV excitation leads to bond breaking which, in turn, results in a volume change. By measuring surface modulations after gratings inscription using atomic force microscopy, Poumellec concluded that densification occurs in germanosilicate glass irradiated with UV and accounts for 7% of the observed index change for a pulsed laser source with λ=243nm (26% for continuous wave with λ=244nm) [10]. However, questions arise whether such surface modulation could possibly be a result of ablation rather than densification and in response to this, annealing experiments were performed by Douay [11] and topographical images were recorded when the samples were at the initial condition (T=23ºC) and after they were heated to 500 ºC. By measuring the depth of the valleys where gratings were inscribed (valleys imply glass compaction), and correlating the numbers obtained with observed index changes, the work proves that densification was, in fact, the mechanism leading to the surface modulation and not ablation. It is worth noting that in concluding his review, Douay mentioned the following: ‘Unlike enhancement of UV photosensitivity via hydrogen loading, no increase in densification following hydrogen can be observed in germanosilicate samples’. He added further that one can conclude that in the light of the above observations, that the colour centre model accounts for a large part of the photosensitivity in the hydrogen loaded germanosilicate samples.

Finally, it was observed that germanosilicate glasses exhibit broadband photoluminescence (PL) bands around 290nm, 400nm and 650nm upon UV irradiation [9]. The 400nm PL band decreases during UV exposure while the 650nm PL band increases. Work by Thibault and co-workers for example [12], concluded that the 400nm PL follows the index profile of the glass fibre (i.e. proportional to the Ge concentration of the fibre preform they experimented with). We have used this observation as a crude way of judging the photosensitivity of our samples, and subsequently determining the suitable UV fluence levels needed in order to successfully fabricate waveguide structures and prototypes.

4.2 Photosensitivity Dynamics

Observed refractive index changes in UV irradiated samples are broadly categorised into three types: Type I, Type IIA and Type II, on the basis of how a grating response evolves with increase in UV light dosage.

- Type I: Within this regime, the amplitude of the refractive index modulation (hence grating strength) and effective index increase monotonically with UV irradiation dosage. This is the regime that is used in most writing experiments. Increasing the dosage further would eventually result in the complete or partial erasure of the formed gratings and also, the formation of a new spectrum. This is the Type IIA regime.
- Type IIA: Following erasure of Type I gratings, another set of gratings with a slight wavelength shift towards the blue is formed (i.e. UV induced index decrease). Xie et al [13] suggested that the refractive index evolution results from two local reactions. The first reaction erases and produces some defects or chemical species which lead

to the positive change in the refractive index. The second, having a slower reaction time than the first, produces negative index change.

- Type II: The final phase, a Type II grating, is formed via ablation (physical damage) by using high intensity light which is usually pulsed rather than continuous wave.

4.3 Photosensitivity Enhancement

As applications involving UV inscribed gratings become more widely used, the need for a stronger and better defined spectral response grows accordingly. One of the means to fulfil such requirements is by increasing the photosensitivity of the host substrate. There are a number of ways to achieve this including increasing the level of germanium in the glass. Alternatively, the following approaches can be employed.

- Low temperature high pressure hydrogen loading

  This technique was first introduced in 1992 by Lemaire [5]. It is carried out by diffusing hydrogen molecules into germanosilicate samples at low temperatures and high pressures, creating more hydroxyl (OH) and GODCs, hence increasing photosensitivity [14]. This is also the approach employed in increasing the photosensitivity of the samples used for the experiments in this thesis.

  One disadvantage of this technique is that the hydroxyl species formed have an absorption band near 1400nm, which would affect transmission losses for λ~1500nm operation. An improvement to this would be using deuterium[2] loading, where the OD-group would have an absorption band at 1900nm, well away from the wavelength region of interest.

  The optimal length of time for hydrogen loading to take effect depends on the diffusion coefficient, or diffusivity, of hydrogen given by:

$$D = D_0 e^{\left(-\frac{E}{RT}\right)} \qquad [4.1]$$

  where D_0 is a constant independent of temperature and ambient pressure, E is the diffusion activation energy, R is the gas constant $8.3\text{JK}^{-1}\text{mol}^{-1}$ and T is the

---

[2] Deuterium is a hydrogen isotope and also known as heavy hydrogen. Its nucleus contains one neutron and one proton whereas the common hydrogen isotope does not have a neutron.

absolute temperature (K). The values of D_0 and E are found experimentally to be $5.65 \times 10^{-4} cm^2 s^{-1}$ and $43.55 kJmol^{-1}$ respectively. These values are similar for both pure and doped silica. It should be noted that this rate of diffusion is not dependent on pressure. On the other hand, the solubility of hydrogen is found to be proportional to applied pressure, and is higher at low temperatures [15]. Therefore, a combination of low temperature and high pressure loading is desirable. Our hydrogen loading apparatus allowed silica samples to be stored in a hydrogen atmosphere at approximately 120 bars at room temperature. The minimum loading duration for a typical silica-on-silicon sample was calculated by Sparrow to be ~3 days [6] with Riziotis estimating a maximum achievable hydrogen concentration of ~1.2 mole % at 100 bars [16].

- Flame brushing

  This method was first reported by Bilodeau [17]. The region of the optical waveguide to be photosensitised is brushed repeatedly by a flame fuelled by hydrogen (sometimes a small amount of oxygen is added). The flame temperature is set to be as high as 1700ºC and the maximum effect is achieved after about 20 minutes with increase in absorption (around λ=240nm) of ~700dB/mm. Flame brushing works in the similar principal as hydrogen loading, increasing photosensitivity and as such, also display an absorption band around 1400nm [18].

- Other dopants

  This includes boron (B) [19], tin (Sn) [20] and rare-earth ions such as europium (Eu) and cerium (Ce) [1].

4.3.1 Stability Issues

As mentioned earlier, we have chosen the hydrogen loading approach for increasing the photosensitivity of our samples. This, however, means that we are faced with the issue of hydrogen out-diffusion, which takes place the moment the samples are taken out of the hydrogen cell, and more importantly, during the UV writing process itself. Hydrogen out-diffusion would lead to the reduction of the UV induced refractive index change over a period of time determined by the factors dictated in equation [4.1], with thermal effects being the major contributor. This thermal stability issue is normally dealt with by subjecting the samples to an annealing stage, and this has been addressed by several groups, see for example, a review by Kashyap in his book [7]. The post-fabrication anneal stage typically involves heating the samples at around 80-100°C over a period spanning between a couple of hours to several days. However, this technique would also lead to 10-20% reduction of UV induced Δn [9] and based on this final point, I have decided not to implement post-fabrication annealing in my experiments. Given the 'prototyping' and proof of principle nature of the work presented in this thesis, the ability to generate as high a Δn as possible coupled with the short time span taken to characterise the samples (typically within weeks) outweighs the long term thermal stability issues.

The hydrogen out-diffusion problem upon removal of the samples from the hydrogen loading cell is inevitable. We reduce this effect by quickly putting the removed sample into a transport flask containing liquid nitrogen. To minimise out-diffusion *during* UV writing, Svalgaard implemented a cold chuck (or cooled sample chamber) which was set at temperatures below -30°C [9, 21]. A similar apparatus is currently being developed here in the ORC by Christopher Holmes, a member of our research group. Work by Emmerson has attempted to address this out-diffusion during UV writing issue by 'thermal locking', a rapid heat treatment process that involves subjecting the sample to elevated temperatures (> 1000°C) over a few seconds, believed to thermally induce bonding between deuterium and oxygen atoms at germanium sites, thus increasing defect species [22]. It was discovered later that thermally locked samples showed an order of magnitude less UV fluence dependency compared to 'unlocked' samples and that thermal erasure of written waveguides occur at ~400°C as opposed to the normal 650°C, suggesting reduced thermal stability [23]. Thermal locking is relatively unrefined as a technique for prolonging photosensitivity, with optimisation of 'locking' conditions being sample dependent.

Finally, hydrogen out-diffusion characterisation performed by Sparrow on a silica sample having 6μm thick overclad and 5.5μm core layer showed a 1×10^{-4} reduction in effective index over the 57 minutes required for the UV writing process [6]. He noted however, that the acquired data was surprisingly noisy and attributed this to variations in the shape of the grating spectra obtained. In light of this final observation, it could be argued that for a similar sample with a thicker overclad layer, the reduction in effective index would be lower. While this is not ideal, I believe that for the experiments presented in this thesis at least, the effect of hydrogen out-diffusion on the results obtained is minimal, and that the necessary steps taken to reduce this detrimental effect during the experiments are sufficient.

4.4 Summary

A brief overview of photosensitivity is presented as this is the essential pre-requisite for UV writing to be possible. There is currently no consensus about the origin of photosensitivity and the two main models are the colour centre and glass compression. Methods for enhancing photosensitivity as well as its dynamics were also discussed.

References:

[1] A. Othonos and K. Kalli, *Fiber Bragg Gratings - Fundamentals and applications in telecommunications and sensing,* Artech House, USA, 1999.

[2] M. Kristensen, Bragg gratings white paper, Ibsen Photonics, 2005. This document can be obtained from:
http://www.ibsenphotonics.com/products/phasemasks/tutorials/bragggratingswhitepaper

[3] K. O. Hill, Y. Fujii, D. C. Johnson, and B. S. Kawasaki, "Photosensitivity in optical fibre waveguides: Application to reflection filter fabrication," *Applied Physics Letters*, vol. 32, pp. 647-649, 1978.

[4] G. Meltz, W. W. Morey, and W. H. Glenn, "Formation of Bragg gratings in optical fibers by a transverse holographic method," *Optics Letters*, vol. 14, pp. 823-825, 1989.

[5] P. J. Lemaire, R. M. Atkins, V. Mizrahi, and W. A. Reed, "High pressure H_2 loadings as a technique for achieving ultrahigh UV photosensitivity and thermal sensitivity in GeO_2 doped optical fibres," *Electronics Letters*, vol. 29, pp. 1191-1193, 1993.

[6] I. J. G. Sparrow, "Development and applications of UV-written waveguides," PhD thesis, University of Southampton, 2005.

[7] R. Kashyap, *Fiber Bragg gratings,* Academic Press, USA, 1999.

[8] B. Malo, J. Albert, K. O. Hill, F. Bilodeau, and D. C. Johnson, "Effective index drift from molecular hydrogen diffusion in hydrogen-loaded optical fibres and its effect on Bragg grating fabrication," *Electronics Letters*, vol. 30, pp. 442-444, 1994.

[9] M. Svalgaard, "Ultraviolet light induced refractive index structures in germanosilica," PhD thesis, Technical University of Denmark, 1997.

[10] B. Poumellec, P. Guenot, I. Riant, P. Sansonetti, P. Niay, P. Bernage, and J. F. Bayon, "UV induced densification during Bragg grating inscription in Ge:SiO_2 preforms," *Optical Materials*, vol. 4, pp. 441-449, 1995.

[11] M. Douay, W. X. Xie, T. Taunay, P. Bernage, P. Niay, P. Cordier, B. Poumellec, L. Dong, J. F. Bayon, H. Poignant, and E. Delevaque, "Densification involved in the UV-based photosensitivity of silica glasses and optical fibers," *Journal of Lightwave Technology*, vol. 15, pp. 1329-1342, 1997.

[12] S. Thibault, J. Lauzon, and F. Ouellette, "Influence of Ge concentration on UV-excited luminescence in a graded-index fibre preform," *Electronics Letters*, vol. 30, pp. 517-518, 1994.

[13] W. X. Xie, P. Niay, P. Bernage, M. Douay, J. F. Bayon, T. Georges, M. Monerie, and B. Poumellec, "Experimental evidence of two types of photorefractive effects

occurring during photoinscriptions of Bragg gratings within germanosilicate fibres," *Optics Communications*, vol. 104, pp. 185-195, 1993.

[14] M. Fokine and W. Marguli, "Large increase in photosensitivity through massive hydroxyl formation," *Optics Letters*, vol. 25, pp. 302-304, 2000.

[15] J. F. Shackelford, P. L. Studt, and R. M. Fulrath, "Solubility of gases in glass II. He, Ne, and H_2 in fused silica," Journal of Applied Physics, vol. 43, pp. 1619-1626, 1972.

[16] C. Riziotis, "Advanced Bragg grating based integrated optical devices for wavelength division multiplexing systems," PhD thesis, University of Southampton, 2002.

[17] F. Bilodeau, B. Malo, J. Albert, D. C. Johnson, K. O. Hill, Y. Hibino, M. Abe, and M. Kawachi, "Photosensitization of optical fiber and silica-on-silicon/silica waveguides," *Optics Letters*, vol. 18, pp. 953-955, 1993.

[18] G. Brambilla, V. Pruneri, L. Reekie, and D. N. Payne, "Enhanced photosensitivity in germanosilicate fibers exposed to CO_2 laser radiation," *Optics Letters*, vol. 24, pp. 1023-1025, 1999.

[19] D. L. Williams, B. J. Ainslie, J. R. Armitage, R. Kashyap, and R. Campbell, "Enhanced UV photosensitivity in boron codoped germanosilicate fibres," *Electronics Letters*, vol. 29, pp. 45-47, 1993.

[20] L. Dong, J. L. Cruz, L. Reekie, M. G. Xu, and D. N. Payne, "Enhanced photosensitivity in tin-codoped germanosilicate optical fibers," *IEEE Photonics Technology Letters*, vol. 7, pp. 1048-1050, 1995.

[21] M. Svalgaard, "Effect of D_2 outdiffusion on direct UV writing of optical waveguides," *Electronics Letters*, vol. 35, pp. 1840-1842, 1999.

[22] G. D. Emmerson, C. B. E. Gawith, S. P. Watts, V. Albanis, R. B. Williams, S. G. McMeekin, J. R. Bonar, R. I. Laming, and P. G. R. Smith, "Photosensitivity locking technique applied to UV-written planar Bragg gratings," *Electronics Letters*, vol. 39, pp. 517-518, 2003.

[23] I. J. G. Sparrow, G. D. Emmerson, C. B. E. Gawith, S. P. Watts, R. B. Williams, and P. G. R. Smith, "Assessment of waveguide thermal response by interrogation of UV-written planar gratings," *IEEE Photonics Technology Letters*, vol. 17, pp. 438-440, 2005.

Chapter 5

Waveguide, X-coupler & Bragg Grating Theory

This section presents a brief treatment of waveguide analysis, beginning with the basic slab structure before progressing to the more accurate channel waveguide analysis tools provided by Marcatili and the Effective Index Method. These tools allow the determination of important waveguide parameters that influence light guidance behaviour. A waveguide is basically a light conduit that confines and directs the propagation of light. Generally speaking, for the purpose of this research, waveguides are designed to operate in the single mode regime for the wavelengths of interest. However, there are certain cases when multi mode operation is advantageous, as in the case of X-couplers (see Chapter 6). The ability to model the guidance behaviour of a waveguide prior to fabrication ensures efficient iteration towards successful implementation of functional devices. However, more often than not, in this work, these tools are used to analyse fabricated devices rather than as design tools. They form an integral part in understanding the physics behind observed behaviours, and from the analysis, important device parameters can be extracted. For the work on small angle X-couplers (Chapter 6), a commercial beam propagation method (BPM) design suite was also employed. Hence, a brief description of the BPM method is warranted. This chapter ends with a description of an analytical model developed specifically to describe direct UV written X-couplers and a brief theoretical treatment of reflection/short period Bragg gratings.

5.1 The Slab Waveguide

The relationship that governs total internal reflection, where light is reflected at the boundaries of two dielectric materials with dissimilar refractive indices, is derived from Snell’s law, as outlined below;

$$n_1 \sin\theta_1 = n_2 \sin\theta_2 \qquad [5.1]$$

The parameters n_1, n_2, θ_1 and θ_2 are depicted in Fig. 5.1(a).

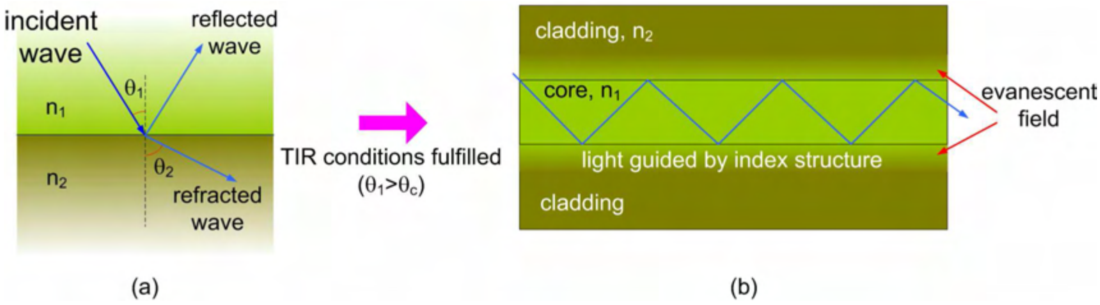

Figure 5.1 (a) Reflection and refraction at a plane interface, (b) light propagation in an index structure via total internal reflection (TIR) with evanescent field extending into the cladding layers.

n represents the refractive index values of the two media with $n_1 > n_2$, and θ is measured with respect to the normal of the boundary between the two media. The incident angle, θ_1 at which $\theta_2 = 90^{\circ}$ is called the critical angle, θ_c and light incident with angles exceeding this critical angle will be guided via total internal reflection. It can be seen from Fig. 5.1(b) that a small portion of the guided light is concentrated beyond the confines of the core layer and this is called the evanescent field. It will be discovered later in this section that this evanescent field has an exponentially decaying distribution within the cladding layer.

The picture above is the basic ray optics description of the behaviour of light within an optical waveguide. However, for a more insightful treatment of the behaviour, analyses based on solutions to Maxwell’s equations are sought. There is a vast amount of reference available regarding waveguide theory including work by Ghatak and Thyagarajan [1], Lee [2], Snyder and Love [3], and Okamoto [4]. For the majority of this section, the treatment is based on the presentation by Ghatak and Thyagarajan [1] as it is, arguably, easiest to follow. A slab waveguide comprising a core layer sandwiched between cladding layers is depicted in Fig. 5.2. The core layer has a refractive index value n_1 and for simplicity, it is assumed that the cladding layers have an identical refractive index of n_2. The core has a thickness, d and a higher refractive index than that of the claddings ($n_1 > n_2$), allowing light confinement. In this case, z is the propagation axis of the light incident onto the input face of the slab.

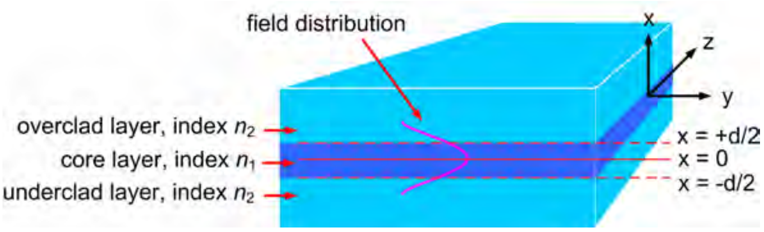

Figure 5.2 Slab waveguide indicating a transverse field distribution E_y. z is direction of propagation.

It can be shown by solving Maxwell's equations for isotropic, linear, non-conducting and non-magnetic media, we will obtain two sets of three coupled equations. The first set involves E_y, H_x and H_z (equations [5.2-5.4]) whereas the second involves E_x, E_z and H_y ([5.5-5.7]). E_n and H_n ($n = x, y, z$) in this case represent the electric and magnetic field components along the three main axes.

$$i\beta \mathrm{E}_y = -i\omega\mu_0 \mathrm{H}_x \qquad [5.2]$$

$$\frac{\partial \mathrm{E}_y}{\partial x} = -i\omega\mu_0 \mathrm{H}_z \qquad [5.3]$$

$$-i\beta \mathrm{H}_x - \frac{\partial \mathrm{H}_z}{\partial x} = i\omega\varepsilon_0 n^2(x)\mathrm{E}_y \qquad [5.4]$$

$$i\beta \mathrm{H}_y = i\omega\varepsilon_0 n^2(x)\mathrm{E}_x \qquad [5.5]$$

$$\frac{\partial \mathrm{H}_y}{\partial x} = i\omega\varepsilon_0 n^2(x)\mathrm{E}_z \qquad [5.6]$$

$$-i\beta \mathrm{E}_x - \frac{\partial \mathrm{E}_z}{\partial x} = -i\omega\mu_0 \mathrm{H}_y \qquad [5.7]$$

ε_0 is the electric permittivity in free space (8.8542x10^{-12} F/m), μ_0 is the magnetic permeability in free space (4πx10^{-7} H/m) and β is known as the propagation constant.

The first set of these equations ([5.2-5.4]) are known as the TE (transverse electric) modes, since the electric field has only a transverse component (E_y) with respect to the direction of propagation (z). The second set corresponds to the TM (transverse magnetic) modes, having non-vanishing values of H_y, E_x and E_z.

Considering the TE modes, by substituting equations [5.2] and [5.3] into [5.4], we obtain

$$\frac{d^2 \mathrm{E}_y}{dx^2} + \left[k_0^2 n^2(x) - \beta^2\right]\mathrm{E}_y = 0 \qquad [5.8]$$

where k_0 is the free space wave number given by equation [5.9] below, and c is the speed of light in free space (= $3\text{x}10^8\,\text{ms}^{-1}$). Equation [5.8] is also known as the scalar wave equation.

$$k_0 = \omega(\varepsilon_0\mu_0)^{\frac{1}{2}} = \omega / c = \frac{2\pi}{\lambda} \qquad [5.9]$$

Referring back to Fig. 5.2 and using the specific index profile as given below

$$n(x) = \begin{cases} n_1; & |x| < \dfrac{d}{2} \\ n_2; & |x| > \dfrac{d}{2} \end{cases} \qquad [5.10]$$

and by applying suitable boundary conditions, we obtain for the core layer the following

$$\frac{d^2 \mathrm{E}_y}{dx^2} + \left(k_0^2 n_1^2 - \beta^2\right)\mathrm{E}_y = 0; \quad |x| < {}^{d}\!/_{2} \qquad [5.11]$$

For the cladding layer

$$\frac{d^2 \mathrm{E}_y}{dx^2} + \left(k_0^2 n_2^2 - \beta^2\right)\mathrm{E}_y = 0; \quad |x| > {}^{d}\!/_{2} \qquad [5.12]$$

Guided modes are those that are mainly confined to the core and hence their field should decay in the cladding. This means that

$$\beta^2 > k_0^2 n_2^2 \qquad [5.13]$$

Furthermore, in order to satisfy the boundary conditions,

$$\beta^2 < k_0^2 n_1^2 \qquad [5.14]$$

Thus, for guided modes, we must have

$$n_2^2 < \frac{\beta^2}{k_0^2} < n_1^2 \qquad [5.15]$$

Recognising that equations [5.11] and [5.12] are of the form shown by equations [5.16] and [5.17] below

$$\frac{d^2\mathrm{E}_y}{dx^2}+\kappa^2\mathrm{E}_y=0; \quad |x|<d/2 \qquad [5.16]$$

$$\frac{d^2\mathrm{E}_y}{dx^2}-\gamma^2\mathrm{E}_y=0; \quad |x|>d/2 \qquad [5.17]$$

where

$$\kappa^2=k_0^2n_1^2-\beta^2 \qquad [5.18]$$

$$\gamma^2=\beta^2-k_0^2n_2^2 \qquad [5.19]$$

suggests solutions of the form

$$\mathrm{E}_y(x)=A\cos\kappa x+B\sin\kappa x; \quad |x|<d/2 \qquad [5.20]$$

and

$$\mathrm{E}_y(x)=\begin{cases} Ce^{\gamma x}; & x<-d/2 \\ De^{-\gamma x}; & x>d/2 \end{cases} \qquad [5.21]$$

where *A*, *B*, *C* and *D* are constants.

Further detail is obtained by ensuring continuity at the boundary between the core and the cladding layers i.e. no abrupt change in the field profile at the boundaries. Both E_y and its derivative, $d\mathrm{E}_y/dx$ must be continuous at $x = \pm d/2$. Applying symmetry conditions simplifies the problem further as the field within the core is either symmetric or anti-symmetric about $x = 0$. The symmetric solution is described as follows

$$\mathrm{E}_y(x)=\begin{cases} A\cos\kappa x; & |x|<-d/2 \\ Ce^{-\gamma|x|}; & |x|>d/2 \end{cases} \qquad [5.22]$$

Applying the continuity requirement at the boundaries yields

$$A\cos\left(\frac{\kappa d}{2}\right) = Ce^{-\gamma d/2} \qquad [5.23]$$

and

$$-\kappa A\sin\left(\frac{\kappa d}{2}\right) = -\gamma Ce^{-\gamma d/2} \qquad [5.24]$$

Dividing equation [5.24] by equation [5.23]

$$\xi \tan\xi = \frac{\gamma d}{2} \qquad [5.25]$$

where

$$\xi = \frac{\kappa d}{2} = \left(k_0^2 n_1^2 - \beta^2\right)^{\frac{1}{2}} \frac{d}{2} \qquad [5.26]$$

Similarly, for the anti-symmetric modes, we have

$$\mathrm{E}_y(x) = \begin{cases} B\sin\kappa x; & |x| < -d/2 \\ \dfrac{x}{|x|} De^{-\gamma|x|}; & |x| > d/2 \end{cases} \qquad [5.27]$$

Next, we introduce a dimensionless parameter called the '*V*-number' that encompasses the waveguide parameters that will directly determine the guidance behaviour of the waveguide, given by

$$V = k_0 d\left(n_1^2 - n_2^2\right)^{\frac{1}{2}} \qquad [5.28]$$

Applying the continuity requirement onto equation [5.27] and utilising equation [5.28], we obtain two transcendental equations for symmetric and anti-symmetric modes respectively

$$\xi\tan\xi = \left(\frac{1}{4}V^2 - \xi^2\right)^{\frac{1}{2}} \qquad \textit{symmetric} \qquad [5.29]$$

$$-\xi\cot\xi = \left(\frac{1}{4}V^2 - \xi^2\right)^{\frac{1}{2}} \qquad \textit{antisymmetric} \qquad [5.30]$$

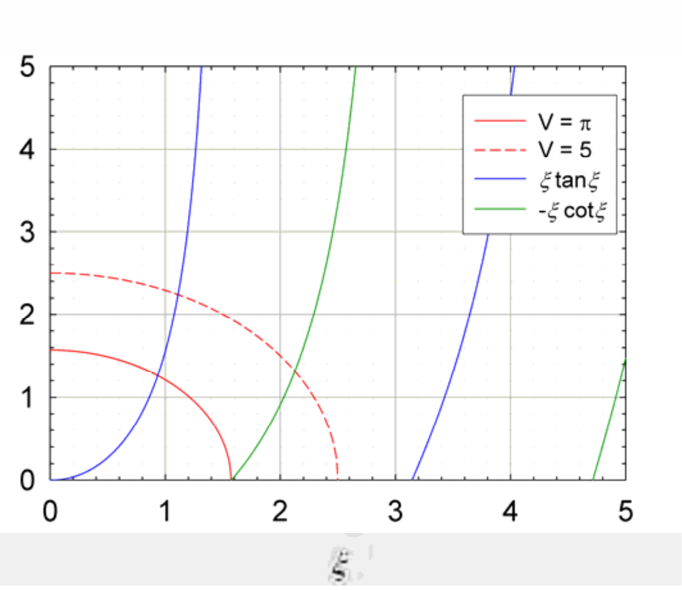

Figure 5.3 Graphical solutions to equations [5.29] and [5.30]. The blue curves represent symmetric modes whereas green curves represent anti-symmetric modes. The intersection between these two curves with the red *V*-number locus indicates the mode(s) supported by the slab. The y-axis shows the value of either the LHS or RHS of equations [5.29] and [5.30] respectively.

As mentioned earlier, the main object of the exercise above is to illustrate the guidance behaviour of the waveguide and to provide both quantitative and qualitative pictures of the way the field is distributed within the core and cladding layers. As depicted in Fig. 5.3, the number of intersection(s) between the curves described by equations [5.29] and [5.30] provides the number of mode(s) that can be supported by the structure. In this case, V must be smaller than 0.5π in order for the slab waveguide to operate in single-mode at λ=1550nm.

Following the discussion of the theoretical treatment for a basic slab structure, we now consider methods that can cater for guidance in channel-type waveguides. There are a number of techniques available, with varying levels of complexity and flexibility, including Marcatili's [5] and Effective Index [6, 7]. Throughout this work, I have utilised the Effective Index method. I have included Marcatili's work in this section as it has a number of similarities with the Effective Index method and acts as a comparative case.

Of course, without an accurate knowledge of the index profile of the fabricated structures, certain assumptions are necessary and, as such, the accuracy of the models is somewhat limited. Intuitively, we would expect UV written channels to possess a graded index profile. Svalgaard's work on characterisation of UV written waveguides via luminescence microscopy, for example [8], points to a trapezoidal index structure, with the bottom channel dimensions being similar to the UV beam spot size. However, in analysing single mode structures, regardless of the index profile structure, the fundamental mode is well approximated by a Gaussian function $\psi(r)=A\exp(-r^2/\omega^2)$ where A is a constant and ω is the spot size of the modal field [1]. Sparrow [9] pointed out that taking a step index approximation as opposed to graded index accounts for a maximum effective index variation in the order of $\sim10^{-4}$. In light of these observations, we have opted to choose a step index approximation in order to simplify the waveguide theoretical analysis.

5.1.1 Marcatili Method

Marcatili begins his analysis by considering an index structure which is depicted below.

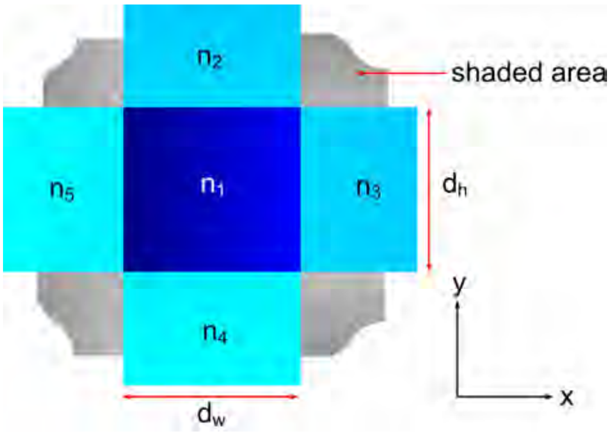

Figure 5.4 Marcatili's depiction of a channel waveguide index profile.

Intuitively, and from the picture provided from the previous section, we know that for a given index profile with $n_1 > n_v$ (where $v = 2, 3, 4, 5$), the field will be concentrated within the core n_1 with a sinusoidal variation, and decays exponentially in regions n_v. Since the field distribution is even lower in the shaded areas depicted in Fig. 5.4, these were neglected in Marcatili's approach without significantly compromising the accuracy of the results.

By ignoring the shaded areas, the index profile depicted can be treated as two independent 3 layer slab waveguides – one along the x-axis (n_5, n_1, n_3) and the other along the y-axis (n_2, n_1, n_4). This would decouple the field solution into two transverse components. In his analysis, Marcatili chose the nomenclature *k* to represent the propagation constant, β, and thus, such convention will be limited to this particular section only.

Once the distinction between the two slabs was made, the propagation constant for each medium, k_w (where w = 1, 2 ... 5) could be calculated via

$$k_w = kn_w = \frac{2\pi}{\lambda} n_w \tag{5.31}$$

The effective index, n_{eff} of the core can be calculated by first determining the propagation constant, k_z along the propagation axis *z* given by

$$k_z = \left(k_1^2 - k_x^2 - k_y^2\right)^{1/2} \tag{5.32}$$

where k_x and k_y are the transverse propagation constants in the x and y directions respectively. The problem is further simplified by identifying that $k_x = k_{x1} = k_{x2} = k_{x4}$ and $k_y = k_{y1} = k_{y3} = k_{y5}$. The effective index, n_{eff} is then given by

$$n_{eff} = \frac{k_z \lambda}{2\pi} \tag{5.33}$$

The transverse propagation constants k_x and k_y are solutions of these equations

$$k_x = \frac{p\pi}{d_w}\left(1 + \frac{A_3 + A_5}{\pi d_w}\right)^{-1} \tag{5.34}$$

$$k_y = \frac{q\pi}{d_h}\left(1 + \frac{n_2^2 A_2 + n_4^2 A_4}{\pi n_1^2 d_h}\right)^{-1} \tag{5.35}$$

where *p* and *q* represent the number of extremes of the sinusoidal field components within the core n_1. *A* is governed by

$$A_v = \frac{\pi}{\left(k_1^2 - k_v^2\right)^{1/2}} = \frac{\lambda}{2\left(n_1^2 - n_v^2\right)^{1/2}} \tag{5.36}$$

Following the initial assumptions made regarding field decay in the cladding layers, this method becomes less accurate as mode confinement decreases (decreasing *V*) where the modal field spreads farther into the cladding, and inevitably, into the ignored shaded areas shown in Fig. 5.4.

5.1.2 Effective Index Method

Similar to the approach taken by Marcatili, this method involves first solving the propagation constant in one dimension, thus again reducing the problem to a slab waveguide consideration. However, contrary to Marcatili's, the shaded areas were not ignored, leading to a more accurate depiction of the modal field behaviour. The effective index of a symmetric slab waveguide (as depicted in Fig. 5.2 in Section 5.1) is obtained by solving [10, 11]

$$\tan\left(kh\sqrt{n_1^2 - n_{eff}^2} \right) = \sqrt{\frac{n_{eff}^2 - n_2^2}{n_1^2 - n_{eff}^2}} \qquad [5.37]$$

where h is the half-thickness of the slab. Fig. 5.5(a) depicts the graphical solution for given n_1 and n_2 values. To allow for index asymmetry of the slab waveguides, the asymmetry parameter, a is introduced, given by [2]

$$a^{TE} = \left(\frac{n_2^2 - n_3^2}{n_1^2 - n_2^2} \right) \qquad [5.38]$$

where $n_1 > n_2 > n_3$. The asymmetric coefficient for the TM mode is given by:

$$a^{TM} = \left(\frac{n_2^2 - n_3^2}{n_1^2 - n_2^2} \right) \left(\frac{n_1^2}{n_3^2} \right) \qquad [5.39]$$

The effect of asymmetry on the waveguide dispersion behaviour (relationship between parameters b and V) is illustrated in Fig. 5.5(b). Putting this asymmetry parameter into the transcendental equation below, and solving b would lead to the determination of the effective index via equation [5.41] as elaborated in [2]

$$V\sqrt{1-b} = p\pi + \tan^{-1}\left(\sqrt{\frac{b}{(1-b)}} \right) + \tan^{-1}\left(\sqrt{\frac{b+a}{1-b}} \right) \qquad [5.40]$$

$$b = \left(\frac{n_{eff}^2 - n_2^2}{n_1^2 - n_2^2} \right) \qquad [5.41]$$

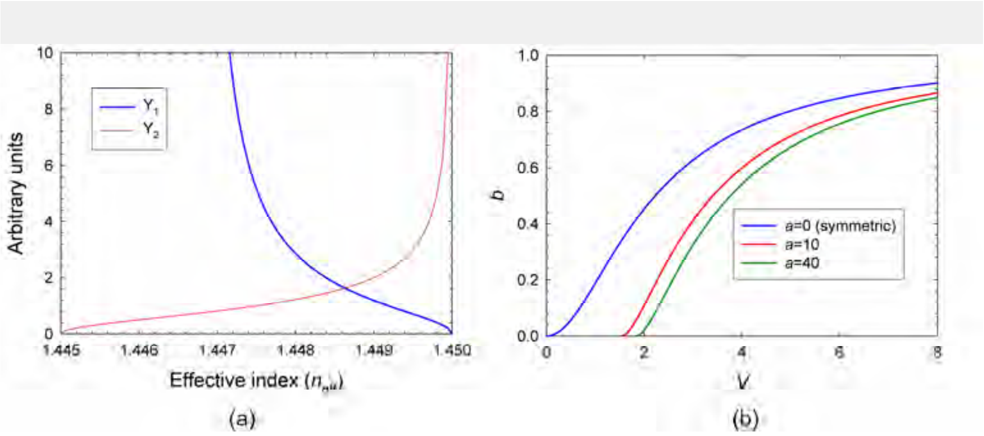

(a) (b)

Figure 5.5 (a) Graphical solution of transcendental equation [5.37] (n_1=1.45, n_2=1.445, d=4µm, λ=1550nm). n_{eff} = 1.4486 is obtained for the given simulation parameters. Y1 = $\tan\left(kh\sqrt{n_1^2 - n_{eff}^2}\right)$ and Y2 = $\sqrt{\left(n_{eff}^2 - n_2^2\right) \div \left(n_1^2 - n_{eff}^2\right)}$; (b) effect of asymmetry on the dispersion relationship for the fundamental TE mode (i.e. p = 0 for equation [5.40]).

The approach taken to evaluate a channel structure using the Effective Index method is depicted in Fig. 5.6. The channel waveguide index profile is first separated into 3 independent slab waveguides along the y-direction. These slabs have index profiles (n_1-n_4-n_7), (n_2-n_5-n_8), and (n_3-n_6-n_9) respectively. Solving the effective index of each of the slabs and denoting them n_{eff1}, n_{eff2} and n_{eff3}, the technique is then re-applied to solve the resulting slab in the x-direction (n_{eff1}, n_{eff2}, n_{eff3}) with width 2w.

5.1.3 Beam Propagation Method

Beam propagation method (BPM) is essentially a particular approach for approximating the exact wave equation for monochromatic waves, and solving the resulting equations numerically [12, 13]. As the name implies, the technique calculates the field as it propagates along a given waveguide by means of solving the wave equation using the finite difference method (FDM) [13, 14]. As mentioned earlier, we utilised a commercial BPM design suite (developed by RSoft – version 5.1) as a tool to understand the behaviour exhibited by our UV written small angle X-couplers. The key parameters required to implement the technique are 1) the refractive index distribution of the waveguide and 2) the input wave field. A given waveguide problem is formulated under the restrictions of a scalar field and paraxiality. Here, a scalar field means that polarisation effects are neglected and paraxiality implies that the propagation is restricted to a narrow range of tilt angles.

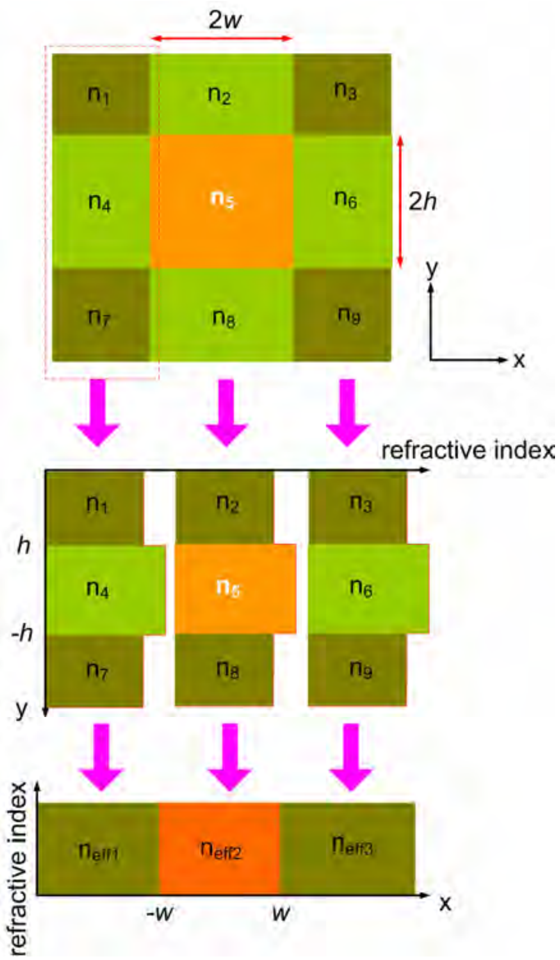

Figure 5.6 Obtaining the effective index of the core by successively implementing the Effective Index method onto the various slab waveguides.

It could be shown that the wave equation can be written in a form that can be solved by FDM. Using this approach, the transverse field distribution is represented only at discrete points on a grid, and at discrete points along the propagation axis (*z*). As such, the resolution of the calculation directly depends on the magnitude of the unit size set for all three axes.

In simulating our devices, particularly small angle X-couplers, we have implemented what we call a 'convergence' approach. This involved optimising the parameters chosen at each stage of the simulation. By 'optimising' we mean cross checking the simulated behaviours with available measured data. For a given structure, we first simulate a basic 3-layer single channel and compare the mode profile with measured ones. This requires the 3D feature of the BPM suite. One disadvantage of using the 3D feature is the inability of the software to provide a topographic index distribution of the buried channel structure. As such, the existence of important features, such as raised index sections of the X-coupler waist (see Chapter 6) and index tapering could not be confirmed. This however is not the case when the 2D feature is utilised. With this in mind, once there was a good agreement between the two modal profiles, we obtained the effective index value of the channel waveguide, and this value will subsequently be used in the 2D simulation that follows. Again, this effective index value is cross-checked with values obtained numerically using the method discussed in Section 5.1.2. Additional features that are unique to the waveguide structure being simulated are systematically added to the simulation profile and, where possible, cross references to available experimental data are performed.

Specific BPM features, catering for waveguide tilt, were utilised in simulating X-couplers. As previously described, the basic BPM formulation is limited by the paraxiality condition. This paraxiality limitation arises from the use of a slowly varying envelope to represent the wave propagation in order to simplify the analysis, thus stripping the model from the term representing the rapidly varying phase oscillation. Overcoming this issue involves solving the wave equation ‘exactly’ by first assuming the function to be a quadratic expansion problem, by ignoring the relevant differential terms [12, 15]. This expansion is then solved via Padé approximants and the Padé order determines the number of terms added to the expansion to increase the resulting accuracy. In fact, the BPM toolbox that was used contains wide angle features including the Padé order, and use of a wave-number, k that is related to cosine of the waveguide tilt angle.

5.2 Analytical Model for Direct UV Written X-couplers

The analytical model used in modelling small angle UV written X-couplers was taken from work by Durr and Renner [11]. The various parameters used in the model, including the depiction of supermodes, are illustrated in Fig. 5.7. The dark blue diamond-shaped region shown is known as the waist of the X-coupler having refractive index n_w.

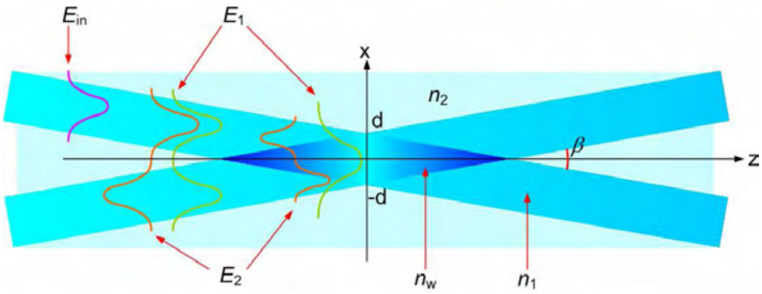

Figure 5.7 Schematic representation of the X-coupler and various supermodes. E_{in} is the input field whereas E_1 and E_2 are the even and odd supermodes respectively. β is the crossing angle and n_w is the waist index.

A supermode is the term used to denote the modes of a composite structure involving more than one waveguide (coupler structures being one of these) where waveguides are placed within close proximity to one another. The reason for this nomenclature is to distinguish these modes from the modes associated with each individual waveguide, which are termed 'local modes' [10].

In developing their model, Durr and Renner first calculated the field distribution of odd and even supermodes approaching the waist section of the X-coupler by solving the standard scalar wave equation such as the one summarised by equation [5.8]. The principle underlying this concept is analogous to superposition of harmonics in producing a sinusoidal wave. The input field, E_{in}, is 'broken' into even and odd supermodes sufficiently far from the X-coupler waist. These supermodes, when superimposed, reproduce E_{in}.

These supermodes are then propagated across the X-coupler. Allowance for the raised waist index increase due to multi-UV exposure is made by introducing a normalised parameter h (see below). Similar to a conventional coupler case, phase shifts between the various supermodes will take place. The total phase shift at the output end of the X-coupler would then determine the coupling behaviour of the structure. It is also worth pointing out at this point that in order to preserve adiabatic mode propagation across the X-coupler, the model assumes no radiation losses taking place, placing an upper limit value on the X-coupler crossing angle, β. In their work, Durr and Renner have limited their analysis to a maximum crossing angle of 1°.

It can be shown that the field distribution of the supermodes is given by equations [5.42] and [5.43] within the specified regions of the X-coupler. Note that the variables d_1 and d_2 denote the boundaries of the calculation as opposed to representing the actual waveguide width (i.e. $|d_2 - d_1| \neq$ waveguide width).

<table>
<tr><td colspan="2">
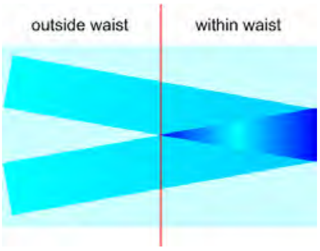

</td></tr>
<tr>
<td>

outside waist

$$E(x)=\begin{cases} a_1 hyp(Wx), & 0 \le x < \pm d_1 \\ a_2\cos(Ux)+a_3\sin(Ux), & \pm d_1 \le x < \pm d_2 \\ a_4\exp(-W\,|\,x\,|), & \pm d_2 \le x < \pm\infty \end{cases}$$

[5.42]

where the index distribution is as follows:

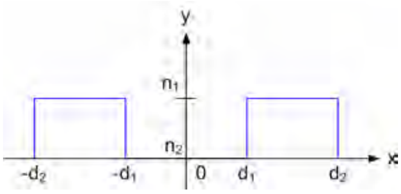

</td>
<td>

within waist

$$E(x)=\begin{cases} b_1 trg(Qx), & 0 \le x < \pm d_1 \\ b_2\cosh(Sx)+b_3\sinh(Sx), & \\ & \pm d_1 \le x < \pm d_2 \\ b_4\exp(-W\,|\,x\,|), & \pm d_2 \le x < \pm\infty \end{cases}$$

[5.43]

where the index distribution is as follows:

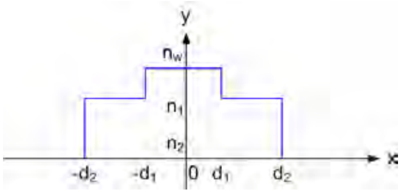

</td>
</tr>
</table>

In equation [5.42], $hyp(Wx) = \cosh(Wx)$ for even and $hyp(Wx) = \sinh(Wx)$ for odd supermodes respectively. Similarly, for equation [5.43], $trg(Qx) = \cos(Qx)$ for even supermodes and $trg(Qx) = \sin(Qx)$ for odd supermodes. $a_{1..4}$ and $b_{1..4}$ are constants and can be solved by applying the boundary conditions. The various normalised waveguide parameters are defined as follows:

$$W = V\sqrt{B} \qquad [5.44]$$

$$U = V\sqrt{1-B} \qquad [5.45]$$

$$Q = V\sqrt{h-B} \qquad [5.46]$$

$$S = V\sqrt{B-1} \qquad [5.47]$$

B and h are defined as:

$$B = \frac{\beta^2 - k^2 n_2^2}{k^2\left(n_1^2 - n_2^2\right)} \approx \frac{\beta - kn_2}{k\left(n_1 - n_2\right)} \qquad [5.48]$$

$$h = \frac{n_w^2 - n_2^2}{n_1^2 - n_2^2} \approx \frac{n_w - n_2}{n_1 - n_2} \qquad [5.49]$$

Examples of the supermode field distribution outside the waist (a), and within the waist with h = 2.6 and B = 2.24 (b), are depicted in Fig. 5.8.

The model further elaborates the conditions that would lead to near-lossless operation. They postulated that in order to achieve a near-lossless condition, the waist segment of the X-coupler must be able to support only the first two supermodes[1]. Such conditions would ensure that radiation loss is minimised as the modes evolve entering the single-mode output ports of the X-coupler. A single-mode waist segment would theoretically give rise to at least a 3-dB insertion loss as the second supermode becomes un-guided and is subsequently radiated into the cladding. A highly multi-mode waist would be susceptible to unwanted mode coupling resulting from waveguide imperfections and therefore, potentially adding to the device insertion loss.

In short, according to the analysis, adiabatic mode evolution will only take place if 1) the waist is multi-mode in a way so as to be able to support a specific number of modes, and 2) that the crossing angle, hence waveguide tilt, is shallow or small enough so as to minimise bend loss (which is due to radiated modes).

The work also provided an empirical formula for the calculation of the accumulated phase shifts between the supermodes, ϕ_{total}, which is valid for a specified range of h, given by

$$\phi_{total} = \frac{\sqrt{2}}{\beta}\sqrt{\Delta}V\left(c_0 + c_1 V + c_2 h + c_3 V h\right) \qquad with\ \left(1 \le h \le 4\right) \qquad [5.50]$$

where c_0 = 2.02, c_1 = -0.878, c_2 = 1.152 and c_3 = -0.248. According to the authors, use of this empirical formula, as opposed to the exact numerical alternative, results in a relative error of 0.75%, and this is deemed acceptable.

---

[1] Durr and Renner used a convention that supposes the first even supermode as the fundamental mode of the composite X-coupler structure. Additionally, in accordance with the convention used when analysing local modes, the second supermode would then be asymmetric (i.e. odd supermode).

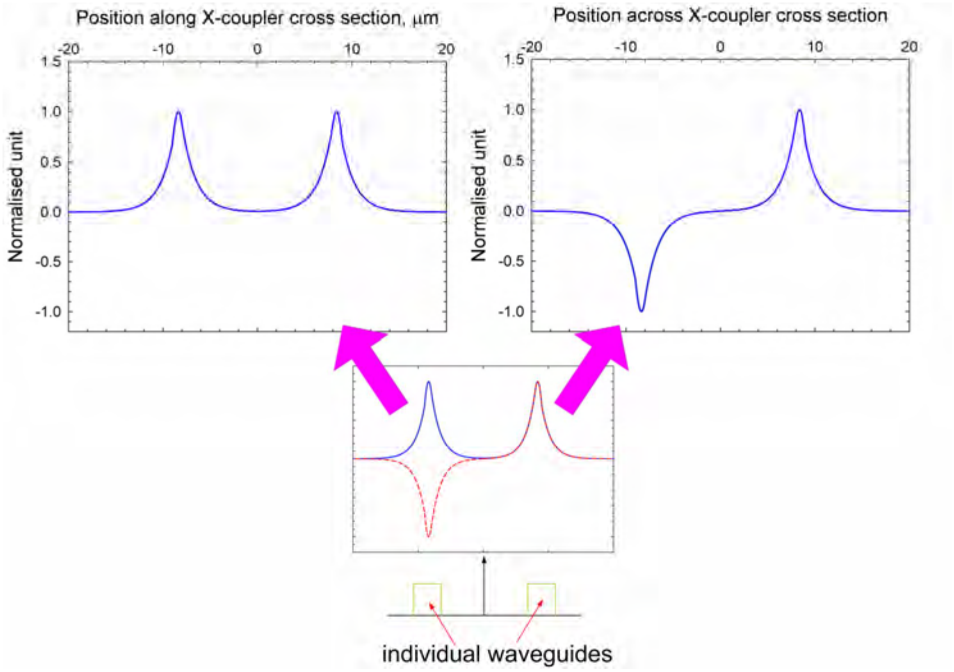

(a)

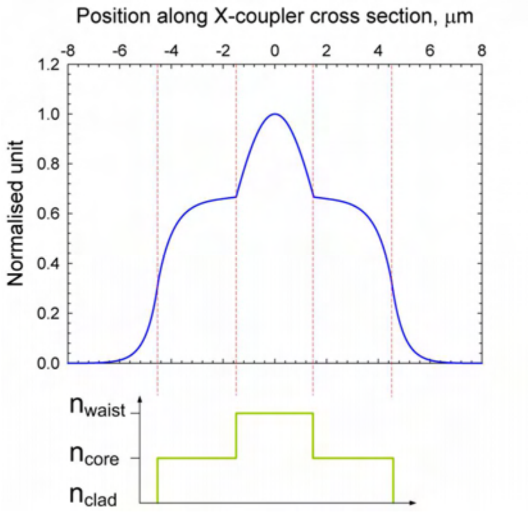

(b)

Figure 5.8 Examples of calculated supermode field distribution. In (a), the even and odd supermodes are depicted. Superimposing the two supermodes results in a field distribution in only one of the channels, reproducing the input field. In (b), the field distribution approaching the mid-point of the waist of the X-coupler is shown.

The variation of output power as a function of X-coupler crossing angle, and the dependence of output power to the normalised profile height, h are shown in Fig. 5.9, where the coupled (P_x) and through ($P_=$) powers were described by the following equations

$$P_{\times} = \sin^2\left(\frac{\phi_{total}}{2}\right) \qquad [5.51]$$

$$P_{=} = \cos^2\left(\frac{\phi_{total}}{2}\right) \qquad [5.52]$$

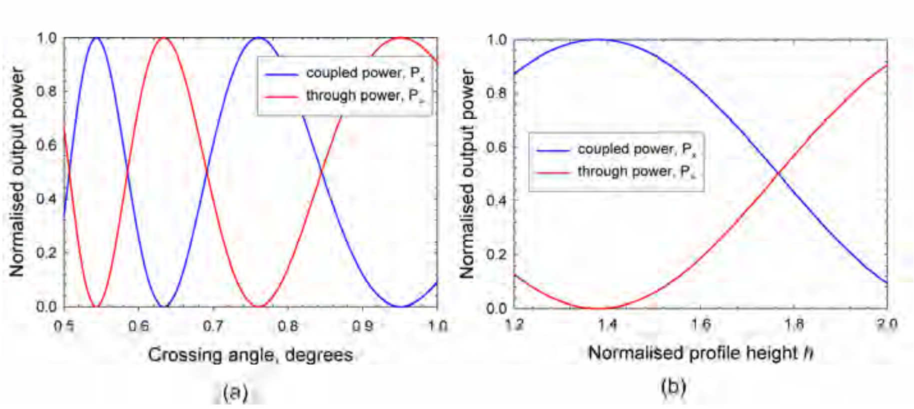

Figure 5.9 (a) Output powers as a function of crossing angle ($h = 2$, $V = 1.4532$, $\Delta = 0.19\%$); (b) output powers as a function of normalised profile height h ($\beta = 1°$).

5.3 Bragg Grating Theory

In Chapter 2, I have described the important role that Bragg gratings play in modern optical telecommunication networks and other critical fields such as sensing. In this section, the various parameters that govern the operation and performance of the structure will be examined in more detail. For a more in-depth treatment of the subject covering various theoretical approaches in analysing different grating index profiles, and methods to fabricate them in fibres and planar substrates, readers are directed to work by Kashyap [16], and Othonos and Kalli [17]. I have extracted work by Erdogan [18] for most parts of this section.

Bragg gratings are periodic index perturbations within a waveguide. When a guided mode that is incident onto these perturbations satisfies what is termed the 'Bragg condition', power coupling takes place. This power coupling can occur between the incident mode and either a mode travelling in the same direction as the incident mode (transmitted mode) or one that is travelling in the opposite direction (reflected mode).

The picture above arises from the laws of conservation of energy and momentum. Conservation of energy dictates that the energy of the incident and transmitted/reflected waves are conserved. Conservation of momentum requires that the wavevector of the incident wave (k_i), coupled with the wavevector of the perturbations forming the gratings (K) must equal the wavevector of the resultant co- or counter-propagating wave (k_r). This is summarised by the expression below

$$k_i \pm k_r = \mathrm{K} \tag{5.53}$$

where K = (2π)/Λ and Λ is the period of the index perturbations. Recognising that for an opposite travelling wave (with respect to the incident wave), the wavevector is $-k_r$, and to satisfy the Bragg condition for a reflection grating case, $|k_i| = |k_r|$, we obtain

$$\frac{2\pi}{\lambda} n_{eff} + \frac{2\pi}{\lambda} n_{eff} = \frac{2\pi}{\Lambda} \tag{5.54}$$

where we have employed $k = k_0 n_{eff}$. Solving the above equation, we will obtain

$$\lambda_B = 2 n_{eff} \Lambda \tag{5.55}$$

The equation above provides the basic design parameters for the Bragg grating of interest, relating the grating period to the desired reflected wavelength. However, in order to deduce useful characteristics such as the grating reflection strength and bandwidth as well as its spectral distribution, use of the coupled mode theory is necessary. References [1, 16, 19] contain a detailed treatment of the coupled mode analysis. We will simply apply the results obtained via this technique to the analysis of weak Bragg gratings, where the amplitude of the index perturbation is small compared to the waveguide strength and the incident wave penetrates to the end of the grating length.

The simplest of Bragg gratings have an index perturbation profile described by

$$\delta n_{eff}(z) = \overline{\delta n_{eff}}(z)\left[1 + \gamma \cos(\mathrm{K} z)\right] \tag{5.56}$$

where $\overline{\delta n_{eff}}$ is the 'dc' index change spatially averaged over a grating period and γ is the fringe visibility of the index change. For a grating profile with $\gamma = 1$, it could be proven that the power reflection spectrum of the grating is given by [18]

$$r = \frac{\sinh^2\left(\sqrt{\kappa^2 - \hat{\sigma}^2}\, L\right)}{\cosh^2\left(\sqrt{\kappa^2 - \hat{\sigma}^2}\, L\right) - \dfrac{\hat{\sigma}^2}{\kappa^2}} \tag{5.57}$$

L is the grating length whereas κ and $\hat{\sigma}$ are coupling coefficients following coupled mode analysis. These coefficients are described as follows

$$\kappa = \frac{\pi}{\lambda}\gamma\overline{\delta n}_{eff} \tag{5.58}$$

and

$$\hat{\sigma} = \delta + \sigma \tag{5.59}$$

where

$$\delta = 2\pi n_{eff}\left(\frac{1}{\lambda} - \frac{1}{\lambda_D}\right) \tag{5.60}$$

and

$$\sigma = \frac{2\pi}{\lambda}\overline{\delta n}_{eff} \tag{5.61}$$

$\lambda_D = 2n_{eff}\Lambda$ is the 'design wavelength' for Bragg scattering by an infinitesimally weak grating ($\delta n_{eff} \rightarrow 0$) with a period Λ. The maximum power reflectivity, $r_{\max}$ of the grating is provided by simplifying equation [5.57]

$$r_{\max} = \tanh^2(\kappa L) \tag{5.62}$$

and recognising that this occurs when $\hat{\sigma} = 0$, or at wavelength

$$\lambda_{\max} = \left(1 + \frac{\overline{\delta n}_{eff}}{n_{eff}}\right)\lambda_D \tag{5.63}$$

Examples of grating reflectivity at different κL values are shown in Fig. 5.10. In calculating these spectra, the grating length was held constant and $\kappa = f\left(\overline{\delta n}_{eff}\right)$ is a measure of the index 'strength' of the index perturbations forming the grating.

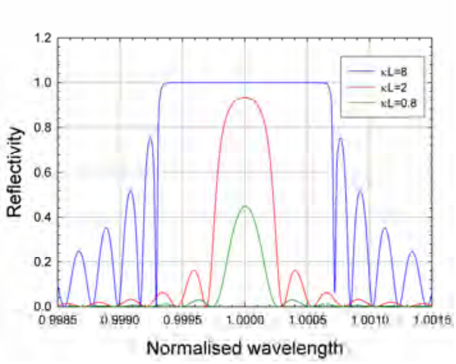

Figure 5.10 Reflection spectra versus normalised wavelength (λ/λmax) for uniform gratings with various κL values.

The side lobes either side of the main reflection peaks shown in Fig. 5.10 are non-ideal if the gratings are to be employed in applications requiring narrow bandwidth filtering with high sideband suppression such as DWDM channels with < 25GHz spacing. In order to overcome these issues, the grating parameters, more specifically the index perturbation profile along the length of the grating can be altered. Novel index profiles such as Gaussian apodised are commonplace and result in the reduction of the amplitude of the side lobes by at least 80%, as shown in [18].

5.4 Summary

In summary, I have discussed the approaches taken towards developing a picture for the modal field distribution within the basic slab waveguide and the more practical buried channel structure. Guidance conditions for the waveguides can be extracted from normalised parameters such as the ‘V-number’, providing an important starting point from which considerations towards fabrication of practical single mode devices are made. The use of an off-the-shelf design suite such as BPM is advantageous, and for our work on small angle X-couplers, we have utilised the Beamprop BPM suite developed by RSoft. The results obtained from the software are subsequently compared to the ones generated by the analytical model presented in this chapter, as will be made clearer in Chapter 6.

References:

[1] A. Ghatak and K. Thyagarajan, *Introduction to Fiber Optics*, 2nd ed: Cambridge Press, USA, 2000.

[2] D. L. Lee, *Electromagnetic principles of integrated optics*: John Wiley & Sons, USA, 1986.

[3] A. W. Snyder and J. D. Love, *Optical waveguide theory*: Kluwer Academic Publishers, United Kingdom, 1983.

[4] K. Okamoto, *Fundamentals of optical waveguides*: Academic Press, USA, 1999.

[5] E. A. J. Marcatili, "Dielectric rectangular waveguide and directional coupler for integrated optics," *Bell Systems Tech. Journal*, vol. 48, pp. 2071-2102, 1969.

[6] G. B. Hocker and W. K. Burns, "Mode dispersion in diffused channel waveguides by the effective index method," *Applied Optics*, vol. 16, pp. 113-118, 1977.

[7] J. Buus, "The effective index method and its application to semiconductor lasers," *IEEE Journal of Quantum Electronics*, vol. QE-18, pp. 1083-1089, 1982.

[8] M. Svalgaard, A. Harpoth, and T. Rosbirk, "Characterization of UV written waveguides with luminescence microscopy," *Optics Express*, vol. 13, pp. 5170-5178, 2005.

[9] I. J. G. Sparrow, "Development and applications of UV written waveguides," PhD thesis, University of Southampton, 2005.

[10] F. Ladoucer and J. D. Love, *Silica-based buried channel waveguides and devices*: Chapman & Hall, United Kingdom, 1996.

[11] F. Durr and H. Renner, "Analytical design of X-couplers," *Journal of Lightwave Technology*, vol. 23, pp. 876-885, 2005.

[12] Rsoft D. G. Inc., "BeamPROP user guide," 2005.

[13] R. Scarmozzino, A. Gopinath, R. Pregla, and S. Helfert, "Numerical techniques for modeling guided-wave photonic devices," *IEEE Journal of Selected Topics in Quantum Electronics*, vol. 6, pp. 150-162, 2000.

[14] Y. Chung and N. Dagli, "An assessment of finite difference beam propagation method," *IEEE Journal of Quantum Electronics*, vol. 26, pp. 1335-1339, 1990.

[15] I. Ilic, R. Scarmozzino, and R. M. Osgood, Jr., "Investigation of the Padé approximant-based wide-angle beam propagation method for accurate modeling of waveguiding circuits," *Journal of Lightwave Technology*, vol. 14, pp. 2813-2822, 1996.

[16] R. Kashyap, *Fiber Bragg gratings*: Academic Press, USA, 1999.

[17] A. Othonos and K. Kalli, *Fiber Bragg Gratings - Fundamentals and applications in telecommunications and sensing*: Artech House, USA, 1999.

[18] T. Erdogan, "Fiber grating spectra," *Journal of Lightwave Technology*, vol. 15, pp. 1277-1294, 1997.

[19] A. Yariv, "Coupled-mode theory for guided-wave optics," *IEEE Journal of Quantum Electronics*, vol. QE9, pp. 919-933, 1973.

Chapter 6

Small Angle X-couplers

X-couplers, also referred to as cross-couplers or crossing/intersecting waveguides, comprise two channel waveguides that overlap or intersect at a given angle. This seemingly simple arrangement forms the basic structure of many functional integrated optical devices such as switches, power dividers and wavelength selective splitters. They are also found in devices with a dense form factor such as folded planar amplifier architectures, where power coupling (or crosstalk) is to be avoided. We were primarily interested in producing ultra-compact integrated optical devices by means of using very low crosstalk small angle X-couplers as opposed to the conventional 90º crossings. It was also discovered in prior theoretical work on such structures that complete power coupling is attainable at small angles, making these structures an attractive alternative to the widely used directional couplers. This chapter will first describe a comparative study on bend loss between cosine and circular s-bends. The optimised s-bends determined from this part of the study would be used in forming the X-couplers.

6.1 S-bends

Several approaches can be used in fabricating s-bends using our direct UV writing set up, the simplest of which are based on connecting two circular bends/arcs with opposite curvatures, and the second using cosine bends. Circular bends can readily be fabricated as our G-code instruction set contains commands to perform such translation[1] or arc motion whereas the coding to produce cosine curves involved a series of μm-length straight translations that trace the cosine curve path. The definition of the s-bend parameters are depicted in Fig. 6.1.

---

[1] G2 and G3 commands (G2: clockwise circular contour; G3: counter clockwise circular contour). The instructions use curve radius as one of the input parameters.

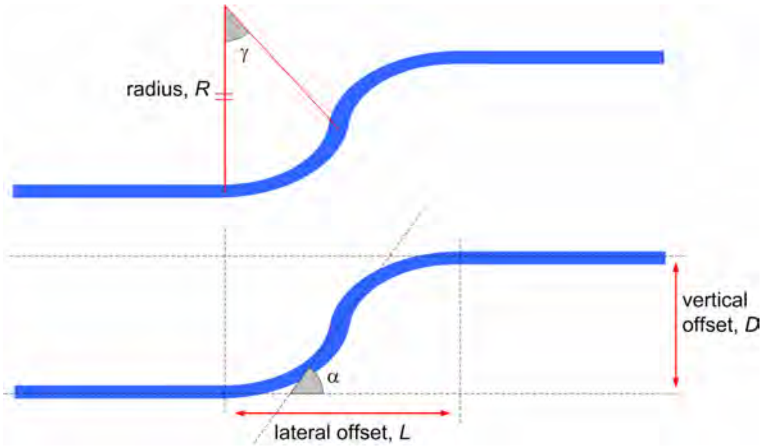

Figure 6.1 A schematic showing various s-bend parameters. α is termed the curve angle.

To allow a direct comparison between the two types of s-bends, the lateral offset of the cosine s-bend was set to be similar to its circular counterpart. The cosine bend is governed by $f(x) = (D/2)(1 - \cos(\pi x/L))$ where L is the lateral offset (m) and D is the vertical offset (m). In our design, D was set to be 100μm for both circular arc and cosine s-bends. Lateral offset values, L (m) for given vertical offset and curve radius are calculated using

$$L = \sqrt{(4RD) - D^2} \tag{6.1}$$

The vertical offset is related to the angle γ(radians) by

$$D = 4R\sin^2\left(\frac{\gamma}{2}\right) \tag{6.2}$$

It can be shown that the path lengths of the s-bends for both circular and cosine configurations are identical, hence ensuring that the two are compatible dimensionally. Path length, $s(x)$ of the circular arc s-bend is given by $2R\gamma$ whereas the cosine bend given by $f(x)$ has a path length described by

$$s(x) = \int_0^{x=L} \frac{ds(x)}{dx}dx \quad where \quad \frac{ds(x)}{dx} = \sqrt{1 + f'(x)^2} \tag{6.3}$$

There are two types of loss mechanisms associated with s-bends. The first is pure bend loss. The second is termed transition loss. Pure bend loss is caused by power radiated as light traverses an arc. This could be deduced from analysing the plane wave front behaviour of the mode as it travels around a bend. Inevitably, the outer portion of the mode will have to travel faster than the speed of light in order to ‘keep up’ with the rest of the field. The inability to do so would result in power from that portion of the mode to be radiated, causing bend loss.

The modal field distribution of an arc shifting towards the outer portion of the structure was illustrated in Fig. 2.2. This shift in peak mode intensity is often likened to the effect resulting from a skewed index profile, forming the basis of the conformal transformation technique used to quantify bend loss as presented in [1]. It is shown by Snyder and Love in [2] that the loss coefficient, γ_{bend} due to bending loss for a step index waveguide is governed by

$$\gamma_{bend} = \frac{\pi^{1/2}}{2a}\left(\frac{a}{R}\right)^{1/2} \frac{U^2}{V^2 W^{3/2} K_1^2(W)} \exp\left(-\frac{4RW^3\Delta}{3aV^2}\right) \qquad [6.4]$$

where a is the width of the waveguide, W and U are normalised waveguide parameters, and K_1 is the Bessel function of the second kind. W and U are given by [3]

$$W = a\left(\beta^2 - k_0^2 n_2^2\right)^{1/2} = V\sqrt{b} \qquad [6.5]$$

$$U = a\left(k_0^2 n_1^2 - \beta^2\right)^{1/2} = V\sqrt{1-b} \qquad [6.6]$$

and

$$V^2 = U^2 + W^2 \qquad [6.7]$$

b is defined by equation [5.41] in Chapter 5.

It is worth pointing out however, the derivation of equation [6.4] did not use the conformal transformation technique and an analogy to a current carrying antenna was utilised instead.

Transition loss takes place where a modal mismatch occurs. This again follows from the above mentioned shift of the mode peak from the propagation axis of the waveguide. The shift results in coupling inefficiencies. Expressions to calculate this peak shift can be found in [1, 2, 4] . Following from this, modal mismatch calculation via an overlap integral can be performed, leading to coupling efficiency and subsequently, the power loss formulae given below

$$1-\frac{P_O}{P_I}=\left(\frac{a}{R}\right)^2\left(\frac{r_0}{a}\right)^6\frac{V^4}{8\Delta^2} \qquad [6.8]$$

for a straight-to-curve transition loss and

$$1-\frac{P_O}{P_I}=\left(\frac{2}{R}\right)^2\left(\frac{a^2V^4}{8\Delta^2}\right)\left(\frac{r_0}{a}\right)^6 \qquad [6.9]$$

for a curve-to-curve transition loss (e.g. where two circular arcs with opposite curvatures meet). P_I and P_O are the input and output powers respectively and r_0 is the 3-dB spot size radius.

From the above equations, we could deduce that using cosine bends should be advantageous due to the following:

1. the cosine bend curvature[2] at $x=L/2$ equals to 0 and as such, produces no curve-to-curve transition loss as in the case of circular arcs;
2. due to the continuously changing curvature (hence radius) of the cosine bend, we expect to see a reduced bend loss compared to the circular arc case. However, this would also mean that quantifying the bend loss for the cosine bend analytically/numerically is elaborate and is not within the scope of this thesis. The cosine bend ($f(x)$), and its curvature with respect to position along the x-axis for a corresponding 20mm circular arc radius is shown in Fig. 6.2;
3. the cosine bends would however experience slightly larger straight-to-curve transition loss as the curvature of the bend at both extremes is larger by a few percent compared to the circular counterpart, thus increasing modal mismatch. For a circular radius of 20mm, the corresponding cosine bend radius (at $x = 0, L$) is 16.2mm, resulting in ~0.2dB higher transition loss per end point.

---

[2] Curvature, κ of a curve $f(x)$ is given by $\kappa = f''(x)/\left(1+f'(x)^2\right)^{3/2}$ where $f'(x)$ and $f''(x)$ are the first and second derivatives of the function $f(x)$. As such, at $x = L/2$, the numerator of the cosine bend equation equates to zero, implying a very large bend radius (i.e radius → ∞).

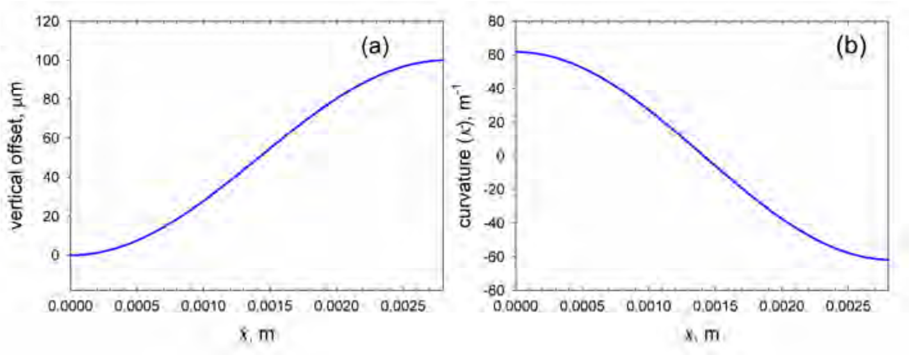

Figure 6.2 (a) Cosine bend governed by $f(x) = (D/2)\,(1-\cos(\pi x/L))$; (b) the continuously varying curvature of the cosine bend.

The modelled bend and transition loss curves shown in Fig. 6.3 used numerical aperture, spot size and cladding layer refractive index (at λ = 1550nm) values measured from the experiment described in Appendix B. These are NA_{mean} = 0.1, 3-dB spot size radius of 5.25μm and cladding index of 1.445.

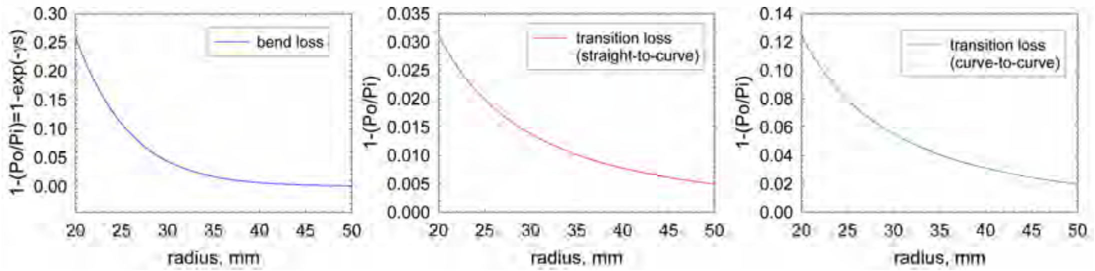

Figure 6.3 Graphs showing modelled results of pure bend loss and transition losses using measured waveguide parameters.

It can be seen that bend loss reduces exponentially with increasing radius and that for the same bend radius, the curve-to-curve transition loss is about four times larger than the curve-to-straight case. Equations [6.4, 6.8-6.9] also highlight the importance of index contrast in producing tight bends. This is among the predominant advantage of using high index material substrates where bends with μm-radius having low losses are possible, although in silica-on-silicon, this would be offset by higher propagation loss due to the levels of dopants necessary in attaining the required index contrast.

6.1.1 Experiment

Circular arc s-bend structures with radii of 20, 30, 40 and 50mm were written with a fluence of ≈ 20kJcm^{-2} on end face polished 12x18 mm^2, hydrogen-loaded samples. A corresponding set of cosine bends with parameters described in the previous sub-section were also fabricated using similar UV writing parameters. Straight channel waveguides (used as a comparative reference) were defined at the beginning and end of the UV writing session to facilitate insertion loss measurements. The UV writing duration was limited in order to minimise hydrogen out-diffusion effects. The samples were then characterised using the set up depicted in Fig. 6.4 below.

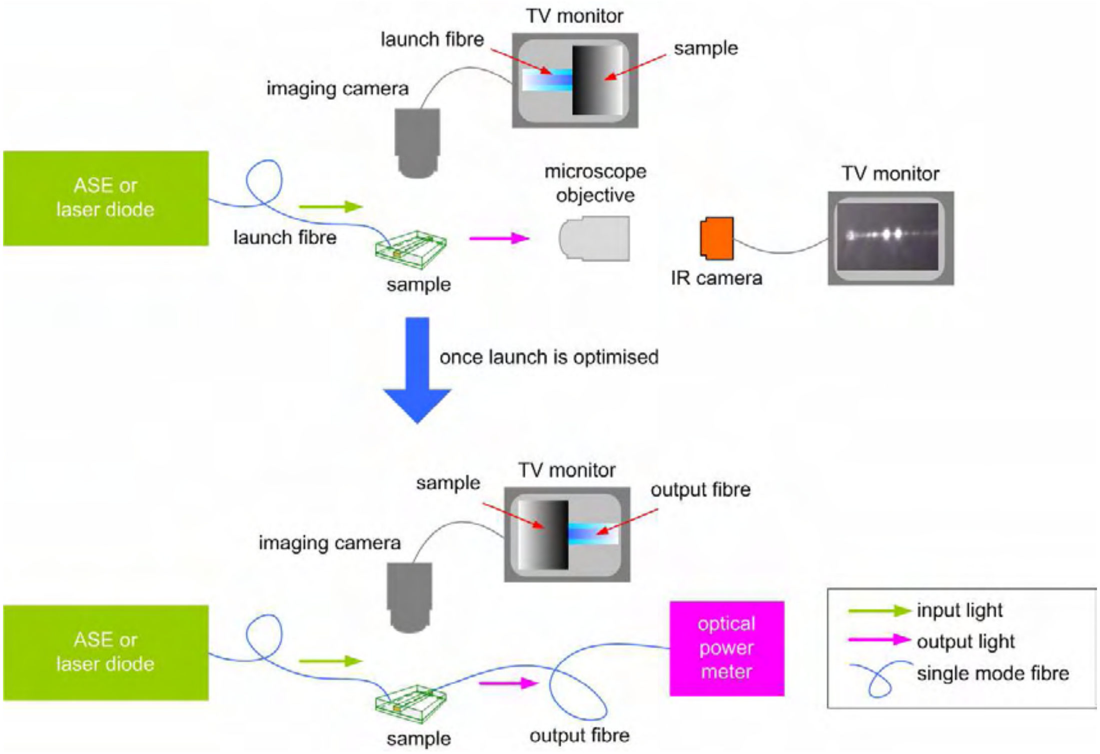

Figure 6.4 Illustration of the main elements of an experimental set up for s-bend loss measurements.

Un-polarised light from an ASE source (wavelength range: 1525-1565nm) with a maximum power of 100mW (20dBm) was input into the s-bends via single mode fibres butt coupled onto the sample input facet. The fibre was tipped with index matching fluid to prevent back reflection from the input facet. The launch fibre was mounted on a 3-axis translation stage having μm-precision while the samples were mounted on a 5-axis stage with the same resolution (the two additional axes are for the yaw and tilt translations). Optimised launching into the s-bends is achieved via a two-pronged visual approach. The first involves the use of a microscope objective (mounted on a 3-axis stage) that images the light from the output facet of the samples onto an IR camera. The IR camera is in turn connected to a monitor and successful launch into the slab waveguide and subsequently the channel structures including s-bends produces the image depicted in Fig. 6.5.

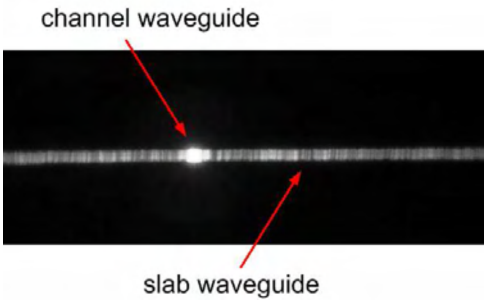

Figure 6.5 Optimised launch into channel waveguide with some scattered light in the slab waveguide as viewed by the IR camera situated along the output end of the sample.

At the same time, the position of the launch fibre with respect to the input facet of the samples and the waveguides could be determined by an imaging camera system placed above the samples equipped with high intensity illumination.

Once the launch conditions were optimised, the microscope objective was replaced by a single mode output fibre connected to a power meter. This output fibre is tipped with index matching oil and butt-coupled to the output facet of the sample. Again, the positioning of the output fibre relative to the waveguides is facilitated by the imaging camera. For each repeat measurement, the launch and output fibres were cleaved and cleaned. The input and output facets of the samples were also re-cleaned prior to each measurement run.

6.1.2 Results & Discussion

The measured and calculated fibre-to-fibre loss (dB) with respect to curve radius is depicted in Fig. 6.6. By fibre-to-fibre loss, L_{fib} (dB) we mean the difference between the power detected at the output of the s-bend, P_s (mW) to the power measured when the launch and output fibres were butt-coupled against a straight reference channel, P_{ref} (both being tipped with index matching oil)

$$L_{fib} = 10\log_{10}\left(P_s / P_{ref}\right) \qquad [6.9]$$

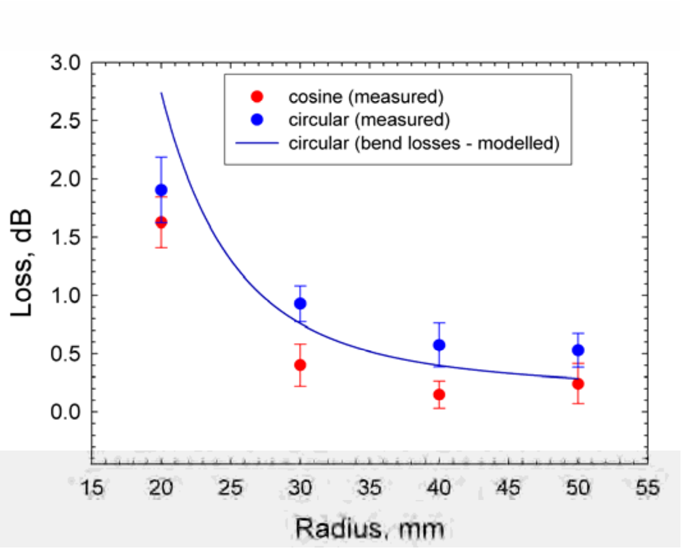

Figure 6.6 Fibre-to-fibre loss with respect to s-bend curve radius.

The insertion loss of a straight channel, η_{total} comprises the losses experienced at the input and output facets of the waveguide, η_0 and the propagation loss, $L\alpha_{prop}$, where L is the length of the waveguide and α_{prop} is the propagation loss coefficient in dB/m.

$$\eta_{total} = 2\eta_0 + L\alpha_{prop} \qquad [6.10]$$

In [5], Svalgaard decomposes η_0 into η_{spot} and η_{extra} where η_{spot} is the loss due to modal mismatch between the waveguide and the input/output fibre modes, and η_{extra} is the result of imperfections of the output facet of the waveguides, hence accounting for poor polishing quality, and the presence of absorbing materials or contaminants. However, a lot of care has been put into minimising η_{extra} not least in terms of polishing quality and cleanliness of the samples. Furthermore, the use of index matching oil would greatly reduce the effects caused by such imperfections, including, to some extent, the cleave quality of the input/output fibre. Another factor to be considered is that for all experiments, repeat measurements on multiple sets of identical structures were performed and as such, uncertainties with regards to these factors are reflected in the error bars[3] on the measured

---

[3] The error bars represent the standard deviation, σ of the data collected given by $\sigma = \left((1/N)\sum(x_i - \bar{x})^2\right)^{1/2}$ where N is the number of measurements made, $\bar{x}$ is the mean value of the measured data and i = 1…N.

results. I believe that η_{extra} could not account for more than ±0.2dB. From the same reference, I have extracted the expression for the calculation of η_{spot} (in dB) given by

$$\eta_{spot} = -10\log_{10}\frac{4\alpha_h\alpha_v\beta^2}{\left(\alpha_h^2+\beta^2\right)\left(\alpha_v^2+\beta^2\right)} \qquad [6.11]$$

where α_h, α_v are the widths (FWHM) of the waveguide modal intensity distribution in the horizontal and vertical directions respectively, and β is the width of the fibre mode. Putting α_h = 6µm and α_v = 5µm by referring to the modal profile measured via the NA experiment discussed in Appendix B, and using a typical single mode fibre mode size of 10µm, the lower limit of the insertion loss of the sample is found to be $2\eta_{spot} \cong$ 3dB[4].

As evident from Fig. 6.6, there is qualitative agreement between the measured and calculated data for the circular arc case, and performing a similar calculation for the cosine bend case would be laborious. As expected, the total losses drop with increase in radius. For all cases, circular arcs produce higher excess loss to that of the cosine, averaging 0.3dB (±0.1dB) more. This is attributed to the additional loss due to the curve-to-curve transition loss at the point of inflection of the circular s-bend, where the two circular arcs meet and the slightly lower bend loss of the cosine bend as a result of its continuously increasing curvature. The large error margins are due to imperfections in taking output power measurements, particularly in aligning the output fibre to the waveguide.

Following from these results, the cosine bends were employed for the X-coupler experiments described in the next section.

---

[4] This value is further compared to a similar expression presented by Ghatak and Thyagarajan (*Introduction to fiber optics,* page 153) where I've used the geometric mean of the channel waveguide dimension to account for asymmetry between α_h and α_v. This geometric mean is given by $\alpha_{mean} = \sqrt{\alpha_h\alpha_v}$ as outlined in Ladoucer and Love (*Silica-based buried channel waveguides and devices,* page 16). Using this approach, we obtained $2\eta_{spot} \cong$ 2.97dB.

6.2 Small Angle X-couplers

As stated earlier, X-couplers, also referred to as cross-couplers or crossing/intersecting waveguides, consist of two channel waveguides that overlap or intersect at a given angle. This arrangement forms the basic structure of many functional integrated optical devices such as switches, power dividers and wavelength selective splitters. X-couplers are attractive in terms of fabrication tolerance as the desired coupling ratio of the device can be achieved with a much shorter interaction length and there is no need for the finite waveguide separation necessary in conventional coupler architectures.

Fabrication of small angle (<5°) X-couplers in silica-on-silicon using photolithography and etching remains challenging due to the existence of under-etched regions (or blunts) within the vicinity where the two waveguides meet and separate [6]. These blunts contribute towards unwanted reflections and surface roughness, resulting in higher insertion loss and polarisation dependence. Hoffman et al [7] addressed this problem by employing very thin (0.35μm) strip loaded channels which are therefore simpler to etch without creating blunts but do not use the industry standard approach for silica-on-silicon waveguides. Overcladding step coverage problems known as voids are also known to cause problems in the fabrication of closely spaced waveguide cores via etching [8, 9]. UV writing provides the means to overcome such problems and could allow smooth crossings with arbitrarily small angles. Another significant advantage of our technique is the ability to achieve an index increase in the waist region due to repeated illumination which is necessary for near lossless X-coupler operation, as described in Chapter 5. To achieve the same condition via photolithography would require an additional fabrication step and very accurate control of material doping. The UV-written X-coupler and its associated parameters are illustrated in Fig. 6.7.

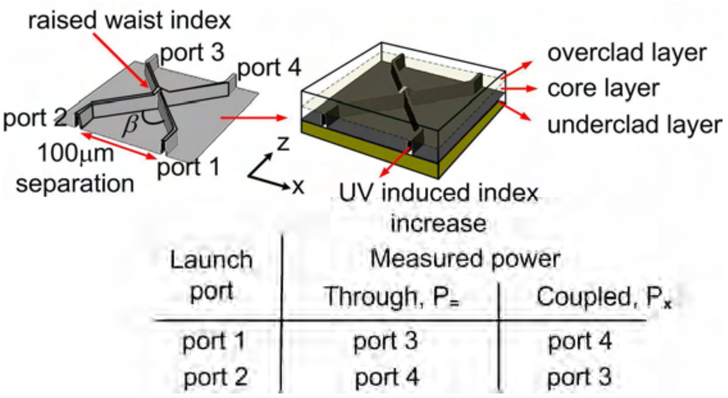

Launch port	Measured power	
	Through, $P_=$	Coupled, P_x
port 1	port 3	port 4
port 2	port 4	port 3

Figure 6.7 X-coupler parameters. Notice the raised index of the waist section. The definition of coupled, P_x and through, $P_=$ power is also provided.

Numerous experimental studies on X-couplers in various material platforms including silica-on-silicon are available. Some of these studies are reviewed in Table 6.1.

Table 6.1 Comparison between various X-coupler experimental studies.

Ref.	**Material**	**Waveguide definition technique (type of waveguide)**	**Range of crossing angles**	**Coupling ratio or crosstalk**[a]
[6]	Silica-on-silicon (FHD)	Photolithography and etching (buried channel)	4° to 18°	-40 to -5 dB
[7]	Silica-on-silicon (PECVD)	Photolithography and etching (strip loaded)	0.2° to 0.7°	-36 to 0 dB
[10, 11]	Corning 0215 bulk glass	Femtosecond direct write (buried channel)	1° to 4°	50% at 1°, 6% at 4°
[12]	Indium-phosphide	MOVPE[b] and etching (rib waveguides)	10° to 90°	n/a

[a] Coupling ratio, CR is defined as $CR = P_x/(P_x+P_=)$. Crosstalk (dB) is defined as $10\text{Log}_{10}(CR)$;

[b] MOVPE = metal organic vapour phase epitaxy.

Comparative work by Przyrembel and Kuhlow [6] is the most similar to ours in terms of material system (SiO_2:Si) and waveguide dimensions (4 and 6μm wide). In their work, allowance for under etching was needed by means of the lithography mask used. The existence of such an issue is probably the reason why the lower limit for their device crossing angle is 4°. Furthermore, the devices fabricated do not possess a raised index waist, and as such, according to the analysis presented in the previous chapter, would display a lower insertion loss fundamental limit of 3dB.

A number of theoretical studies of X-couplers also exist, for example in references [13-16]. Agrawal et al for example, postulated in [16] that the coupling behaviour of a double-Δn type crossing waveguides (which is a specific raised waist index case), display a similar decreasing frequency behaviour as shown in Fig. 5.9(a). In [17], Gerard et al suggested that ~90% coupling could be attained for β as large as 11°. However, his analysis is based on a different material system. Consequently, it is important to validate these models experimentally for the case of direct UV writing.

6.2.1 Analytical & BPM Modelling

As mentioned in the previous chapter, I have utilised BPM as a post-fabrication analysis tool to analyse, understand and subsequently obtain various device parameters. In the case of X-couplers, we have also compared the experimental results with the analytical model provided by Durr and Renner [13] (as described in Chapter 5). For the BPM modelling, a commercially available RSoft Beamprop and CAD suite (version 5.1) was used. 2D scalar simulations of the structures were conducted by first obtaining a slab approximation of the 3 layer sample via the effective index method, resulting in an underclad effective index of 1.4486 (λ=1550nm, underclad index of 1.445, a non-UV exposed core layer index of 1.45). These values were also used in the analytical model.

For the UV-written channels, a step index profile was assumed and the BPM add mode feature was utilised where the two channels overlap, allowing a raised index profile of the waist segment (shown in Fig. 6.7). A quadratic index tapering along the direction of propagation ensures smooth index increase in the regions within the vicinity of the waist, avoiding unnecessary light scattering. This behaviour was later confirmed by the proximity effect experiments presented in Chapter 7 where maximum index increase is achieved where the region is multi-exposed and this increase in index effect is present up to two waveguide widths away. BPM simulations for three distinct cases are shown in Fig. 6.8.

Automatic tilt was used for the BPM launch and monitor, with Padé order (1,1) and reference k (wavevector) representing each channel’s angular offset. Simple Transparent Boundary Condition ensures that radiated light from the structure is not reflected back at the calculation boundaries. A convergence study was conducted to optimise the above simulation parameters. The power monitor gives an overlap integral between the launch mode and the evolving mode profile. To assess the loss of the device, the total power monitor feature was also employed.

Here, the simulation was optimised in order to display the varying levels of scattering in the waist area with respect to its modal characteristics, and also the resulting insertion loss of the structure. The waist length over which index tapering takes place was taken to be 2000µm so as to ensure a very shallow taper, preventing light scattering originating from the tilted waveguides. A Total Power BPM monitor sums the output power of the structure. For the simulation, absolute UV induced index change as large as 1.5×10^{-3} was used and parameter scanning was employed to match the results to experimental ones. The progress from one operating regime to another depends on the effective index and physical dimensions of the fabricated structure.

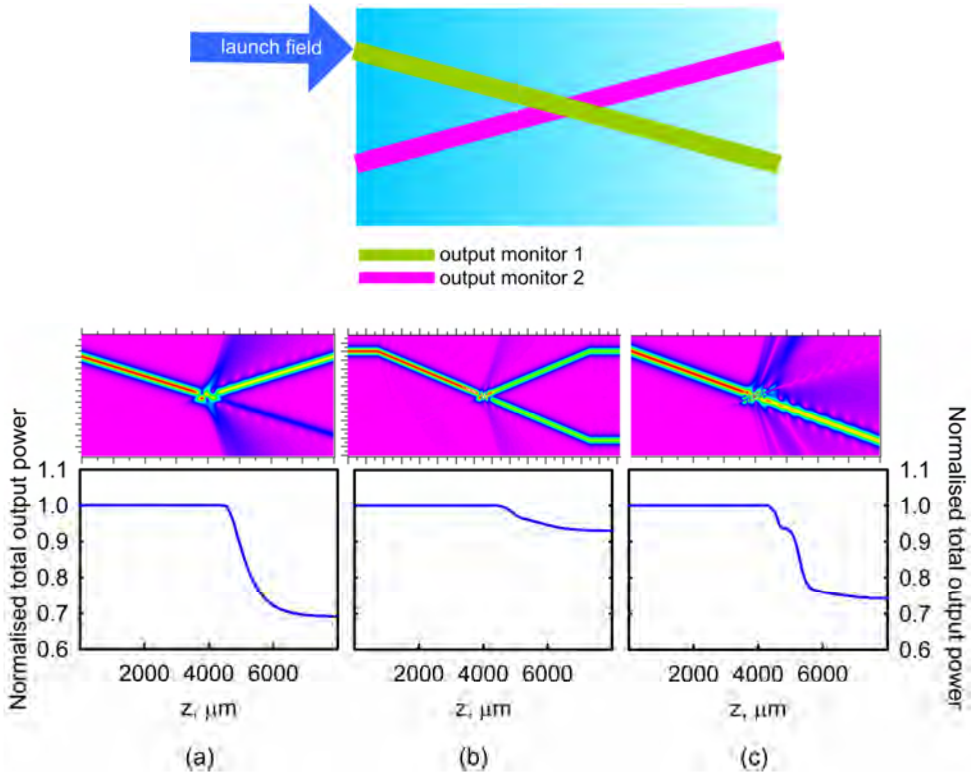

Figure 6.8 Examples of BPM simulation of 1° crossing angle X-couplers with various waist index values. The topmost schematic shows the control case X-coupler and the locations of the launch field and the various power monitors. The solid line graphs below the BPM depiction of the field distribution along the X-coupler are obtained using the Total Power monitor. Figs. 6.8 (a) and (c) show at least 30% and 25% radiated power respectively, while case (b), corresponding to the ideal case, shows about 5% (~0.2dB) radiated loss.

The structure in Fig. 6.8(a) is the single-Δn case whereas structures (b) and (c) guide two (ideal case) and three supermodes respectively within the waist region. It can be seen that a near lossless operation could be achieved if the waist index modal characteristics fits the model in [13] such as the one shown in (b). A total power drop of ~30% can be seen from the two non-ideal cases where the waist segment is either single mode (Fig. 6.8(a)) or highly multi mode (Fig. 6.8(c)) whereas minimal insertion loss is displayed by the X-coupler shown in Fig. 6.8(b). For the BPM results presented in Figs. 6.10 and 6.11 below, the complete X-coupler structure, including the waveguide bends, such as the one in Fig. 6.8(b) was used and some of the losses are attributed to transition and bend losses from the waveguide bends.

6.2.2 Experiment

For this study, multiple UV-written structures were fabricated including 14 X-couplers with crossing angles of between 0.8° and 5° and a straight reference channel waveguide. To begin with, each substrate was diced and the shorter end facets of the samples were polished to optical quality and the samples were hydrogen loaded at >120bar for a minimum of 3 weeks to increase photosensitivity (see Chapter 4). The total writing time was limited to reduce detrimental effects resulting from hydrogen out-diffusion.

In order to expose the buried channel waveguide structures for imaging purposes, additional samples were fabricated. The overclad layer of these samples was chemically wet etched using 48% hydrofluoric (HF) solution. The waveguide width, measured from SEM imaging, is 4µm (±0.5µm) and Fig. 6.9(a) depicts a x10 microscope image of one of the fabricated structures. Fig. 6.9(b) shows a surface profiler image of the same structure indicating smooth crossing (i.e. no step coverage and blunts). One interesting observation from these images is the dip where the sample was UV-written suggesting a higher etch rate to the un-exposed sample region. This is probably a feature that is unique to the samples used for this experiment.

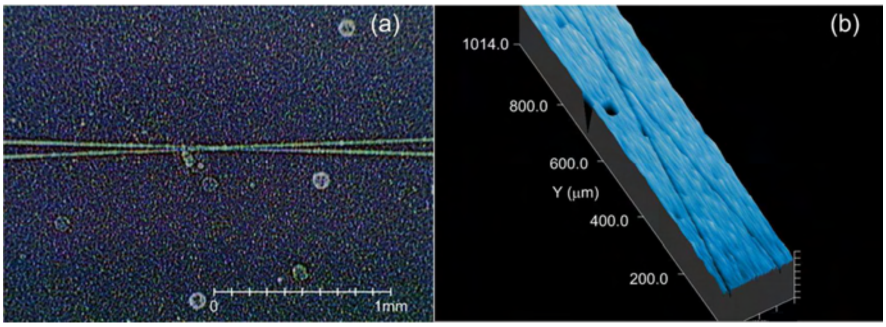

Figure 6.9 Microscope and surface profiler images of a UV-written X-coupler that has been etched to reveal the device structure. (a) x10 microscope image of X-coupler and (b) surface profiler image of the same structure indicating smooth crossing.

For the characterisation of the X-couplers, the set up similar to the one depicted in Fig. 6.4 was utilised, with minor additions. Two light sources were used. For un-polarised light and wavelength dependency measurements, an ~80µW Agilent 83437A broadband source with output wavelength range of 1250-1600nm (350nm spectral width) was used. For polarisation sensitivity measurements, a ~100mW 1520-1560nm EDFA ASE source (40nm spectral width) and polariser were used. The in-fibre polariser was in turn connected to a fibre-spool polarisation controller. Optimum TE and TM launching was ensured prior to the characterisation of the X-couplers. Standard single-mode (SMF-28) input and output fibres were butt-coupled to the respective end faces of the sample and tipped with index matching oil to prevent unwanted reflections. Each sample was mounted onto a 5-axis stage with the three main axis (x, y, z) being piezo-controlled. A camera system such as the one described in Section 6.1.1 was utilised to assess the fibres position with respect to the X-couplers input and output ports. During both the wavelength and polarisation sensitivity analyses, multiple measurements were taken to account for experimental errors such as launch conditions and end-face quality. For each repeat measurement, the sample and fibres were re-cleaned and fibre-to-fibre power measurements taken. Transmitted light was measured using either a power meter or an optical spectrum analyser (OSA) for spectral analysis. Typical excess loss of the X-couplers with respect to a straight reference channel was 1.0 (±0.25) dB at λ=1550nm.

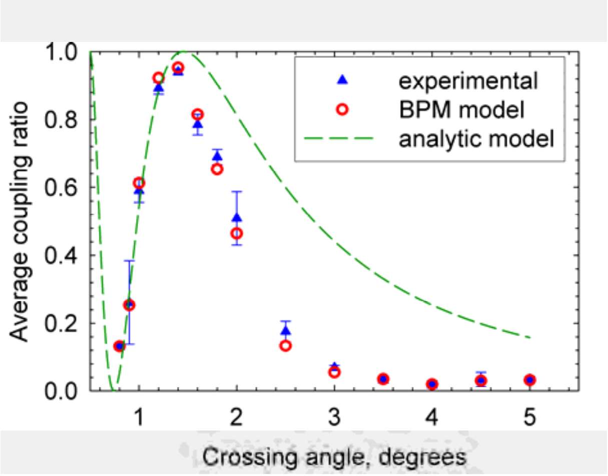

Figure 6.10 Coupling ratio behaviour with respect to X-coupler crossing angle. The BPM data shows excellent agreement with those measured while the analytical model curve agrees well at small angles only.

6.2.3 Results & Discussion

In Fig. 6.10, the X-couplers show a similar trend for changes in coupling ratio with respect to crossing angle as described by [13, 16]. In principle, there exist 3 operating regimes, the first being for crossing angles <1° which is characterised by rapidly oscillating coupling with angle. The second operating regime, with crossing angle between 1.0° and 1.5° is typified by a steep coupling ratio curve. The analytical model shows excellent agreement with our experimental results for angles within regimes 1 and 2. The disagreement outside these regions results from the analytical model only predicting coupling behaviour for a structure with a gradual enough waveguide inclination to maintain adiabatic evolution and allow radiation mode coupling effects to be neglected.

Results from the BPM simulation are also shown in Fig. 6.10 and the simulated results show excellent agreement with our experiment. In getting the best fit, allowance for hydrogen out-diffusion has to be incorporated into the model through reduction in the UV-written refractive index values. Structures written at the start of the fabrication run, in our case the X-coupler with β = 0.8°, have higher UV induced refractive index compared to those written towards the end of the run. Channel effective index decrease as much as 2x10^{-4} was used for the above purpose. This effective index reduction is quantitatively in agreement with the hydrogen out-diffusion experiments by Sparrow described in Chapter 4 [18].

Strong coupling is to be expected in regime 2 and in our devices, 95% (±0.8%) of input light was coupled with a 1.4° crossing angle. In the third regime ($\beta \geq$ 1.5°), coupling decreases gradually and coupling becomes very low (<0.3%), making the structure well suited for passive crossings. In our case, the lowest coupling ratio is 1.9% (±1%) at a 4° crossing angle.

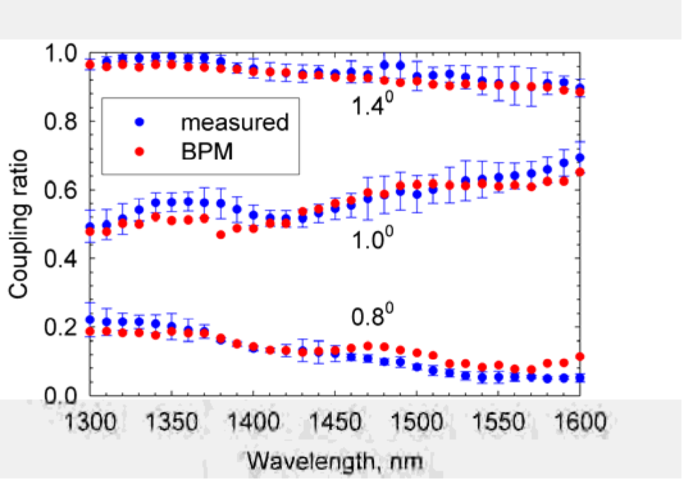

Figure 6.11 Wavelength dependencies of X-couplers for 3 different crossing angles.

The measured wavelength dependency of the characterised structures, together with the BPM simulated behaviour, is shown in Fig. 6.11, indicating excellent agreement between the two. Discrepancies between simulated and measured data can be minimised by fine tuning the refractive index values of the UV-written channels and waist segment, and optimising input launch conditions, although this would not add to the accuracy of the general trend shown. The different error levels with wavelength for all three X-couplers result from the nature of the input and output light spectrum as shown in Fig. 6.12, having intensity dips at around 1370, 1480 and 1600nm. At these wavelengths, the measurements tend to be very noisy as the level of output light is close to the noise floor.

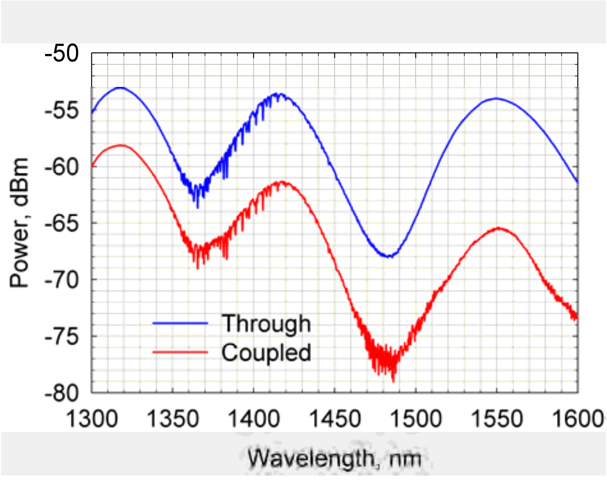

Figure 6.12 Typical through and coupled power spectrum showing intensity dips at around 1370, 1480 and 1600nm.

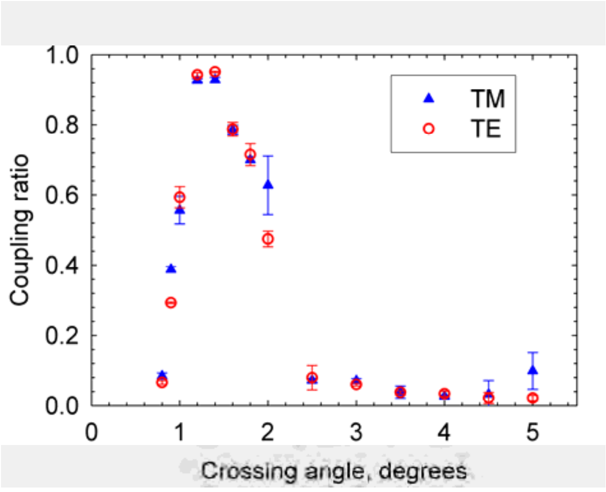

Figure 6.13 Graph showing the coupling ratio against crossing angle using polarised input light, highlighting the low polarisation dependence of the structure.

The coupling ratio for two orthogonally polarised sources is depicted in Fig. 6.13. Here, the X-couplers display almost indistinguishable coupling behaviour for both TE and TM modes. Such low polarisation dependence demonstrates the smooth transition between the two overlapping UV-written waveguides that form the X-couplers. It is widely known that blunts are a major source of polarisation dependency due to a difference in scattering levels between the horizontally and vertically polarised signals, an effect not seen in our structures.

6.3 Tuning of Coupling Ratio via Asymmetry

Having demonstrated the advantageous features of the direct UV-written X-couplers, the next goal was to employ asymmetry in tuning the coupling behaviour of X-couplers, enabling fabrication of cascaded devices such as 1xN splitters for use in WDM networks for example. DUW allows us two degrees of freedom in producing asymmetry, 1) dimensional (waveguide width) asymmetry is achieved by defocusing the UV laser to change the writing spot size, and 2) refractive index asymmetry is achieved by varying the writing speed.

A schematic of an asymmetric X-coupler is depicted in Fig. 6.14, highlighting the two s-bends that form the structure and the segment where asymmetry is introduced.

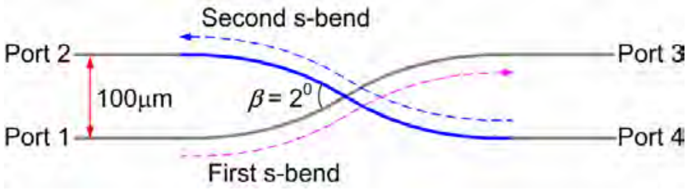

Figure 6.14 A schematic representation of the fabricated UV-written X-couplers with 2° crossing angle. The two s-bends forming the X-coupler are shown and the second s-bends were written with various fluence values.

6.3.1 Experiment

The X-couplers fabricated for this experiment each have a 2° crossing angle (β =2°). The second s-bend was written with various fluence levels, creating asymmetry in terms of UV induced index increase. The fluence of the first s-bend and all input and output ports was fixed at ~25.5 kJcm^{-2} and those of the second s-bend were varied from 17.0 - 25.5 kJcm^{-2}, the latter of which forms a symmetric structure for comparison.

The fabricated devices were then characterised using a similar approach to that presented in the previous section.

6.3.2 Results & Discussion

The coupling ratio, insertion loss (relative to the loss of a straight channel waveguide) and polarisation dependent loss (PDL) performance of the X-couplers with polarised input ASE launched into Port 1 is shown in Fig. 6.15.

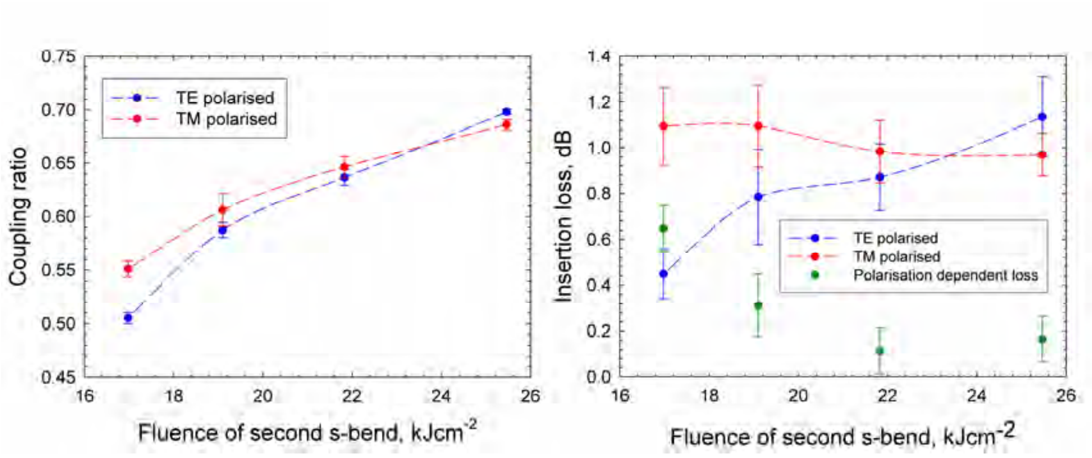

Figure 6.15 Coupling ratio and insertion loss of X-couplers with various second s-bend UV writing fluence values highlighting the effects of index asymmetry of the structure (dotted lines: for indicative purpose only).

As the asymmetry level increases, so does the difference in coupling ratio for the two polarisation cases, with a maximum difference of ~5% over the fluence range used. This low polarisation dependence is possibly due to the absence of under-etched regions in the vicinity where the two s-bends meet, as would occur in conventional etched devices.

It could be seen that the coupling ratio varies from a maximum of ~70% (symmetric case) to 50% (highest asymmetry case). 50% coupling ratio is ideal for cascaded 1xN splitting applications and the ~20% coupling ratio tunability achieved highlights the viability of tunable X-couplers over C-band wavelengths (λ = 1520-1560nm). This stems from the coupling behaviour of X-couplers being dependent on the refractive index of the waist. As such, the ability to manipulate the waist index by forming an etched window over the waist and manipulating the index via liquid crystal overlays for example, would be a possible way to achieve beam switching.

Polarisation dependent loss (PDL) increases with asymmetry, the highest being ~0.65dB, obtained with highest asymmetry. An interesting behaviour worth pointing out is the reduction in insertion loss of the device with asymmetry for TE polarisation. We believe this is due to the increase in mode conversion efficiency moving away from symmetry, ensuring adiabatic mode evolution across the coupler [19]. Very low PDL (<0.2dB) and coupling ratio difference (<1%) were displayed as we move closer to symmetry, highlighting the polarisation insensitivity of the devices.

The wavelength dependence of the structures was also characterised, the results of which are shown in Fig. 6.16.

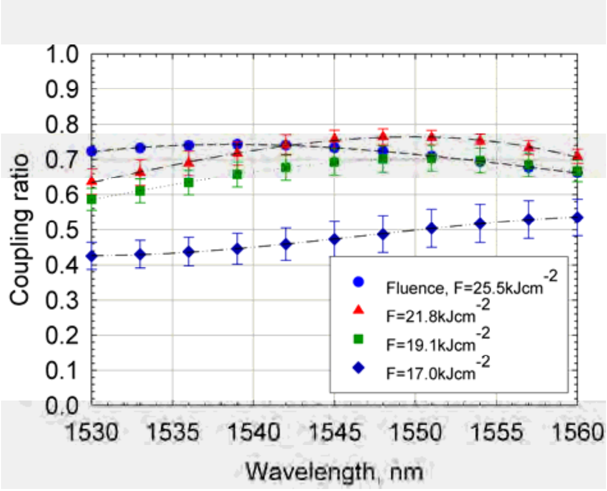

Figure 6.16 Wavelength dependencies of asymmetric X-couplers. The legend indicates the fluence values of the second s-bend.

6.4 Summary

The advantages offered by direct UV-written X-couplers are 1) they possess a raised refractive index waist, facilitating near lossless operation, 2) the ability to tune the coupling ratio via asymmetry, highlighting post-fabrication capabilities, and 3) low wavelength and polarisation dependence. These X-couplers do not suffer from blunts and under-etching, and show good agreement with simulated data.

Specifically, we have experimentally demonstrated the power coupling behaviour of small angle X-couplers with respective maximum and minimum coupling ratios of 95% (±0.8%) and 1.9% (±1%). A low wavelength dependency over 300nm was also obtained, highlighting the potential for broadband operation. Polarisation dependence of the couplers is extremely low, an effect attributed to the smooth waveguide crossing intersections made possible by UV writing. Device operation was simulated using both BPM and analytical model and the experimental results show good agreement with the simulated behaviour. UV writing seems to present an ideal route towards attaining a suitable waist refractive index increase for lossless operation. An improved understanding of fabrication parameters will allow future implementation of custom designed X-couplers based on the UV writing fabrication platform.

In addition to this, we have also demonstrated 20% coupling ratio tuning via waveguide asymmetry, with stable operation over 30nm C-band spectral range. As such, the ability to manipulate the waist index by forming an etched window over the waist and manipulating the index via liquid crystal for example, would be a way to beam switching (see Chapter 10).

References:

[1] F. Ladouceur and P. Labeye, "New general approach to optical waveguide path design," *Journal of Lightwave Technology*, vol. 13, pp. 481-492, 1995.

[2] A. W. Snyder and J. D. Love, *Optical waveguide theory*: Kluwer Academic Publishers, United Kingdom, 1983.

[3] A. Ghatak and K. Thyagarajan, *Introduction to Fiber Optics*, 2nd ed: Cambridge Press, USA, 2000.

[4] T. Kitoh, N. Takato, M. Yasu, and M. Kawachi, "Bending loss reduction in silica-based waveguides by using lateral offsets," *Journal of Lightwave Technology*, vol. 13, pp. 555-562, 1995.

[5] M. Svalgaard, "Ultraviolet light induced refractive index structures in germanosilica," PhD thesis, Technical University of Denmark, 1997.

[6] G. Przyrembel and B. Kuhlow, "Waveguide crossings with low crosstalk at small angles," *Electronics Letters*, vol. 38, pp. 1533-1535, 2002.

[7] M. Hoffmann, P. Kopka, and E. Voges, "Thermooptical digital switch arrays in silica-on-silicon with defined zero-voltage state," *Journal of Lightwave Technology*, vol. 16, pp. 395-400, 1998.

[8] M. Olivero and M. Svalgaard, "Direct UV-written broadband directional planar waveguide couplers," *Optics Express*, vol. 13, pp. 8390-8399, 2005.

[9] M. Svalgaard and M. Kristensen, "Directly UV-written silica-on-silicon planar waveguides with low loss," *Electronics Letters*, vol. 33, pp. 861-863, 1997.

[10] K. Minoshima, A. M. Kowalevicz, E. P. Ippen, and J. G. Fujimoto, "Fabrication of coupled mode photonic devices in glass by nonlinear femtosecond laser materials processing," *Optics Express*, vol. 10, pp. 645-652, 2002.

[11] K. Minoshima, A. M. Kowalevicz, I. Hartl, E. P. Ippen, and J. G. Fujimoto, "Photonic device fabrication in glass by use of nonlinear materials processing with a femtosecond laser oscillator," *Optics Letters*, vol. 26, pp. 1516-1518, 2001.

[12] H. G. Bukkems, C. G. P. Herben, M. K. Smit, F. H. Groen, and I. Moerman, "Minimization of the loss of intersecting waveguides in InP-based photonic integrated circuits," *IEEE Photonics Technology Letters*, vol. 11, pp. 1420-1422, 1999.

[13] F. Durr and H. Renner, "Analytical design of X-couplers," *Journal of Lightwave Technology*, vol. 23, pp. 876-885, 2005.

[14] S. Gevorgyan and A. Hovsepyan, "Power distribution in symmetric integrated optic X junction," *Electronics Letters*, vol. 26, pp. 788-789, 1990.

[15] R. A. Forber and E. Marom, "Symmetric directional coupler switches," *IEEE Journal of Quantum Electronics*, vol. QE-22, pp. 911-919, 1986.

[16] N. Agrawal, L. McCaughan, and S. R. Seshadri, "A multiple scattering interaction analysis of intersecting waveguides," *Journal of Applied Physics*, vol. 62, pp. 2187-2193, 1987.

[17] P. Gerard, P. Benech, and R. Rimet, "Intersecting waveguide modelization for any angle and guiding conditions with the radiation spectrum method," *Optics Communications*, vol. 124, pp. 165-174, 1996.

[18] I. J. G. Sparrow, "Development and applications of UV-written waveguides," PhD thesis, University of Southampton, 2005.

[19] W. K. Burns, A. F. Milton, A. B. Lee, and E. J. West, "Optical modal evolution 3-dB coupler," *Applied Optics*, vol. 15, pp. 1053-1065, 1976.

Chapter 7

Bragg Gratings as an Assessment Tool

Until this point, the work presented has involved structures, devices and experiments that do not make use of Bragg gratings. Earlier in this thesis, the potential applications of this important structure were discussed, and the theoretical aspects governing grating performance were examined. In this chapter, the use of the Bragg grating in assessing substrate characteristics and behaviours is described. This includes the measurement of the substrate photosensitive response to UV writing dosage, normally termed ‘the fluence test’. The ability to use gratings to determine substrate birefringence is also demonstrated by deducing the difference in effective refractive index for TE and TM polarised light by interrogating the grating reflection peak wavelength. Finally, we will describe the first quantification of the ‘proximity effect’, which is the key mechanism in producing the raised refractive index waist X-couplers presented in the previous chapter, as well as the refractive index tapering effect experienced by the waveguides approaching the waist segment.

7.1 Producing the Bragg Grating

A brief description of our Direct Grating Writing (DGW) set up has been provided in Chapter 3. In this chapter, we will take a closer look at the various issues governing the successful fabrication of Bragg gratings. The main parameters of interest are the duty cycle, grating length, and the number of reflection planes contained within the grating length. A schematic depiction of the DGW technique is shown in Fig. 7.1.

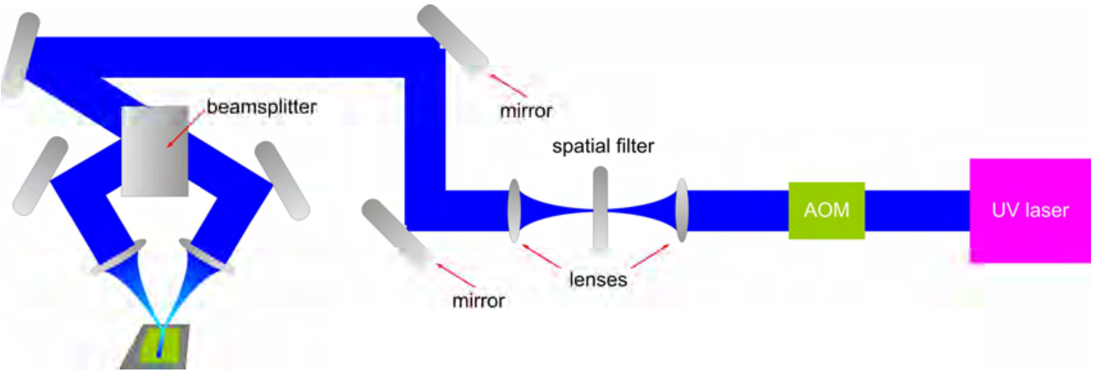

(a)

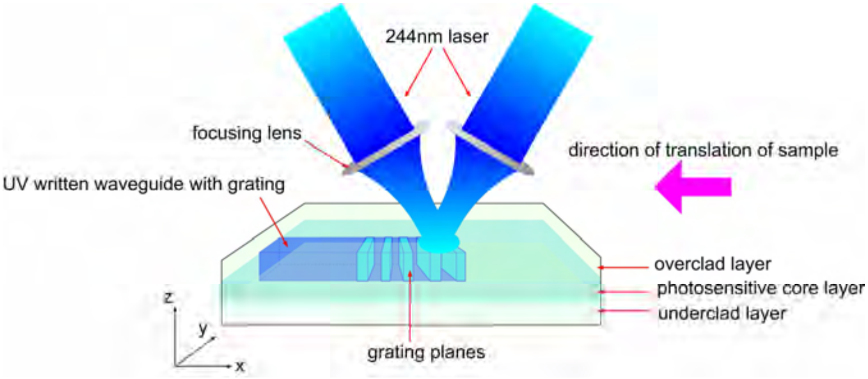

(b)

Figure 7. 1 Schematic of the Direct Grating Writing technique. The angle between the two beams is ~26°.

The period of the interference fringes, Λ_{spot} generated by the crossed UV beams is obtained using the known interference expression below

$$\Lambda_{spot} = \frac{\lambda_{UV}}{2\sin(\theta/2)} \qquad [7.1]$$

where λ_{UV} = 244 nm, and θ is the angle between the crossing beams. For our case, θ is ~26°, leading to Λ_{spot} = 542nm. An overlapping beam waist diameter of ~4.5µm would therefore contain approximately 7 grating periods.

With reference to Fig. 7.1(a), the inclusion of an acousto-optic modulator (AOM) within the DGW set up enables the modulation of the UV exposure. Briefly, when switched on, the AOM will diffract the incoming 244nm light, and this is governed by [1]

$$\Lambda_{AOM} = \frac{m\lambda_{UV}}{\left(\sin\left(\frac{\theta_m}{2}\right) - \sin\theta_i\right)} \qquad [7.2]$$

where $m = 0, \pm1, \pm2$ and so on is the diffraction order, Λ_{AOM} is the period of the standing wave created in the AOM, $\theta_m/2$ is the angle of the diffracted order and θ_i is the angle of incident of the UV beam. The 1st diffraction order was chosen for our set up as it typically has a high extinction ratio approaching 100% whereas the 0th order diffraction would only display ~20% extinction. The latter case would translate into an inability to turn off the laser beam completely, thus affecting the overall UV-written structure.

The term ‘duty cycle’ is introduced to describe the degree of modulation of the UV beam as the grating is being written. Analogous to the meaning of the term in electronics, duty cycle in this case represents the ratio between the time when the laser is on to the time when the laser is off over the space of a single exposure. Clearly, for the same writing translation speed setting, the grating plane modulation reduces with increase in duty cycle. As the duty cycle approaches 100%, channel waveguides are produced instead of gratings.

The planar Bragg gratings in this work are generally fluence matched, which means that the average refractive index of the grating section, $\overline{\delta n}_{eff}$ is designed to be equal to the UV induced index increase of the channel leading up to the grating section. This is attained by ensuring that the translation speed during grating writing is related to the duty cycle, that is $v_{grating} = \delta \times v_{channel}$ where $v_{grating}$ is the grating writing speed (mm/minute), δ is the duty cycle and $v_{channel}$ is the translation speed (mm/minute) used to define the channel waveguides before and after the grating section.

In this work, a 50% duty cycle was chosen for all the experiments involving Bragg gratings because firstly, the grating response is sufficiently large (> 10dB with respect to the reflected noise levels) and secondly, there is a trade-off between grating strength and the need to minimise hydrogen out-diffusion effects. Intuitively, and as shown in the work by Emmerson [2], smaller duty cycles lead to stronger grating reflections resulting from the higher index contrast. However, if the gratings are to be fluence matched, using a small duty cycle would also require much longer grating writing times, limiting the number of devices that can be written onto the substrate and introducing out-diffusion related variability in the results obtained. It is worth mentioning ongoing work by my research colleague, Christopher Holmes that is geared towards addressing this out-diffusion issue by means of a cold chuck (chamber). By cooling the samples, the UV writing time may be significantly extended.

Typically, our gratings are 1 – 1.5 mm long. The number of grating planes or index perturbations, N contained within a given grating length, L (mm) is given simply by $N = L/\Lambda$ where Λ is the grating period. In the case of a 1mm grating, N is $\cong$ 1800. Assuming a $\overline{\delta n}_{eff}$ of a similar magnitude to that of a typical UV induced index increase of a single channel, that is ~ $5\text{x}10^{-3}$, we will obtain a theoretical κL value of 10 at λ = 1550nm and with fringe visibility, γ of 1 (see reference [3] and equation [5.58] in Chapter 5 of this thesis). This would result in a 100% reflectivity with a bandwidth, $\Delta\lambda_0$ of ~ $2\lambda/N \cong$ 2nm. However, the gratings used in this thesis typically display < 1dB transmission dips, corresponding to less than 30% reflectivity. This is not surprising given the length of the gratings used, and the 50% duty cycle. Typical reflection and transmission spectra are shown in Fig. 7.2.

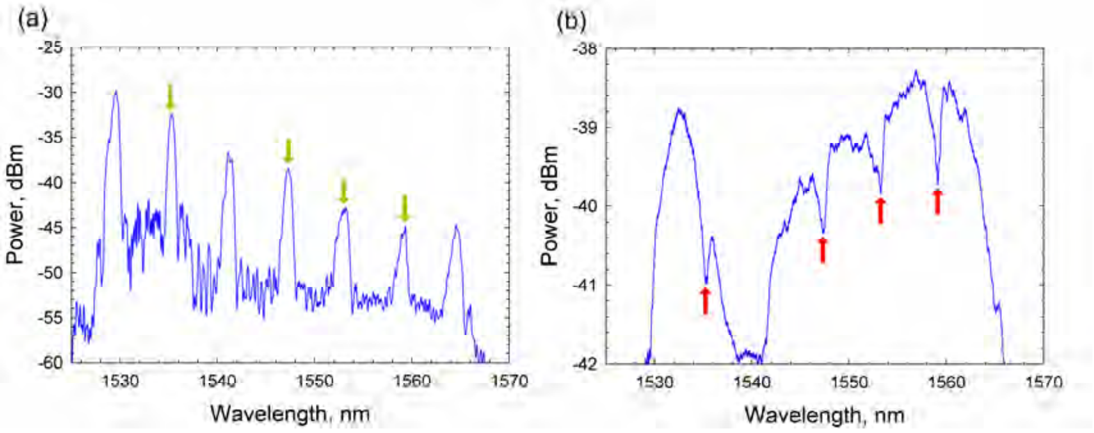

Figure 7.2 Graph showing (a) reflection and (b) transmission spectra of a series of 1mm gratings direct UV-written with UV beam power of 50mW and 50% duty cycle (arrows indicate the corresponding reflection peaks and transmission dips).

Using the above spectra, the estimated $\overline{\delta n}_{eff}$ is of the order ~10^{-4} (assuming $\gamma = 1$). However, as stressed earlier, for the type of experiments and devices investigated in this work, which involve interrogating the grating in reflection mode, the level of power reflection and bandwidth obtained from our normal 1mm gratings is sufficient.

We will next turn our attention to a few experiments that provide a better understanding of the substrates we employ in terms of photosensitivity and birefringence. The FHD substrates we used were supplied by the Centre for Integrated Photonics (CIP), with typical parameters outlined in Table 7.1.

Table 7.1 FHD substrate specifications.

Wafer number	Layers	Thickness (μm)	Refractive index (λ = 1550nm)
DN423/ 1, 2, and 3	Overclad: FHD	18.5	1.4449
	Core: FHD	5.6	1.4452
	Underclad: thermal oxide	15.9	1.4450
DN426/ 2, 3, and 4	Overclad: FHD	18.4	1.4446
	Core: FHD	5.8	1.4449
	Underclad: FHD	18.5	1.4449
	Thermal oxide layer	6.0	1.4450

7.2 Experiment

For the fluence test and birefringence experiments, a series of 50% duty cycle, fluence-matched 1mm gratings were written at various fluence values. The samples were hydrogen loaded prior to UV writing and each substrate measured 10 x 20mm^2. All four sides of the samples were polished and for these experiments, the gratings were written along the shorter sample axis.

After UV writing, the gratings were characterised using the set up depicted in Fig. 7.3. Clearly, the set up is very similar to the one described in Chapter 6, and uses the same two-pronged visual approach for ensuring optimised launching.

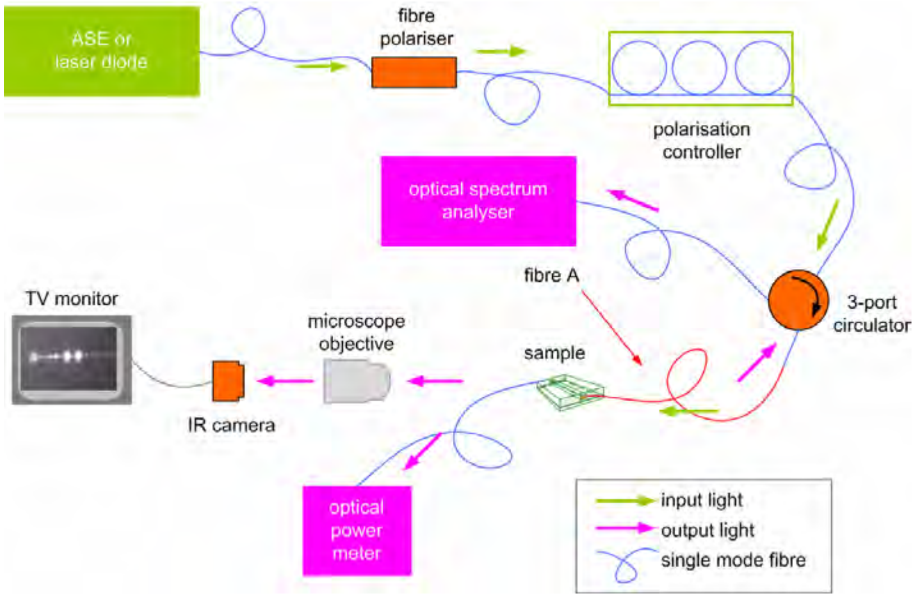

Figure 7.3 Illustration of the experimental set up used to assess planar Bragg grating reflection spectra.

Controlled polarisation of input light is achieved by employing a fibre polariser and fibre-spool polarisation controller. The input light, as indicated by the green arrows, will pass through a 3-port circulator before reaching the sample. During the later stages of this research, the standard single-mode input fibre (labelled fibre A) was replaced by a polarisation maintaining fibre. The reflected light (pink arrows) from the grating is output from the third port of the circulator and assessment of the grating spectrum is achieved by connecting this output into an optical spectrum analyser (OSA). At the same time, the launch quality can be checked by inspecting the transmission image captured by the IR camera.

In obtaining the grating transmission spectrum, the objective-camera assembly is replaced by a single mode fibre connected to another OSA. To simplify the process of locating the optimum position on the output facet of the waveguide, the output fibre was first connected to a power meter prior to the OSA (as shown in Fig. 7.3). A power meter is sensitive enough to enable us to differentiate between the power emitting from the slab waveguide, and the power within the channel waveguide.

7.3 Results & Discussion

The increase in effective index with increase in the UV dosage is depicted in Fig. 7.4.

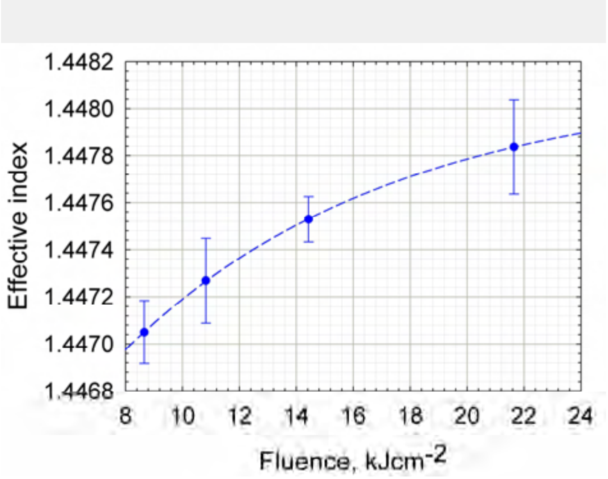

Figure 7.4 Effective indexes versus UV writing fluence. Sample used: DN423/1.

The trend shown in Fig. 7.4 is as expected, and a similar behaviour was described by Emmerson [4]. Effective index, as discussed in Chapter 5, is a function of both core and cladding refractive index (see equations [5.37] and [5.41]). In the absence of meaningful levels of index change in the cladding layer[1] upon UV irradiation, then we would expect that increase in effective index directly implies an increase in the core index. As such, a fluence test allows measurements of Δn for a given fluence level, with the increase in index being reflected by the shift in peak Bragg wavelength, λ_B. Intuitively, the graph is expected to level off at some point, where increase in UV writing fluence would no longer have any effect in terms of index increase. This occurs when photosensitivity is completely saturated. Noting that photosensitivity is intimately related to the processing history of the substrates, it is somewhat pointless to make any form of comparisons with other reported work with regards to this saturation point. Suffice to conclude at this point, that for the fluence levels that we normally use ($F < 30\text{kJcm}^{-2}$), the photosensitivity is not saturated.

In addition to the above, when we consider typical operating UV beam powers in the regions of 50mW, to write structures with $F = 30\text{kJcm}^{-2}$ for example, we would require a translation speed of ~2.8mm/minute which is prohibitively slow when hydrogen out-diffusion effects are factored into the process.

Using the data provided in Table 7.1, we were able to calculate the absolute index increase, Δn_{abs} with fluence for the particular sample, providing us with useful information for the design of more complex structures, as well as for simulation purposes. Table 7.2 summarises the calculated absolute increase in refractive index of the UV-written structures for a corresponding fluence.

Table 7.2 Absolute refractive index increase for a given fluence level.

Fluence (kJcm^{-2})	**Effective index**	**Absolute index increase***
8.6	1.4471	3.6×10^{-3}
10.8	1.4473	3.9×10^{-3}
14.4	1.4475	4.3×10^{-3}
21.6	1.4478	4.7×10^{-3}

* The non-UV exposed core index of 1.4452 is used. Absolute index increase, $\Delta n_{abs} = n_{UV} - n_{non\text{-}UV}$, where n_{UV} and $n_{non\text{-}UV}$ are the index values for the UV exposed and non-UV exposed structures respectively.

---

[1] We would expect the cladding layer to absorb a small percentage of the UV light despite not containing any germanium. This could be supported by the observation of ~ 400nm fluorescence originating from the cladding layer, although the intensity of this fluorescence is orders of magnitudes less to that emitted by the core.

Using a similar experimental approach, it is possible to quantify the birefringence of the sample. Birefringence is a measure of the difference in the propagation constants of the two orthogonal modes TE and TM, and is defined by $|n_{eff\mathrm{TM}} - n_{eff\mathrm{TE}}|$. This polarisation dependence, in many cases, is detrimental to device performance. The effect manifests itself, for example, in the form of polarisation dependent loss, broadening of the grating response, and polarisation dependent coupling. A number of factors contribute to birefringence, not least the difference in coefficient of thermal expansion (CTE)[2] in the case of silica-on-silicon. This CTE mismatch results in a stress gradient within the layers (along the vertical direction), causing compression which subsequently leads to a different refractive index being 'seen' by polarised light. Another contributing feature is the asymmetry of the waveguide itself, inevitably causing $n_{eff\mathrm{TE}}$ and $\mathrm{n}_{eff\mathrm{TM}}$ to display different values. There are a number of approaches reported in the literature to minimise birefringence, including tailoring the UV beam spot size [5], novel waveguide dimensions [6], material processing [7] and the addition of stress relief structures such as milled grooves [8]. Our sample exhibited a mean birefringence of 2×10^{-4}, and this can be attributed to both waveguide asymmetry[3], and inter-layer stress.

7.4 Proximity Effect

The advantages of direct UV writing in producing X-couplers have been highlighted in Chapter 6. In our work, the raised waist index was achieved by multi-exposing a region on the sample with UV light. I have also shown in the previous chapter that to obtain symmetric power splitting behaviour (50% power splitting) for a given X-coupler crossing angle, the ability to tailor the UV writing dosage so as to compensate for the photosensitivity level changes resulting from the multi-exposure is essential. A detailed knowledge of how the initial exposure affects the photosensitivity levels of adjacent regions on the substrate (up to 10's of microns away), known as the 'proximity effect', is also useful, particularly in fabricating cascaded splitter devices, where multiple crossing waveguides are required. This effect has been reported before, [9] but to our knowledge, no quantitative characterisation of its behaviour has been performed, particularly in silica-on-silicon. This is not surprising given the sample specific behaviour of photosensitivity.

---

[2] CTE for silica = 0.55×10^{-6}/°C whereas CTE for silicon ~ 2.5×10^{-6}/°C.

[3] See Chapter 10 regarding recent work in accurate determination of waveguide dimensions via a combination of confocal microscopy and micro-luminescence characterisation.

For the experiment to quantify the proximity effect, sets of three 1mm long Bragg gratings with three different periods (Λ_1=529.3, Λ_2=534.5, Λ_3=539.6nm) were defined at a fixed spacing from a set of earlier defined straight 1mm length regions, as shown in Fig. 7.5. It was found that by using three gratings, the initial issues resulting from uncertainties due to coupling between the two closely spaced adjacent channels could be overcome. Since this coupling effect is wavelength dependent, the use of multiple gratings with different λ_B helps simplify the interpretation of results.

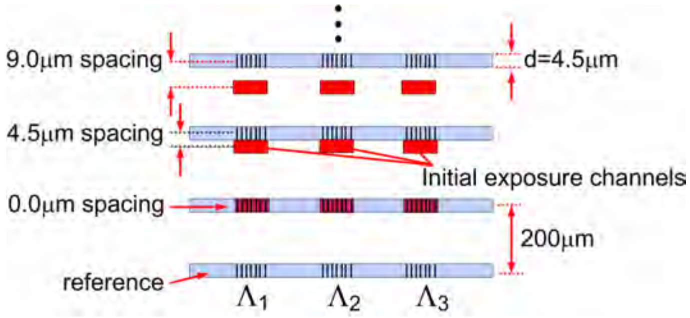

Figure 7.5 Experimental layout of UV-written Bragg gratings and previously defined channel waveguides for proximity effect characterisation (d: waveguide width).

Reflection spectra of the gratings were then recorded (Fig. 7.6) using the set up shown in Fig. 7.3. This then allows the calculation of average effective index of the waveguide, as depicted in Fig. 7.7. Using different fluence levels allows the determination of the spatial extent of this behaviour in relation to UV dosage. The horizontal extent (width) of this effect is expected to be proportional to the applied fluence.

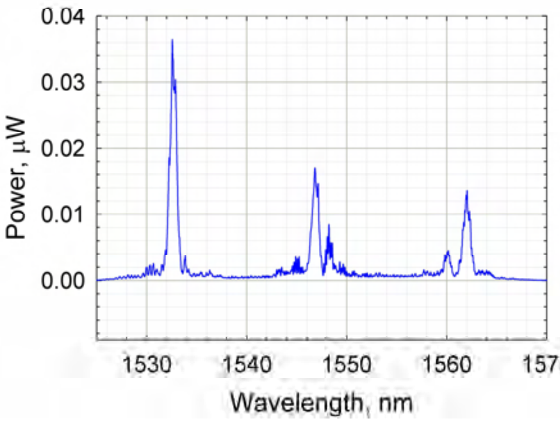

Figure 7.6 Example of the gratings' reflection spectra used for the proximity effect experiment.

It can be seen from Fig. 7.7 that an increase in index is obtained in regions up to 9µm away, highlighting the proximity effect, and with a maximum increase obtained when the same region is multi-exposed (0µm spacing). Effective index increases as large as 8.3x10^{-4} (with respect to the reference gratings) were recorded.

We believe that the behaviour exhibited is due to non-localised heating effects, resulting in redistribution or creation of additional oxygen deficient defects, causing an increase in photosensitivity. The mechanisms taking place that resulted in such an increase in photosensitivity is probably similar to the thermal locking approach (discussed in Chapter 4 and work by Emmerson [10]), and pre-exposing germano-silicate fibres to CO_2 laser irradiation prior to grating writing, as described by Brambilla and colleagues [11].

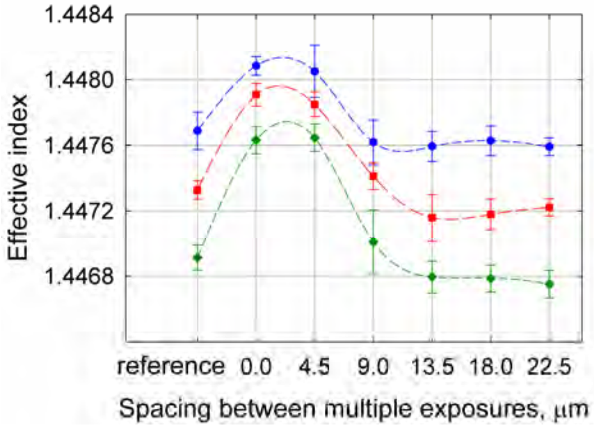

Figure 7.7 Effective indexes at various spacing and fluence values.

(●: Fluence, F = 22kJcm^{-2}, 🟥 : F = 14kJcm^{-2}, ◆ : F = 9kJcm^{-2})

These results reinforce the claims, made earlier, regarding the raised index waist of UV-written X-couplers. The normalised profile height, h, which is the measure of index increase in the waist with respect to the individual X-coupler channels, as described by equation [5.49], can be calculated by referring to Tables 7.1 and 7.2 for the refractive index values of the cladding layers, n_2 and the individual UV-written channels, n_1 respectively, and obtaining the waist index, n_w from the effective index values provided by the 0µm spacing cases depicted in Fig. 7.7.

As the fluence of the first exposure increases, the remaining photosensitivity level of the exposed region is expected to decrease. On the other hand, a lower first exposure fluence implies that the remaining photosensitivity is still enough to generate a significant index increase during subsequent exposures. This is reflected in Fig. 7.8 where h is inversely proportional to fluence. It is also worth noting that I have used *h* = 1.5 for the BPM simulations presented in Chapter 6 and, in light of the results presented here, the choice was justifiable i.e. the value is within the range of magnitudes presented here, bearing in mind that the samples used for the X-coupler experiments were not fabricated by CIP and therefore, are expected to show a slight difference in such behaviour.

In addition to this, the somewhat slow and exponential-like decrease in proximity effect as we move away from the 0μm case shown in Fig. 7.7 supports the assumption that was made for the BPM simulations regarding the index tapering of the individual X-coupler channels along the direction of propagation approaching the waist segment.

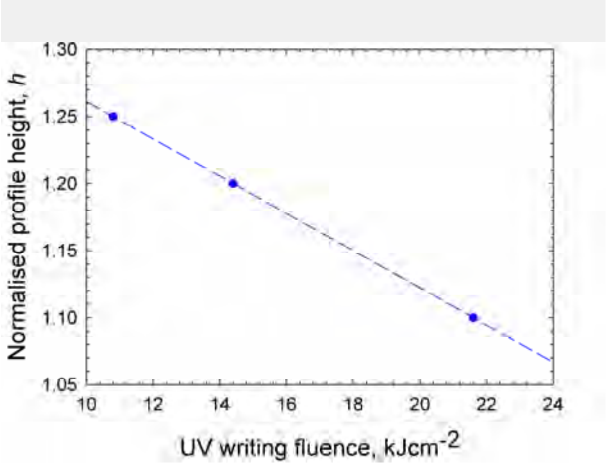

Figure 7.8 Normalised profile height, *h* versus UV writing fluence.

7.5 Summary

Apart from their important role in novel devices, it has been demonstrated in this chapter that Bragg gratings can be useful interrogation tools to facilitate determination of important substrate parameters, such as photosensitivity and proximity effects. Measurements in support of assumptions made earlier regarding the X-coupler work were also presented here.

The fluence test is a necessary experiment in determining the photosensitivity of our sample, providing information relating to the ‘linear’ operation regime with UV dosage used. Such data is vital in UV multi-exposure experiments such as the work on X-couplers. We have also experimentally quantified the proximity effect by demonstrating that photosensitivity increase is evident with initial exposures up to two waveguide widths away.

Another use of Bragg gratings is in the assessment of core layer uniformity (flatness). This again derives from their ability to allow assessment of changes in the effective index of the structure to be performed, which is in turn linked to waveguide dimensions. We have conducted experiments to prove this last point. However, these results will be presented in Chapter 9 as they were carried out on our novel flat fibre technology.

In the following chapter, I will describe a device that is based on Bragg grating sensors. The work involves the use of a liquid crystal overlay to tune the peak Bragg wavelength.

References:

[1] R. Kashyap, *Fiber Bragg gratings*: Academic Press, USA, 1999.

[2] G. D. Emmerson, "Novel direct UV-written devices," PhD thesis, University of Southampton, 2003.

[3] T. Erdogan, "Fiber grating spectra," *Journal of Lightwave Technology*, vol. 15, pp. 1277-1294, 1997.

[4] G. D. Emmerson, C. B. E. Gawith, S. P. Watts, V. Albanis, R. B. Williams, S. G. McMeekin, J. R. Bonar, R. I. Laming, and P. G. R. Smith, "Photosensitivity locking technique applied to UV-written planar Bragg gratings," *Electronics Letters*, vol. 39, pp. 517-518, 2003.

[5] M. Svalgaard, "Direct UV-written integrated optical components," *Optical Fiber Conference* (OFC) Los Angeles, CA, USA, 2004, paper FK2.

[6] M. Hoffmann, P. Kopka, and E. Voges, "Low-loss fiber-matched low-temperature PECVD waveguides with small-core dimensions for optical communication systems," *IEEE Photonics Technology Letters*, vol. 9, pp. 1238-1240, 1997.

[7] A. Kilian, J. Kirchhof, B. Kuhlow, G. Przyrembel, and W. Wischmann, "Birefringence free planar optical waveguide made by flame hydrolysis deposition (FHD) through tailoring of the overcladding," *Journal of Lightwave Technology*, vol. 18, pp. 193-198, 2000.

[8] Y. Nasu, M. Kohtoku, M. Abe, and Y. Hibino, "Birefringence suppression of UV-induced refractive index with grooves in silica-based planar lightwave circuits," *Electronics Letters*, vol. 41, pp. 1118-1119, 2005.

[9] K. Faerch and M. Svalgaard, "Symmetrical waveguide devices fabricated by direct UV writing," *IEEE Photonics Technology Letters*, vol. 14, pp. 173-175, 2002.

[10] G. D. Emmerson, C. B. E. Gawith, S. P. Watts, V. Albanis, R. B. Williams, S. G. McMeekin, J. R. Bonar, R. I. Laming, and P. G. R. Smith, "Photosensitivity locking technique applied to UV-written planar Bragg gratings," *Electronics Letters*, vol. 39, pp. 517-518, 2003.

[11] G. Brambilla, V. Pruneri, L. Reekie, and D. N. Payne, "Enhanced photosensitivity in germanosilicate fibers exposed to CO_2 laser radiation," *Optics Letters*, vol. 24, pp. 1023-1025, 1999.

Chapter 8

Tunable Bragg Gratings via a Liquid Crystal Overlay

In today's telecommunication market, price competition provides a significant motivation for engineers to increase the scalability and span of optical networks, while maintaining channel integrity and, at the same time, keeping operational expenditures to a minimum. One potential route that has gained a lot of interest is to introduce reconfigurable network elements. Consequently, devices on integrated optics platforms such as arrayed waveguide gratings and micro-electro-mechanical (MEMS) based switches continue to be the subject of intense research [1]. In the field of reconfigurable optical add drop multiplexers (ROADMs) for example, a number of frequency/wavelength resonant technologies such as ring resonators, surface relief gratings, and Bragg gratings are utilised, mainly to perform filtering tasks. Castro et al [2] utilised a combination of asymmetric y-branches and anti-symmetric buried etched gratings for their OADM chip, relying on the ability to adiabatically separate even and odd modes via the asymmetric y-branches. Similarly, Riziotis and Zervas [3] proposed a grating assisted 4-port null coupler to perform the same task. However, it has to be pointed out that, in both cases, tunability of the grating is not mentioned.

The most widely used techniques for Bragg wavelength, λ_{B}, tuning are thermal or applied stress to fibre Bragg gratings, and examples of such approaches can be found in references [4-7]. Kumazaki et al [4] reported a 0.055nm/°C λ_B shift rate by heating a liquid paraffin layer that was acting as the cladding layer for a thinned fibre Bragg grating (FBG). The term thinned Bragg grating was adopted to imply that the cladding layer and parts of the core of the fibre were removed (in this particular case via plasma etching). Their thermal tuning approach takes advantage of the large[1] thermo-optic coefficient of the liquid paraffin

---

[1] This is in comparison to silica for example, which has a thermo-optic coefficient, *dn*/*dT* of ~ 10^{-5}/°C (see *Integrated Optical Circuits and Components: Design and Applications* by E.J. Murphy, CRC Press 1999).

(-3.5 x 10^{-4}/°C), permitting higher thermal tuning efficiency. Stress tuning was also reported by the same authors, displaying a 3.4nm shift for every 100V supplied to a piezo-controlled fibre stretcher. The authors argued that using a thinned structure would increase sensitivity towards applied forces. Mavoori et al [7] used temperature-dependent tensile strain onto their FBG by heating materials with opposing thermal expansion coefficients bonded to either end of the fibre. This approach achieved ~4nm shift over a ΔT of 40°C.

Surprisingly, to date, very little has been reported on electrically-tunable Bragg gratings, particularly in planar form, given the potentially superior response time over their more commonly used temperature-tuned counterparts. In her work, Sneh [8] suggested switching speeds of the order of 10’s of μs up to 100ms as opposed to the typically 100’s of milliseconds via temperature tuning. Electrical tuning of gratings is also a non-mechanical approach, allowing simpler device construction and reduced scope for instabilities resulting from the use of multiple material systems. Such electrically tunable devices work on the principle of shifting the Bragg wavelength by modifying the effective refractive index of a waveguide in a multilayer substrate, which is related to the evanescent field sensing concept described by Iadicicco [9] and Chryssis [10]. One potential route to achieve this is by overlaying the grating structure with a liquid crystal. Liquid crystals display refractive index anisotropy due to their molecular structure and orientation that can be manipulated using an electric field. Changes to the liquid crystal index subsequently alter the effective index of the waveguide, leading to Bragg wavelength shift. Using this approach, Sparrow et al [11] have previously described 35GHz electrically tunable planar Bragg gratings in silica-on-silicon at 1560nm using an 80Vpp (peak-to-peak) square wave with 250μm-spaced aluminium electrodes. Theoretical analysis of devices utilising similar concepts for switching and tunability can be found in work by Sirleto [12], and Asquini [13] for example. In [12], Sirleto postulated and modelled an electro-optical switch based on a surface relief grating covered with liquid crystal sandwiched between two electrodes. Application of a voltage would modify the liquid crystal features via the same mechanism described above, leading to changes to the behaviour of light incident onto the grating, resulting in switching and tunability. Fratalocchi [14] reported an experimental demonstration of an integrated, low power, and broadband optical switch by controlling the index of a dual-mode waveguide, thus determining the superposition of the two modes at the waveguide output.

This chapter is a culmination of collaborative work with the members of the liquid crystal group in the School of Physics and Astronomy in the University of Southampton (specifically: Andriy Dyadyusha and Malgosia Kaczmarek). It will describe experimental work in realising electrically tunable first order Bragg gratings via liquid crystal index modification with a maximum tunability of 141 GHz at 1562 nm and 114 GHz at 1561.8nm for transverse magnetic (TM) and transverse electric (TE) polarised input light respectively. Electro-patterned ITO-coated glass was used to provide a local electrode structure, as opposed to the metal deposition previously adopted by Sparrow. The tunability range was achieved with a 170Vpp sinusoidal supply voltage (voltage swing between -85V and +85V with 0 DC offset) at 1 kHz and is limited by the initial grating reflection strength (~17 dB with respect to noise level) and the supply voltage level. Distinct threshold behaviours leading to hysteretic tuning curves were also observed in this work. This chapter starts with a brief description of the properties of liquid crystals.

8.1 Liquid Crystals

There is a vast literature about liquid crystals (LC) and it is not the aim of this chapter to provide a comprehensive description of the technology. Work by Collings and Hird [15], and Sussman [16] provide good introduction points to the subject, and for a more device-oriented treatment, please refer to [17-19] for example. Liquid crystals, as the name implies, are fluidic, but, at the same time, display some level of molecular ordering analogous to crystalline structures. In short, below their transition or clearing temperature, these LCs can be regarded as anisotropic fluids. This molecular ordering is, to some extent, caused by the physical structure of the LC molecules, the most common of which are rod-shaped. Following from this, there is a tendency for these molecules to point along a preferred direction, exhibiting a form of orientational ordering. This preferred direction is called the director and is denoted by unit vector, $\hat{n}$. In addition to the above, some liquid crystal phases also display positional ordering. The simplest LC phase is nematic, where only orientational ordering is exhibited. The smectic A phase in contrast, displays both orientational and positional ordering, giving rise to a layered structure also known as the book-shelf configuration. Fig. 8.1 depicts schematically the nematic phase and director $\hat{n}$, and was the type of LC used for the experiments in this chapter.

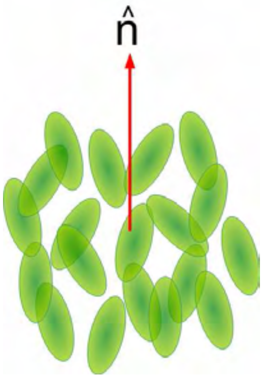

Figure 8.1 Illustration of the molecular order in a nematic liquid crystal.

Intuitively, given the above description, we would expect LCs to be anisotropic in terms of their polarisation along the two main LC axes, which in turn leads to optical anisotropy. Specifically, supposing that the director is pointing in a fixed direction, then the average dipole moment per molecule and thus the polarisation of the LC is different depending on whether the electric field is applied parallel or perpendicular to the director [15]. Another factor worth noting is whether the molecules have positive or negative dielectric anisotropy. Positive dielectric anisotropy molecules tend to reorient with their long axis parallel to applied electric field. Likewise, molecules with a negative anisotropy will align their long axis perpendicular to the applied field. The difference in polarisation is reflected in the ordinary and extraordinary indexes of LCs, denoted by n_o and n_e respectively. n_e in this case represents the situation where the optical field is applied parallel to the director and n_o denotes the opposite case. An alternative notation often used to represent the indexes is $n_{\|}$ (= n_e) and $n_{\perp}$ (= n_o).

Clearly, the director alignment is the key parameter to LC behaviour. Consequently, it is important to establish the alignment state when a device incorporating an LC cell is assembled. Recognising that director alignment is affected by the surface with which the molecules are in contact, we are able to align the LC molecules with their director pointing either perpendicular or parallel to the contact surface. The former is known as homeotropic alignment whereas the latter is called homogeneous or planar alignment. Homeotropic alignment can be achieved by surface treating using surfactant solution (a type of solvent), whilst mechanical rubbing of a surface, creating micro-relief structures, typically results in planar alignment of the LC molecules. These two alignment states are depicted in Fig. 8.2.

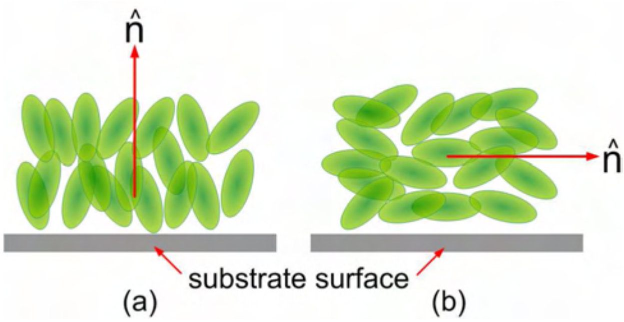

Figure 8.2 Illustration of (a) homeotropic and (b) homogeneous alignment.

For the experiments described in this chapter, we have utilised a nematic BDH 18523 LC developed by Merck. Table 8.1 provides various LC material parameters.

Table 8.1 Nematic LC BDH 18523 specifications.

Phase	Nematic
Dielectric anisotropy	Positive
n_e @ λ = 589nm, T = 20°C	1.5089
n_o @ λ = 589nm, T = 20°C	1.4599
***Clearing temperature**	~ 60°C

* Clearing temperature is the temperature at which the liquid crystal becomes isotropic. The value provided was determined experimentally by Andriy Dyadyusha.

The primary reason for using LC 18523 is because the refractive index values of the LC, particularly n_o, are compatible with that of silica. Most LCs display n_o values exceeding 1.46. As such, for Bragg grating tuning via an evanescent field sensor structure, such values would ‘pull’ the mode away from the waveguide, eventually resulting in loss of guidance. For the operating wavelength of interest (λ = 1550nm), n_o and n_e values for LC 18523 are obtained from work by Pan and colleagues [20], with n_e and n_o of ~1.489 and ~1.445 respectively, as depicted in Fig. 8.3.

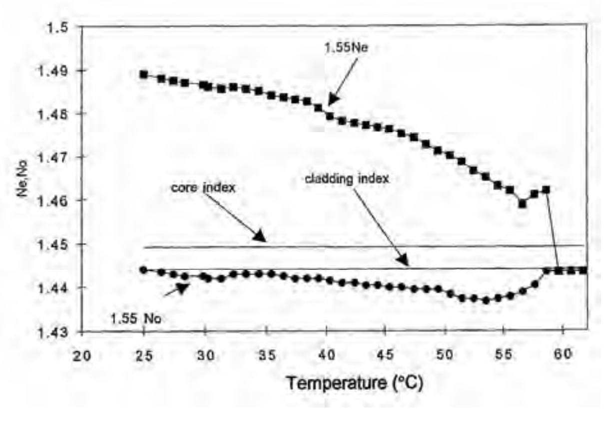

Figure 8.3 Refractive index of the LC18523 with temperature at λ=1550nm (taken from [20]).

8.2 Device Assembly

The grating sensor sample used for this experiment was originally fabricated by Ian Sparrow. We were not able to construct a new sample for my work as the clean room facilities were unavailable, preventing surface etching work.

The sample contains a series of 2 mm long gratings with $\Lambda = 537$nm, UV-written on a hydrogen loaded, end polished, FHD sample measuring ~ 10mm x 15mm. The cladding and core refractive indices were 1.4434 and 1.4505 respectively. A finite section of the 20μm thick overclad layer of the sample covering the grating was removed via hydrofluoric acid wet etching. Surface profiling measurements of this etching technique showed peak to peak surface modulations measuring ~800nm with lateral periodicity of ~18μm [21], which could directly affect the surface alignment of the liquid crystal molecules. For his work, Sparrow has deposited 100nm thick aluminium layers as electrodes, spaced 250μm apart. These metallic layer electrodes were removed prior to my experiments by a repetitive sample cleaning procedure involving immersing the sample in acetone and subjecting the arrangement to an ultrasonic bath treatment, followed by gently scrubbing off the remaining aluminium layers.

The electrodes were prepared by electro-patterning (electrically scribing) through a piece of single sided Indium Tin Oxide (ITO) coated glass. The spacing between the electrodes is estimated to be ~60 μm and the patterned glass was then cut to match the dimensions of the UV-written sample. Homeotropic alignment of the liquid crystal molecules was achieved by applying a thin layer of surfactant (Merck liquicoat ZLI-3334 0.2% solution in ethanol) in the etched area and on the ITO electrodes and both were then baked at 180 ºC for one hour to ensure good surfactant adhesion. The ITO electrodes were then attached to the top of the sample using supporting glass spacers to allow sample movement for aligning the etched waveguide with the electrodes. LC 18523 was then inserted into the etched window under vacuum. The assembled device is schematically shown in Fig. 8.4.

For our chosen waveguide, λ_B was measured to be ~ 1557.9nm prior to application of the LC. Upon insertion of the LC, this peak shifted to 1560nm, resulting in an increase of effective index by 0.002. This is a clear sign that the LC layer index is larger than the original overclad index of 1.4434.

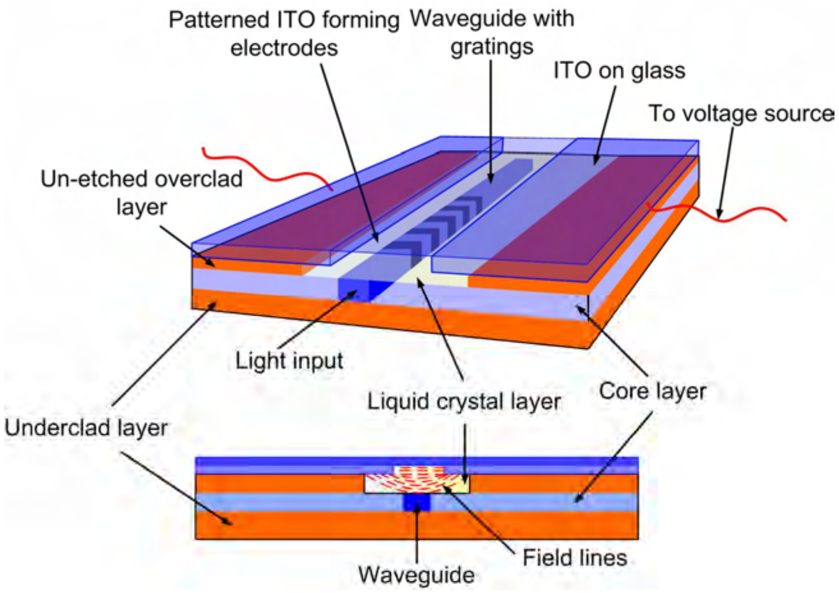

Figure 8.4 A schematic representation of the assembled device showing the liquid crystal overlay in between the electro-patterned ITO electrodes and the waveguide containing Bragg gratings. Overclad, core, and underclad thickness are ~ 20, 5 and 20 µm respectively with a waveguide width of ~ 5 µm.

8.3 Experiment

In order to test the switching characteristics of our LC device, the following procedures were performed. The electrodes were first aligned to the waveguide prior to each experimental run by launching a HeNe (λ = 633nm) laser into the waveguide and observing the scattering from the exposed part of the waveguide. This scattering 'footprint' was easily obtained as the top cladding layer of the sample was etched. The electrodes were then carefully aligned to this scattering 'footprint' as shown in Fig. 8.5.

Given this relatively crude approach in aligning the device, we would expect the generated measurements to vary somewhat for each experimental run. Once optimised overlap was achieved, characterisation of the Bragg shift with voltage was conducted.

The characterisation of the device follows the same procedures as described in Section 7.2, using the optical arrangement shown in Fig. 7.3. Computer-based software (Labview) was used to control the voltage level supplied to the device and to obtain various data including the grating spectrum for each voltage level setting and the centre wavelength shift with respect to the initial (zero voltage) condition. For each voltage setting, the code records spectral data from the OSA scan and stores these in a buffer before proceeding to increase or decrease the voltage value. The codes for the software were written by James Gates. A Gaussian Levenberg-Marquardt (Lev-Mar) curve fitting function, $f(x)_{\text{Lev-Mar}}$ was employed in the control program to determine the peak Bragg wavelength. To facilitate this, the software first converts logarithmic spectra information obtained from the OSA to linear before applying the fitting function given by

$$f(x)_{Lev-Mar} = a + (b \times \exp(\psi)) \qquad [8.1]$$

with

$$\psi = -0.693 \times \left(1 + \left(\frac{x-c}{d}\right)^2\right) \qquad [8.2]$$

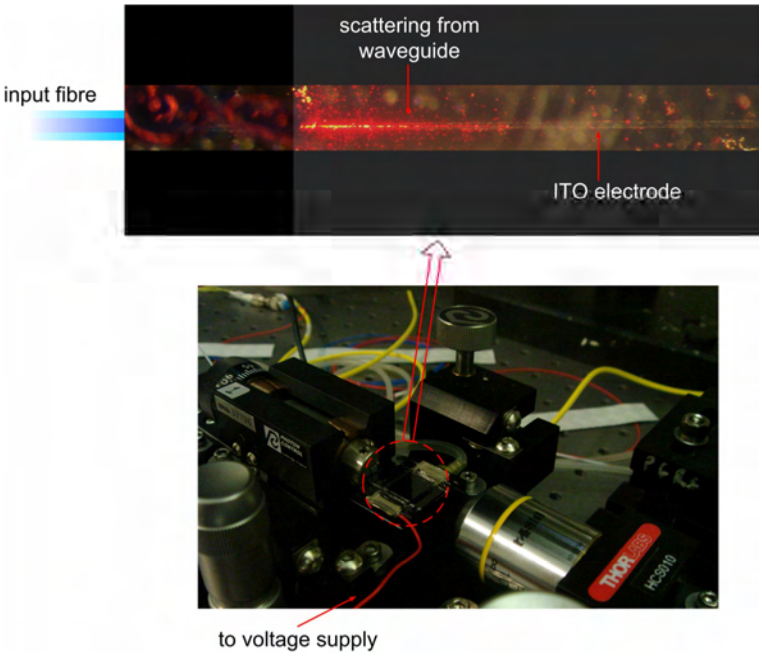

Figure 8.5 Photographs showing the HeNe scattering footprint of an etched segment of the sample containing planar Bragg gratings as viewed from the top of the sample.

Fitting coefficients *a*, *b*, *c* and *d* are defined as follows: *a* is the vertical offset in watts (µW) accounting for the noise floor of the signal from the OSA, *b* is the peak height of the reflection spectrum (µW), *c* represents the peak Bragg wavelength (nm), and *d* is the peak width (nm).

The duration of the process of setting the voltage level and obtaining the spectra from the OSA is dependent on the number of sampling points set for the OSA. We typically use 1001 sampling points, leading to about 3 seconds processing time for each voltage level, resulting in 10-15 minutes being taken for every experimental run.

8.4 Results & Discussion

The Bragg wavelength shift curve of the device for both TM and TE launched input light is shown in Fig. 8.6. For TM input, the curve exhibits 1.15 nm (141 GHz) Bragg wavelength shift over 170Vpp supply voltage and 0.93 nm (114GHz) shift was recorded for the TE case. Both curves display hysteresis between points A and B. Repeat measurements were conducted over a period of several weeks to validate the hysteretic behaviour.

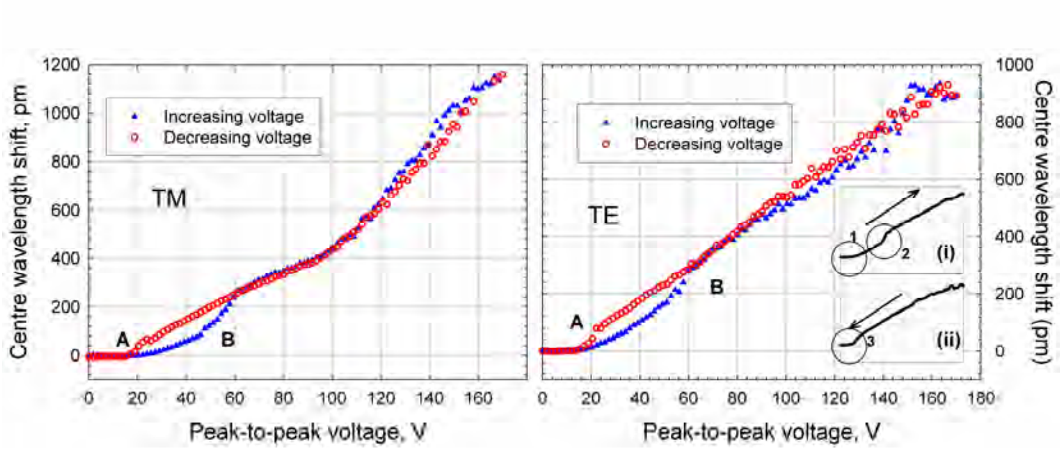

Figure 8.6 Device tuning curves for both TM and TE polarised light showing hysteresis between points A and B. The insets show the same curves for increasing (arrow pointing upwards) and decreasing (arrow pointing downwards) voltages. In inset (i), the circles numbered 1 and 2 shows the two threshold points at ~22V and ~57V respectively. In inset (ii), the low voltage threshold at ~18V is circled and numbered 3.

Inset (i) shows a typical tuning curve with increase in voltage whereas inset (ii) shows the curve with decreasing voltage. It was observed in all measurements that the curves for increasing voltage exhibit two distinct points (circled and labelled 1, 2) where the tuning gradient increases significantly. We discovered that for both TM and TE inputs, the primary threshold is observed at ~18±4Vpp supply voltage, whereas the secondary threshold point seems to appear over a wider margin, around 57±10Vpp. A low voltage threshold point is also observed in the decreasing voltage curve (circled and labelled 3).

The exhibited tuning capability of the device is able to cover at least five 25GHz spaced wavelength division multiplexed (WDM) channels, demonstrating its potential in practical applications. The use of electrical tuning as opposed to thermal would contribute not only in terms of response time, but would also relax the fabrication complexity of the device. A cascaded architecture of such integrated liquid crystal devices operating at different Bragg wavelengths could pave the way towards true colourless add/drop modules for dynamic dense optical networks.

It was initially believed that the low voltage thresholds (points 1 and 3) are the points where the applied electric field is large enough to overcome interactions of liquid crystal molecules with surfaces and elastic forces (in the case of point 1) or the re-appearance of such interactions (point 3). The origin of the secondary threshold is not clear, but our hypothesis was that this was likely to be due to the multi-domain structure of liquid crystals, created in the confined area of the etched window, and their interactions with an applied field, creating disclination. Disclinations are defects in an LC sample with undefined director direction. These defects could take the form of points, lines or sheets [15], with line defects being the most ubiquitous.

The grating spectral measurements at the two threshold points (for the increasing voltage case), as shown in Fig. 8.7, have no noticeable difference in terms of grating strength and shape. Furthermore, the reflection spectrum for both TE and TM do not display any significant differences apart from the peak Bragg wavelength values. The spectra shown further supports the argument that the effect is physical in nature and is related to the liquid crystal overlay behaviour under applied electric field.

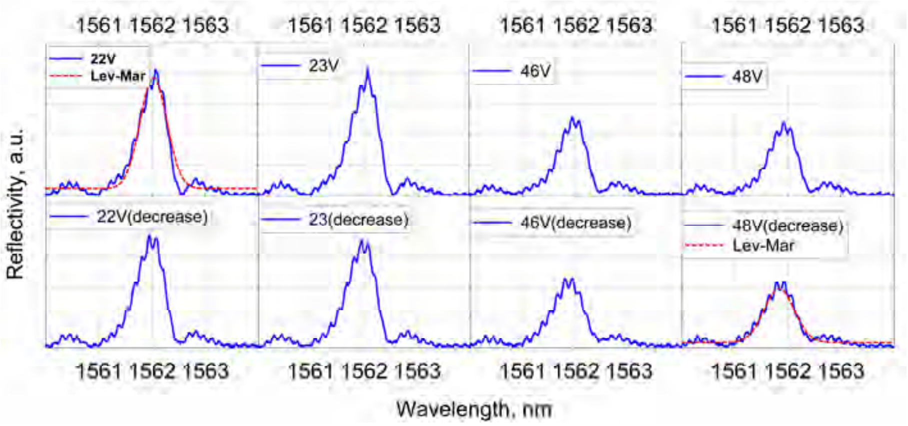

Figure 8.7 Grating reflection spectra at the two threshold points for increasing voltage values. The primary threshold for this case is between 22-23Vpp whereas the secondary threshold point is between 46-48Vpp. No noticeable difference in terms of grating reflection spectral shape and strength is observed at these transitions. Lev-Mar theoretical profiles are also shown on two of the graphs. The ‘periodic’ ripples seen on the spectra are the result of the etalon fringes from the launch and between the facets of the etched window.

In each experiment, the exact threshold points were dependent on the alignment between the waveguide and the ITO electrodes. While a single sample was used throughout the experiments, the need to clean the launch facets between experiments necessitates realignment of the ITO electrodes, causing a variation in the voltages of the two threshold points. Despite these observations, the overall qualitative behaviour of the tuning curves showed excellent repeatability throughout the measurement runs.

The overall tuning range of our devices was limited by the effective refractive index of the host channel waveguide and original (no applied voltage) reflection strength of the incorporated Bragg grating. This effect is due to the refractive index of the liquid crystal, which is larger than that of the waveguide and thus causes loss of modal confinement and a weaker grating response while the device is operated at higher voltages (as shown in Fig. 8.8).

As such, we believe that by implementing stronger waveguides with a narrower Bragg grating reflection, an even larger tuning range will be attainable. In addition, our power supply system is currently limited to 170Vpp before the advent of signal clipping and we also believe that further tuning is achievable with higher voltage levels or by switching to square waves.

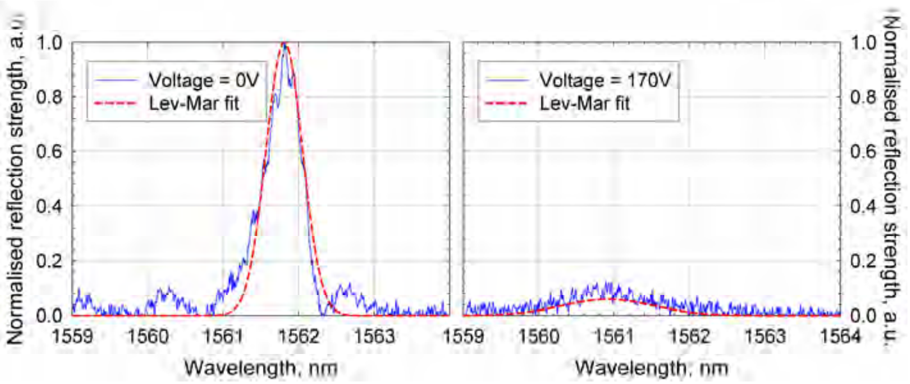

Figure 8.8 Grating spectrum observed in reflection with the fitted Lev-Mar curves shown. The grating reflection strength reduces significantly at high voltages, limiting device tunability.

Having demonstrated successful tuning of the device, we then set out to further investigate the cause of the observed hysteretic behaviour, particularly the threshold point dynamics. Andriy Dyadyusha, in a separate work involving LC 18523 and the ITO electrodes structure similar to that used in this experiment, observed the formation of a disclination line with increase in voltage [21].

To this end, a ‘control’ sample was constructed in conjunction with Benjamin Snow (a member of our group), comprising a microscope slide covered with the same electrode structure as the device in Fig. 8.4 and filled with homeotropically aligned LC 18523. The assembly was then observed through a 90° cross polarised microscope whilst voltage was applied across the electrodes. We observed formation and disappearance of disclinations at specific voltage levels. The formed disclination line becomes progressively narrower with increasing voltage before disappearing completely at elevated voltages. During the decreasing voltage iteration, this defect will not reappear at the voltage level at which it earlier disappeared. Instead, it reappears at a lower voltage, typically < 30Vpp.

These correlations between the voltage levels and disclination dynamics reflect the hysteretic behaviour shown earlier by the tuning curves (Fig. 8.6). The exact threshold points or voltage levels are dependent on the assembled structure and the existence of contaminants along the waveguide/electrode axis, which will form nucleation points from which disclination lines originate. Examples of disclination dynamics are depicted in Fig. 8.9.

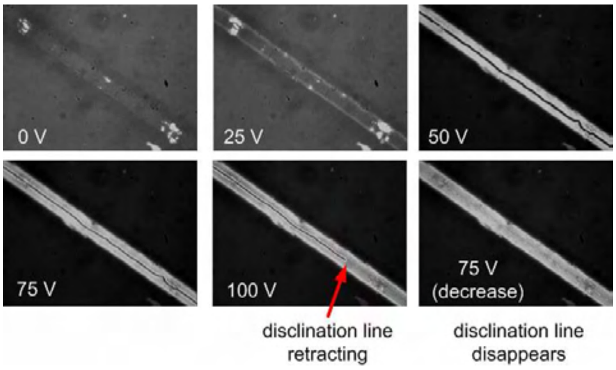

Figure 8.9 Disclination line dynamics with applied voltage seen via 90° cross polarisers (data was taken from experiments by Benjamin Snow).

For the case depicted in Fig. 8.9, the disclination line becomes progressively narrower with increase in voltage. When the supply voltage is ~100Vpp, this disclination line begins to disappear. Reducing the voltage at this point will not recreate the defect. In fact, it is not until V ~20Vpp that the disclination reappears.

8.5 Anomalous Polarisation Behaviour

Following from the above observations, we deduced that the threshold points in the tuning curves are related to disclination line dynamics. However, one important issue still remains. Unexpectedly, both TE and TM show reduced effective index for higher voltages (i.e. shift to lower wavelengths). This cannot be explained by simple geometric arguments. Our initial expectation was that the effective index for TE (n_{effTE}) and TM (n_{effTM}) would be the inverse of each other i.e. if n_{effTE} decreases then n_{effTM} should increase. Such a view is summarised graphically in Fig. 8.10. As can be seen, at 0V, we expect TM polarised light to 'see' the LC's n_e whereas TE polarised light 'sees' n_o. Increasing the voltage will rotate the director and eventually, at elevated voltages, the reverse takes place, as depicted. As such, for TM polarised light, λ_B should shift towards lower wavelengths (reflecting the decrease of LC layer index from n_e to n_o) and vice versa for TE.

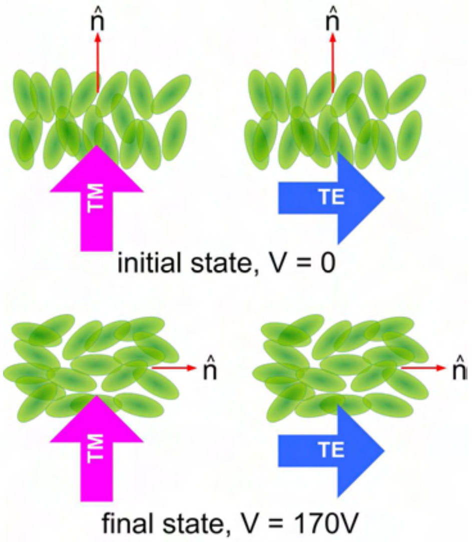

Figure 8.10 Schematic depiction of expected LC alignment at initial and final voltage states, showing the anticipated refractive index 'seen' by TM and TE polarised light.

Given the above picture, we would expect that for TE polarised input, λ_B should shift towards longer wavelengths. A quick transmission study was conducted to see if polarization rotation takes place as light propagates through the LC covered segment of the waveguide. Negligible rotation, in the order of 1° or less polarisation rotation was measured for both polarisations. The transmitted light captured by IR camera for TE input during the increasing voltage sequence is shown in Fig. 8.11. It could be seen that the mode becomes somewhat progressively weaker as voltage increases, supporting the argument presented earlier. This observation however is not conclusive due to the level of saturation of the IR camera, and the changing levels of glitter emitted from the scattering into the LC layer. Secondly, for TM input, there was no observable change in transmission.

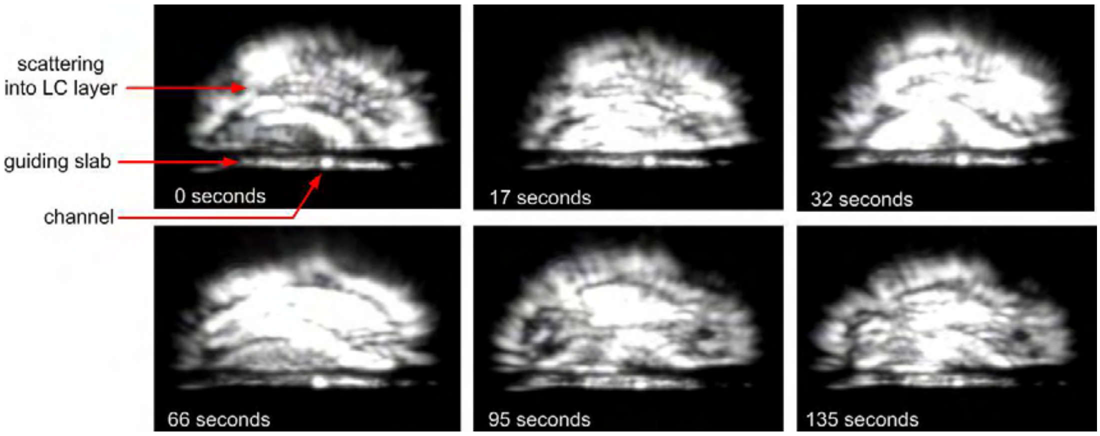

Figure 8.11 Transmission images from the output facet of the LC device at different instances during the increasing voltage sequence with TE polarised input light.

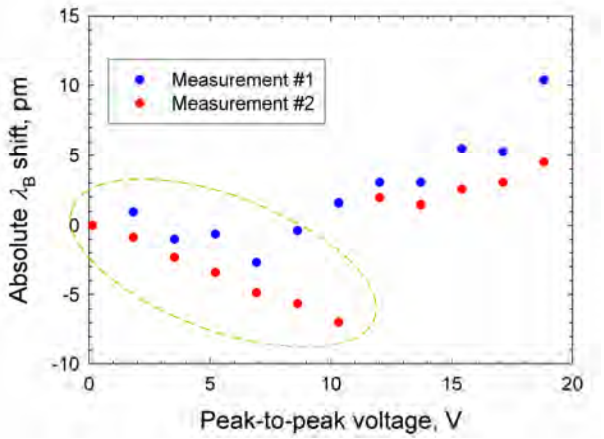

Figure 8.12 λ_B shift for TE polarised input at low voltages. The green elliptical curve indicates the segment where the Bragg shift is as expected, as discussed earlier. Measurements #1 and #2 were performed with over a month separating the two, and those performed in between this period also showed the same behaviour, highlighting the repeatability of the phenomena.

A closer look at the TE tuning curve with very low voltages reveals that for voltages < 11V or so, λ_B does shift to higher wavelengths, and this behaviour is repeatable, as shown by the two measurements in Fig. 8.12. This could possibly be a clue to solving this issue. At the time of writing of this thesis, simulation of the electric field distribution within the LC cell involving colleagues from the Mathematics department has been planned to explain the observed anomaly.

8.6 Effect of Supply Voltage Waveform

The effect of the supply voltage waveform on the tuning curve is depicted in Fig. 8.13. For the sake of clarity, I have only included the tuning curve for the increasing voltage sequence under TE polarised light. It could clearly be seen that using a square wave would result in a steeper tuning curve running up to maximum tunability. The maximum tuning range however, is similar to that shown by the sinusoidal waveform case.

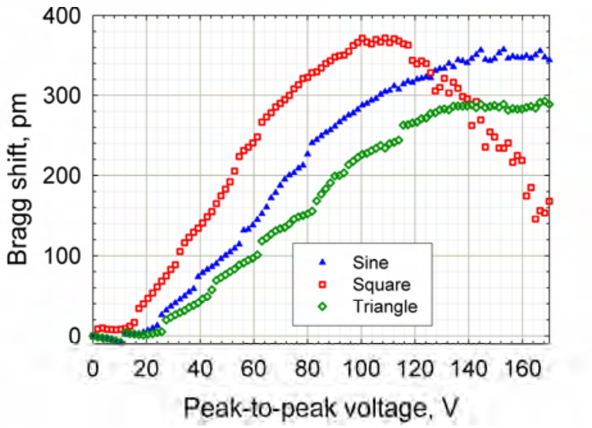

Figure 8.13 TE tuning curve with various supply voltage waveform.

The above result is expected since for a given voltage setting and duration, a square waveform would inherently exhibit higher average power compared to either the sinusoidal or saw-tooth waveforms. This would lead to higher efficiency in terms of LC director orientation as this effect is proportional to the square of the applied field. The apparent fall off of the square waveform case is due to the difficulty in fitting the grating spectra as the reflection peak becomes broader and very weak.

8.7 Effect of Power Supply Frequency

The effect of supply frequency on the tunability of the device is shown in Fig. 8.14. The square waveform was used for this experiment. Again, only the increasing voltage tuning curve is included for clarity.

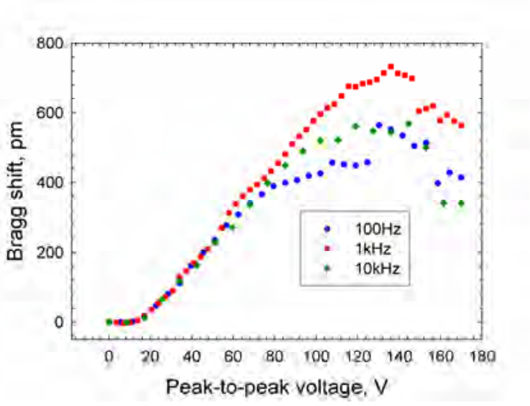

Figure 8.14 A graph showing the effect of supply voltage frequency on tuning range.

Throughout these experiments, AC voltage was used, in order to prevent charge build up in the LC that would eventually lead to reduction in sensitivity to applied field and could potentially damage the assembled cell. The optimal operational frequency in this case is closely linked to the capacitive and resistive characteristics of the LC cell. As can be seen from the graph, at supply voltages below 60Vpp, the tuning curve has no frequency dependence (for the three frequency settings). However, as voltage is increased, we could deduce that using a supply with a frequency of 1 kHz would produce the largest tuning compared to the other two cases.

8.8 Electrode Offset

A further short experiment was performed in order to determine the importance of electrode alignment with respect to the Bragg grating and, to assess whether the tuning range recorded resulted from heating effects. In both optimised and un-optimised cases, the HeNe scattering footprint alignment method, as described in Section 8.3, was utilised. The optimised case is as indicated in Fig. 8.5 whereas the non-optimised case is shown in Fig. 8.15 below where the HeNe scattering emanating from the waveguide is clearly shown to be offset to one side of the electrode.

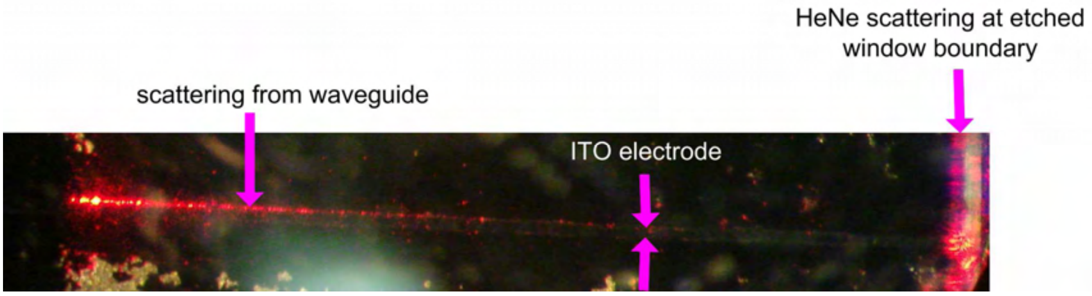

Figure 8.15 HeNe scattering from the waveguide showing non-optimised electrode position (offset).

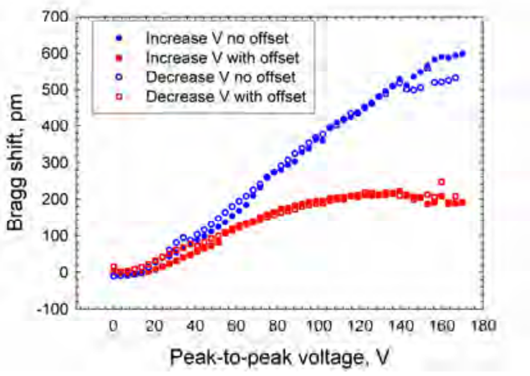

Figure 8.16 Graph showing the effect of electrode position with respect to waveguide on the tunability of the device.

A comparison between the tuning range displayed by the optimised and non-optimised electrode positioning is shown in Fig. 8.16. As expected, a lower tuning range was achieved if the electrodes were not placed optimally relative to the waveguide position. About 63% reduction in tuning is displayed with the waveguide placed along one edge of the electrodes, caused by the limited LC reorientation resulting from the weaker field penetration at these electrode boundaries. The result also indicates that thermal effects are negligible because if the opposite is true, then the tuning range should be similar to the case of optimised electrode positioning. This is clear, because, should heating be the case, the LC would possess similar temperature throughout the confines of the cell, and as such, this would result in similar tuning amplitude over the voltage supply range.

In order to confirm that the tuning behaviour is caused by the electric field generated across the electrodes and therefore is not a thermal effect, a separate experiment involving thermal diffusion across silica layers and the corresponding λ_B shift was conducted.

8.9 Thermal Effects

The premise for this experiment is simple. If increasing the supply voltage resulted in the heating of the LC, then the heat generated would diffuse across the substrate silica layers with which the LC layer is in contact. By using a sample that contains Bragg gratings, this heat diffusion would translate into a shift in λ_B. As silica is heated, it will expand, causing a change in the Bragg grating period, Λ_B, causing the abovementioned Bragg wavelength shift. This shift is between 8-12 pm per degree C, depending on the sample. We had to rely on thermal diffusion for this experiment because we were still unable to perform any wet etching tasks, preventing us from etching a sensor window onto the sample.

The sample previously used for the proximity effect experiment (discussed in Chapter 7) was utilised for this study, and therefore contains three gratings per channel. The ITO electrode was constructed according to the previously discussed method and was attached onto the sample overclad layer via plastic spacers measuring 10μm thick. Once the assembly was completed, LC 18523 was applied into the space between the sample surface and the ITO electrodes.

To assess the overall temperature stability and dynamics, the assembly was then placed onto a metal block which had a hole drilled into one of its sides to fit in a thermocouple. Another thermocouple was placed on top of the sample. This facilitated the measurement of the temperature gradient (if any) between the heating element (metal block) and the sample. The metal block was in turn, placed on a ceramic Peltier mount which was connected to a temperature controller. Measurements were taken at room temperature and at increasing temperatures, and the grating spectra and λ_B shift were recorded for each temperature setting. The arrangement's thermal stability at room temperature over one hour and the thermal dynamics of the assembly is depicted in Fig. 8.17.

As can be seen from Fig. 8.17(a), the set up showed excellent stability with only ~5pm wavelength shift over one hour duration of the experiment. Upon application of heat, λ_B displayed the same order of magnitude of linear shift as predicted earlier, depicted by Fig. 8.17(b).

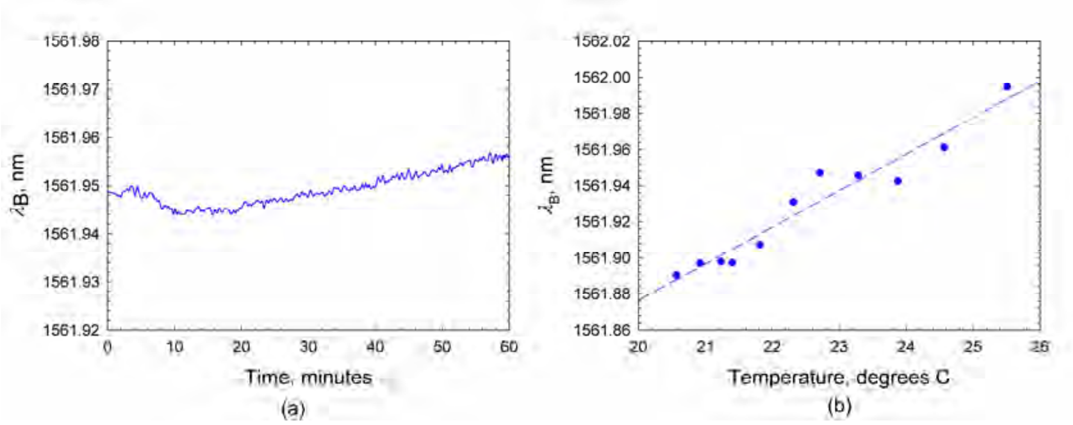

Figure 8.17 Graphs showing λ_B as a function of temperature for: (a) experimental set up under room temperature conditions, (b) thermal behaviour of the assembly (straight curve with broken line is the linear fit).

We next applied 150Vpp voltage across the electrodes with the whole assembly kept stable at room temperature. The voltage was applied over a finite period before being switched off and this procedure was repeated over ~ 1¾ hour duration. Fig. 8.18 shows λ_B

for the three gratings, indicating that little or no heat was diffused across the ~ 18.5μm overclad layer, with maximum shift of not more than 10pm over the entire experiment. From this final result, we could conclude that the tuning effect was not thermally driven and was in fact, due to the electrically induced reorientation of the LC molecules within the overlay instead.

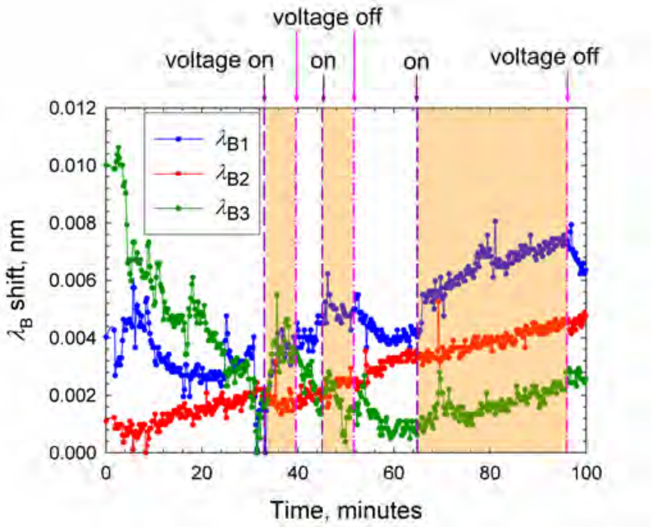

Figure 8.18 A graph showing the effect of applying voltage across ITO electrodes at random points and duration along the experimental run, indicating that very little thermal effect is taking place.

8.10 Applications

As mentioned earlier, one of the primary applications of the demonstrated technology is in active network elements. Grating tunability is also useful in determining the lasing wavelength of fibre lasers for example. However, there are still issues to be addressed, particularly in terms of grating strength reduction with increase in supply voltage and the hysteretic behaviour of the tuning curve.

8.11 Summary

In summary, electrical tunability of UV-written Bragg grating covering at least five 25GHz spaced WDM channels have been demonstrated and characterised. A maximum tunability of 141GHz at 1562nm (TM polarised) and 114GHZ at 1561.8nm (TE polarised) was obtained using electro-patterned ITO-coated glass electrodes, with 170Vpp sinusoidal voltage at 1kHz applied across them. The tuning range is currently limited by the modal leakage caused by the LC layer having a higher refractive index value compared to the waveguide containing the Bragg grating. Clearly, use of a more suitable LC layer would circumvent this issue.

We believe that the hysteretic behaviour of the tuning curve is related to the formation and disappearance of disclination defects along the waveguide axis. A subsequent thermal study conducted also proved that heating effects do not play a role in the tuning behaviour of the device.

One issue that needs to be addressed is regarding the similar tuning behaviour displayed by both TE and TM polarised light, both shifting towards shorter wavelengths. Specifically, both TE and TM show reduced effective index for higher voltages (i.e. shifts to shorter wavelengths) and this cannot be explained by simple geometric arguments.

References:

[1] D. T. Neilson, C. R. Doerr, D. M. Marom, R. Ryf, and M. P. Earnshaw, "Wavelength selective switching for optical bandwidth management," *Bell Labs Technical Journal*, vol. 11, pp. 105-128, 2006.

[2] J. M. Castro, D. F. Geraghty, S. Honkanen, C. M. Greiner, D. Iazikov, and T. W. Mossberg, "Optical add-drop multiplexers based on the antisymmetric waveguide Bragg grating," *Applied Optics*, vol. 45, pp. 1236-1243, 2006.

[3] C. Riziotis and M. N. Zervas, "Design considerations in optical add/drop multiplexers based on grating-assisted null couplers," *Journal of Lightwave Technology*, vol. 19, pp. 92-104, 2001.

[4] H. Kumazaki, Y. Yamada, H. Nakamura, S. Inaba, and K. Hane, "Tunable wavelength filter using a Bragg grating fiber thinned by plasma etching," *IEEE Photonics Technology Letters*, vol. 13, pp. 1206-1208, 2001.

[5] M.-C. Oh, H.-J. Lee, M.-H. Lee, J.-H. Ahn, S. G. Han, and H.-G. Kim, "Tunable wavelength filters with Bragg gratings in polymer waveguides," *Applied Physics Letters*, vol. 73, pp. 2543-2545, 1998.

[6] J. L. Cruz, A. Diez, M. V. Andres, A. Segura, B. Ortega, and L. Dong, "Fibre Bragg gratings tuned and chirped using magnetic fields," *Electronics Letters*, vol. 33, pp. 235-236, 1997.

[7] H. Mavoori, S. Jin, R. P. Espindola, and T. A. Strasser, "Enhanced thermal and magnetic actuations for broad-range tuning of fiber Bragg grating-based reconfigurable add-drop devices," *Optics Letters*, vol. 24, pp. 714-716, 1999.

[8] A. Sneh, K. M. Johnson, and J.-Y. Liu, "High-speed wavelength tunable liquid crystal filter," *IEEE Photonics Technology Letters*, vol. 7, pp. 379-381, 1995.

[9] A. Iadicicco, A. Cusano, S. Campopiano, A. Cutolo, and M. Giordano, "Thinned fiber Bragg gratings as refractive index sensors," *IEEE Sensors Journal*, vol. 5, pp. 1288-1295, 2005.

[10] A. N. Chryssis, S. S. Saini, S. M. Lee, H. Yi, W. E. Bentley, and M. Dagenais, "Detecting hybridization of DNA by highly sensitive evanescent field etched core fiber Bragg grating sensors," *IEEE Journal on Selected Topics in Quantum Electronics*, vol. 11, pp. 864-872, 2005.

[11] I. J. G. Sparrow, G. D. Emmerson, P. G. R. Smith, M. Kaczmarek, and A. Dyadyusha, "35 GHz tunable planar Bragg grating using nematic liquid crystal overlay," *European Conference on Integrated Optics* (ECIO), Grenoble, France, 2005, paper ThB3-5.

[12] L. Sirleto, G. Coppola, G. Breglio, G. Abbate, G. C. Righini, and J. M. Oton, "Electro-optical switch and continuously tunable filter based on a Bragg grating in a planar waveguide with a liquid crystal overlayer," *Optical Engineering*, vol. 41, pp. 2890-2898, 2002.

[13] R. Asquini, A. Fratalocchi, A. D'Alessandro, and G. Assanto, "Electro-optic routing in a nematic liquid-crystal waveguide," *Applied Optics*, vol. 44, pp. 4136-4143, 2005.

[14] A. Fratalocchi, R. Asquini, and G. Assanto, "Integrated electro-optic switch in liquid crystals," *Optics Express*, vol. 13, pp. 32-37, 2005.

[15] P. J. Collings and M. Hird, *Introduction to liquid crystals*: Taylor & Francis, London, 1997.

[16] A. Sussman, "Electrooptic Liquid Crystal Devices: Principles and Applications," *Parts, Hybrids, and Packaging, IEEE Transactions on*, vol. 8, pp. 24-37, 1972.

[17] V. G. Chigrinov, *Liquid crystal devices*: Artech House, USA, 1999.

[18] I.-C. Khoo and s.-T. Wu, *Optics and nonlinear optics of liquid crystals*: World Scientific, Singapore, 1993.

[19] D.-K. Yang and S.-T. Wu, *Fundamentals of liquid crystal devices*: Wiley, USA, 2006.

[20] R.-P. Pan, S.-R. Liou, and C.-K. Lin, "Voltage-controlled optical fiber coupler using a layer of low-refractive-index liquid crystal with positive dielectric anisotropy," *Japanese Journal of Applied Physics, Part 1: Regular Papers & Short Notes & Review Papers*, vol. 34, pp. 6410-6415, 1995.

[21] I. J. G. Sparrow, "Development and applications of UV-written waveguides," PhD thesis, University of Southampton, 2005.

Chapter 9

Flat Fibre Technology

Despite the numerous advantages offered by integrated optical devices, there are many limitations that prevent wider deployment. Among these limitations is the fact that silica-on-silicon samples are mechanically rigid, have upper limit dimension of ~15cm (6 inches silicon substrate), and need to be fibre pigtailed to allow connection to other equipment. Therefore, in the fields of distributed sensing and in data transport for example, fibre based solutions reign supreme.

The limitations of the planar format have encouraged work, here in the ORC, in developing a substrate platform that, among other things, overcomes the mechanical and size limitations of its chip-like predecessor while maintaining the advantages of multi-functionality and dense form factor. To this end, a number of attempts were made, including the development of a planar substrate from a rectangular preform by Harwood [1]. Clearly, one of the motivations for this work is to possess the ability to mass-produce ribbon fibres that are fabricated in a single run, ensuring uniformity and high throughput, instead of combining individual fibres which is the de-facto technology at the moment. Successful demonstration of such a ribbon fibre, for example, would be an attractive proposition to the harnessing issue currently faced by in-flight data transport and Media Oriented Systems Transport (MOST) in cars. An alternative approach for fabricating samples that would allow formation of extended length waveguides beyond the 15cm limit include the work on cylindrical samples by Emmerson [2].

In this chapter, initial results from the development of what we term the 'flat fibre' are presented. The flat fibre is a joint effort also involving the Silica Fibre Fabrication group. The bulk of the fabrication efforts were carried out by Andrew Webb, with supervision from Jayanta Sahu. Flat fibre substrates were created by collapsing an unsealed optical fibre preform fabricated via modified chemical vapour deposition (MCVD) process, into a rectangular/planar shape by applying a vacuum during the fibre drawing process. This rectangular shape is preserved as the preform is drawn into extended lengths of high quality planar substrate.

Having successfully demonstrated the fabrication of the substrate, the next step was to incorporate waveguide structures within the photosensitive core. For the time being, given the dimensions and unique features of the flat fibre (this will be elaborated later), we believe that direct UV writing is the most suitable technique for waveguide definition.

Finally, it is worth pointing out that due to sample availability limitation, it was decided that proof of principle work should take precedence over a more structured study geared towards optimising the various UV writing parameters. The latter option would inevitably require a steady supply of flat fibre samples. As such, the work presented in this chapter utilised typical parameters for UV writing onto silica-on-silicon samples instead and, needless to say, some of the results obtained reflect on this fact.

9.1 MCVD Process

In the MCVD process, reagent gases are passed down a rotating tube that is heated by an external burner that traverses back and forth [3]. The chemical reaction which takes place involves reagent oxidation and formation of soot, similar to the one discussed in Chapter 3.

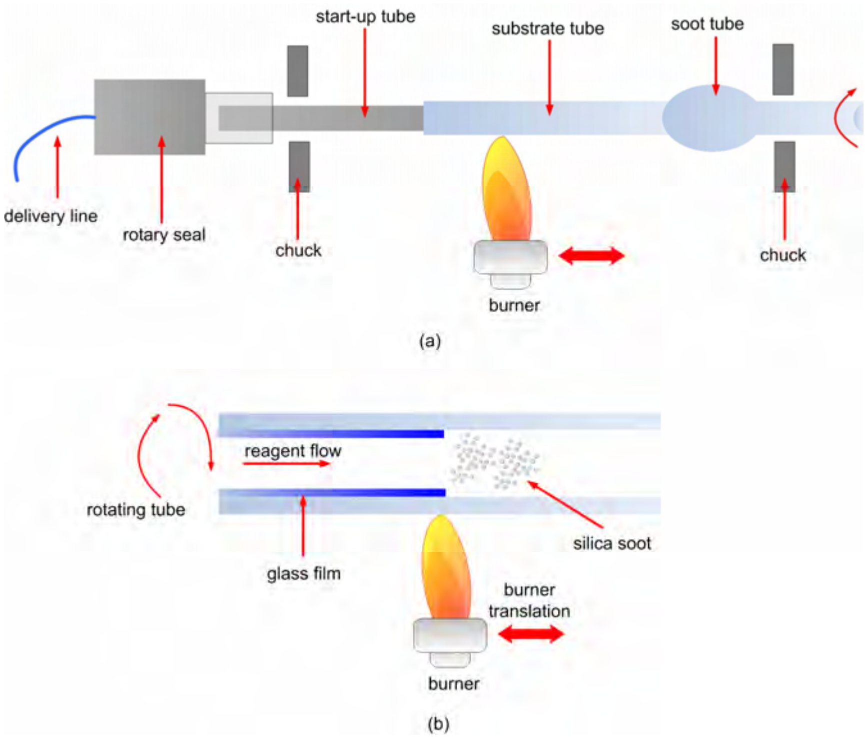

Figure 9.1 Schematic representation of the preform fabrication stage of MCVD, (a) the overall set up, (b) closer look at the soot formation and consolidation into glassy layer.

The temperature of the flame (usually around 1800 - 2000°C) raises the temperature of the tube, eventually consolidating the soot layers into a dense glassy film. The process is shown schematically in Fig. 9.1.

The substrate tube was then collapsed to form a solid preform by reducing the translation speed of the burner, resulting in ‘softening’ of the glass film and collapsing the tube via surface tension. This preform is then transferred onto a drawing tower where fibre drawing takes place. This is depicted in Fig. 9.2.

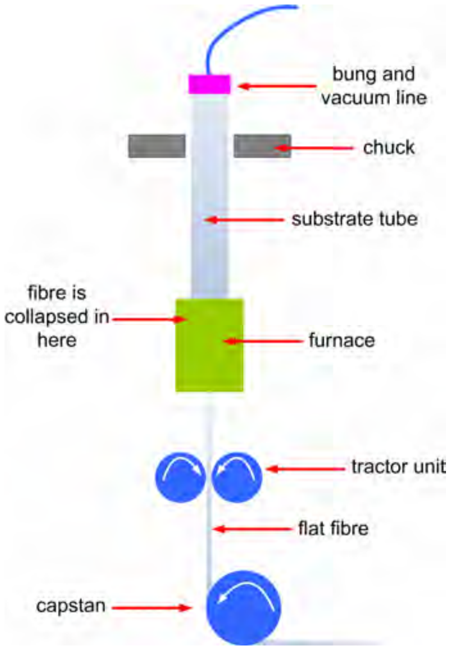

Figure 9.2 Schematic representation of the fibre drawing stage of MCVD. The collapsing of the circular preform into a planar substrate takes place in the furnace, as shown.

It is worth mentioning that an added advantage of fabricating planar substrates via MCVD is the ability to incorporate higher concentration of dopants compared to FHD, and the processes involved in rare-earth doping via MCVD is relatively simpler than FHD.

9.2 Making the Flat Fibre

For the flat-fibre fabrication, core and cladding compositions are deposited inside a high-quality 20mm outside diameter SUPRASIL-F300 tube under usual MCVD conditions. Early samples feature standard silica cladding layers and a germanosilicate core with 10mole% of GeO_2 to provide photosensitivity and a core refractive index of ~1.46, the absolute concentration of which is determined by measuring the numerical aperture of a conventional preform fabricated using the same reagent gas flows.

As mentioned earlier, in a standard preform formation, the substrate tube would be collapsed into a solid rod following the core deposition. However, in order to create flat fibre geometry, this collapse process is skipped. Following deposition the substrate tube is removed from the lathe and positioned in a conventional fibre drawing tower. The tube is then drawn to a circular capillary at furnace temperatures ~ 2000°C. Once the drawing has stabilised, a vacuum of ~15mbar below atmospheric[1] is applied to the top of the substrate tube, collapsing the substrate into a planar format. This is the novel step taken by Andrew Webb that led to the discovery of the successful demonstration of the flat fibre substrate. Vacuum and fibre drawing parameters are then chosen to optimise the geometry of the flat fibre core. The formed flat fibre substrate is depicted in Fig. 9.3.

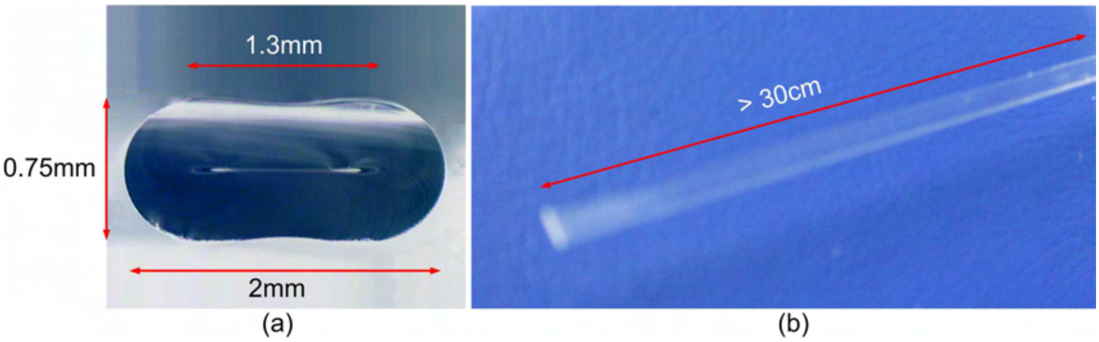

Figure 9.3 Photos showing the (a) cross section; and (b) perspective views of a novel flat fibre sample.

Evidently, the ‘bean-shaped’ profile of the flat fibre, and the thick cladding layer in excess of 350μm meant that defining waveguide structures via photolithography and etching would be non-trivial, involving time consuming multi-step procedures. The top cladding layer would probably have to be polished first to ensure a flat surface for mask aligning purposes, adding to the complexity of the procedure. This led us to believe that direct UV writing is well suited for defining waveguide structures, and the key to the success of the approach relies on the photosensitivity and uniformity of the flat fibre core layer and the ability to accurately focus the UV beam onto the core through the thick cladding layer. Fig. 9.4 demonstrates the first flexible glass planar substrate with lengths extending over a metre.

---

[1] This is equivalent to a pressure of 985mbar.

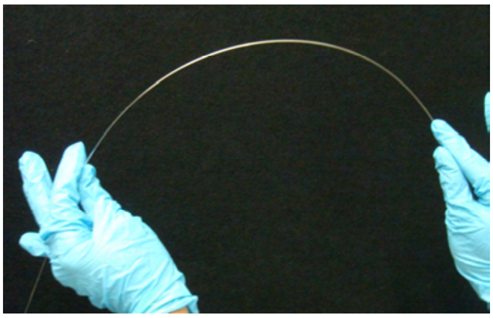

Figure 9.4 Extended lengths of the flexible glass planar substrate.

9.3 Adding Waveguide Structures

As a first proof of principle, simple structures such as straight channels and y-splitters were defined into the flat fibre core layer via single-beam direct UV writing. A series of straight channels with writing speeds varying from 10 to 90mm/minute were UV-written onto a sample measuring 4cm long with laser power of ~56mW.

To demonstrate optical power routing functions, a set of y-splitters was also written. Each y-splitting junction incorporates an input channel waveguide that is bifurcated into two output waveguides via a pair of cosine arcs. Typical output separations of 100µm have been used to demonstrate power routing capability, with the corresponding s-bend radii of a few millimetres.

Each channel waveguide structures was characterised by launching HeNe light into the waveguides using the set up shown in Fig. 6.4. The first demonstration of channels and y-splitters in flat fibre samples is shown in Fig. 9.5.

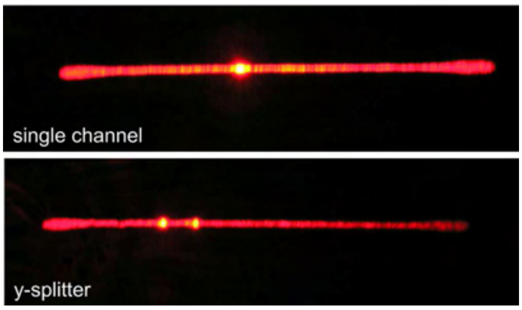

Figure 9.5 Image captures of (a) straight channel waveguide and (b) the two output arms of 100µm y-splitters, both illuminated at λ = 633nm.

No specific optimisation of the writing parameters was performed for these early y-splitters. However, results indicate that the power splitting ratio between arms is near 50:50. These preliminary results demonstrate that larger and more complex waveguide layouts should be achievable in the flat-fibre samples.

An observation to note from this early work was the high level of fluorescence ($\lambda \sim$ 400nm) emitted by the core layer upon irradiation with the UV laser, suggesting a large inherent material photosensitivity, which is an additional advantage of the flat fibre.

9.4 Propagation Loss Measurement - Experiment

Propagation loss in our channel waveguide devices was investigated via a series of cut-back measurements, in which the optical throughput of different lengths of flat fibre are analysed. Here, light is launched into channel waveguides of different lengths and the output power measured both in free space and by collection via butt-coupled fibre. With all other conditions being equal, any change in the optical throughput is assumed to be the result of material-based losses over the change of length. As the most important aspect of this measurement is to minimise any changes to the launch conditions between different samples or waveguide lengths, our approach was to bond an optical fibre pigtail to the end of a flat fibre waveguide a few centimetres long before cleaving and measuring the sample at various lengths. Performing the cut-back measurement in this way minimises any variation of the launch efficiency, although minor changes to the output facet will occur between cleaves.

To ensure added stability and robustness of the pigtail, we decided to mount the whole assembly onto a microscope slide. Attaching the fibre end to the flat fibre was facilitated via the use of low viscosity UV cured glue, which also has a low shrinkage to reduce fibre movement during the curing process. A more viscous and ‘harder’ adhesive was used to mount the pigtailed assembly to the microscope slide. During the pigtailing process, mode launching was continuously observed to check and minimise fibre movement. The pigtailed assembly is shown in Fig. 9.6.

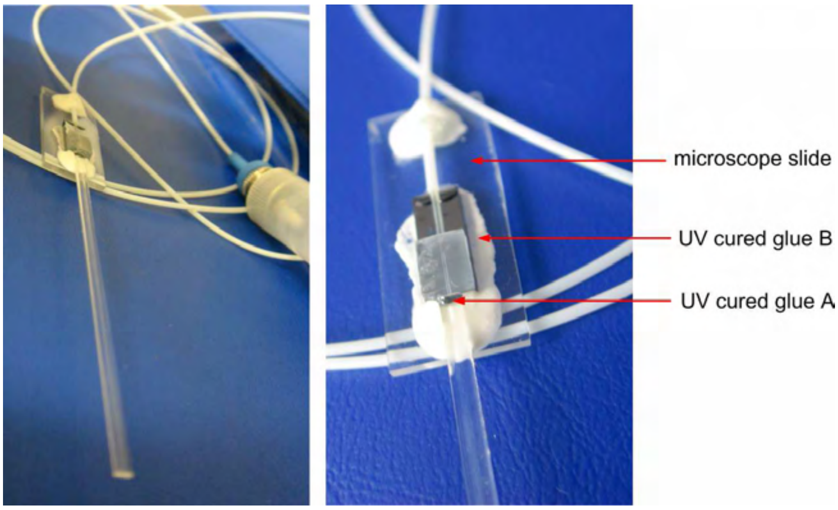

Figure 9.6 Photographs of the pigtailed assembly for propagation loss measurements. (UV cured glue A: Dymax OP-54; UV cured glue B: Dymax OP-60).

The sample was then characterised using the set up shown in Fig. 9.7. Both free space coupling of output power into the power meter and the fibre butt coupled alternative were utilised. For the free space arrangement, optimised measurements were ensured by spatially discriminating the mode from the scattered power emanating from the guiding core slab layer via the pinhole. Once alignment and effective mode clipping is achieved, the power is directed into the power meter detector by use of a mirror.

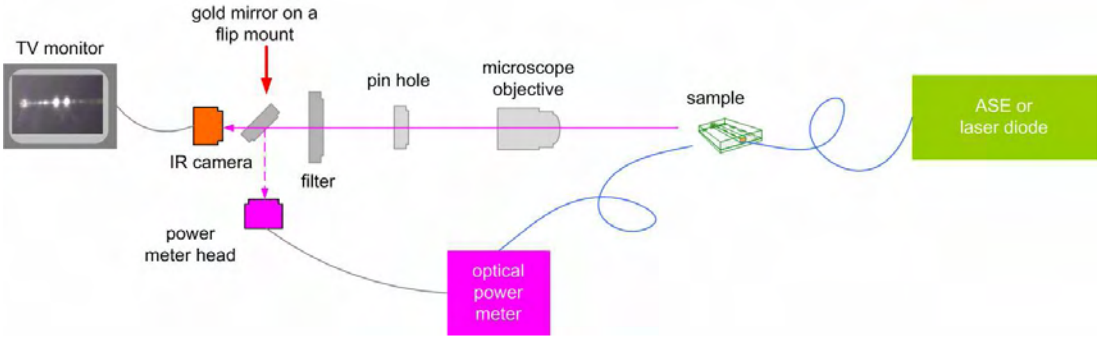

Figure 9.7 Schematic diagram of the optical set up for free space and fibre coupled propagation loss measurement.

9.4.1 Results & Discussion

The detected power using the two methods described above in relation to the flat fibre length is shown in Fig. 9.8. Intuitively, we expected that the power measured via fibre butt coupling would be higher as scattered power from the slab was also included.

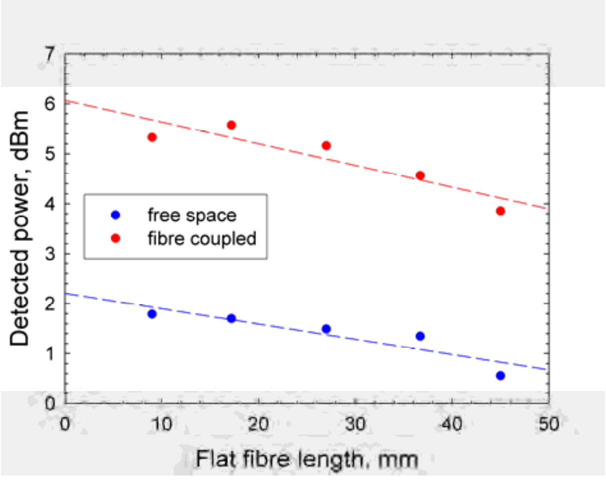

Figure 9.8 Cutback loss measurement results relating detected transmitted light to flat fibre length (curves with broken lines represent the linear fit).

The propagation losses, based on the gradient of the linear curve fits, are 0.3 and 0.4dB/cm for free space and fibre coupled respectively. These values are higher than the often quoted 0.2dB/cm losses in silica-on-silicon. There are a number of possible explanations for this, not least the fact that the UV writing fluence, in this case ~ 14kJcm^{-2}, might not be the optimal setting for this particular sample. Secondly, upon closer inspection of the flat fibre involving scanning electron microscopy (SEM) imaging, we discovered that there exists a clear boundary where the layers ‘meet’ upon collapsing, opening the possibility of light scattering, leading to losses. This is highlighted in Fig. 9.9 with the arrow pointing to the said features. However, this is still a hypothesis and at the time of writing, a further investigation involving determination of optimal fluence levels and the elimination of the boundary are being carried out.

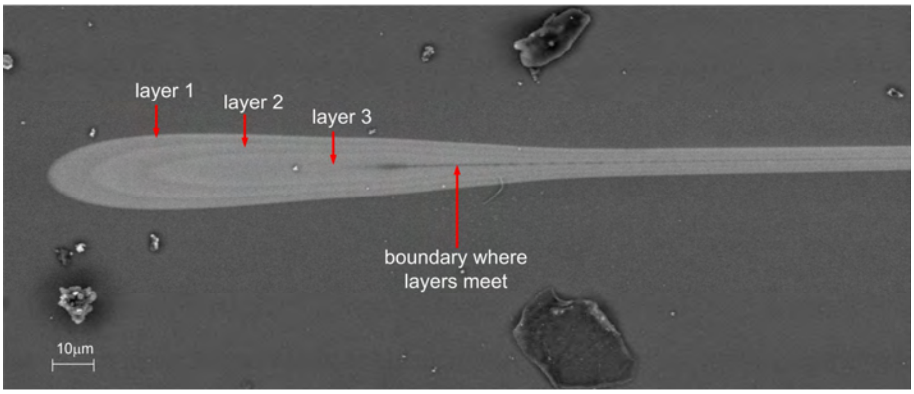

Figure 9.9 SEM image of the core of the flat fibre with the arrow pointing to the boundary where the layers meet. In the case of this sample, three layers of germanium doped layers were deposited during the preform fabrication stage, as clearly shown.

9.5 Substrate Analysis via Bragg Gratings

Further to the above work, physical and optical assessment of layer flatness and waveguide birefringence were also conducted by the use of Bragg gratings. DGW again provides a useful approach to this problem, allowing a series of identical Bragg gratings to be inscribed and assessed through the ~350µm thick cladding layer at various points across the flat fibre width.

For this work, fluence matched 1.5 mm long Bragg gratings were fabricated with periods of 529.37nm. Characterisation of the gratings followed the procedure described in Chapter 7. The reflection spectrum of the first ever demonstration of Bragg gratings in the flat fibre sample with a peak wavelength of 1555.38nm and a FWHM bandwidth of ~0.2nm is shown in Fig. 9.10. To successfully define gratings using the DGW technique places a stringent need for the core layer to be flat so as to ensure that the beams overlap throughout the duration of grating writing. Despite the 'bean-shaped' profile of the sample, the fact that gratings have been successfully demonstrated leads us to believe that the core layer of the sample is flat along the direction of propagation. The inset shows the grating reflection and the ASE spectrum from the source.

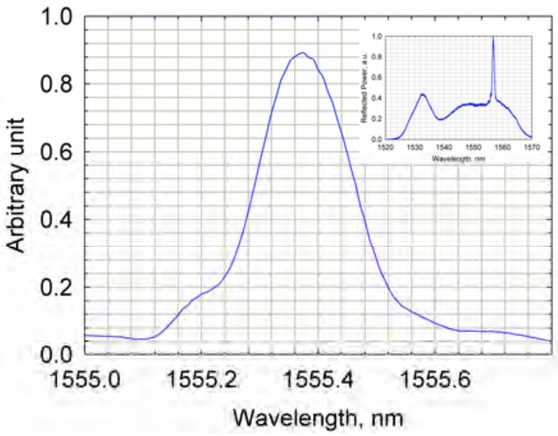

Figure 9.10 First demonstration of Bragg reflection in a flat fibre sample. The inset shows the ASE spectrum of the input light and the Bragg gratings reflection.

Following the successful demonstration of Bragg gratings, we then proceeded to define a series of identical gratings similar to the one above along the cross sectional width of a different flat fibre sample. This would allow the determination of lateral surface uniformity of the flat fibre core. The gratings were spaced 100µm apart from each other. Variations in the thickness of the sample (in cross section) will be reflected in the form of

Bragg wavelength shift. This is because layer thickness influences the effective index of a waveguide in a multi-layered sample such as the ones in this experiment. A change in effective index would result in a shift in Bragg centre wavelength. The variation of effective index across the cross section of the sample, and the approximate location of each grating is shown in Fig. 9.11. Note that gratings 6 and 7 display multi-mode behaviour which can be attributed to the increase in layer thickness as we approach the edge of the sample, enabling higher modes to be supported.

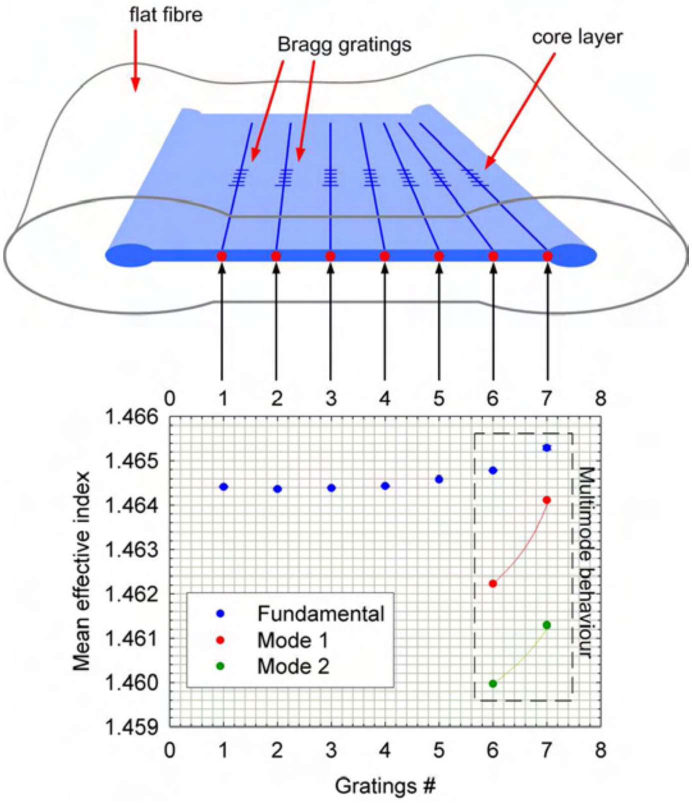

Figure 9.11 Mean effective refractive index variation across the cross section of the sample core layer. Gratings 6 and 7 exhibit multi-mode behaviour as the core layer thickness increases approaching the edge (solid lines are for indicative purpose only).

The thickness variation was estimated by means of a BPM mode solver (RSoft Beamprop). The core layer thickness is 6µm with 0.4, 0.9 and 1.7µm increase at positions 5, 6 and 7 respectively.

Finally, the birefringence of the sample was assessed by successively launching TE and TM polarised light into each of the gratings, and subsequently using data from the fundamental mode reflection spectra. The sample exhibits a mean birefringence of 3.3×10^{-4} as shown in Fig. 9.12. The large error displayed by grating 7 is probably due to its multi-mode behaviour and as such, the spectrum obtained from this grating is very sensitive to launch conditions. The low birefringence of the sample is believed to be mainly due to the lack of inherent inter-layer stress caused by variation in thermal expansion coefficients as in the case of typical 3-layer silica-on-silicon samples. We believe that this birefringence could be reduced with further optimisation of the fabrication process.

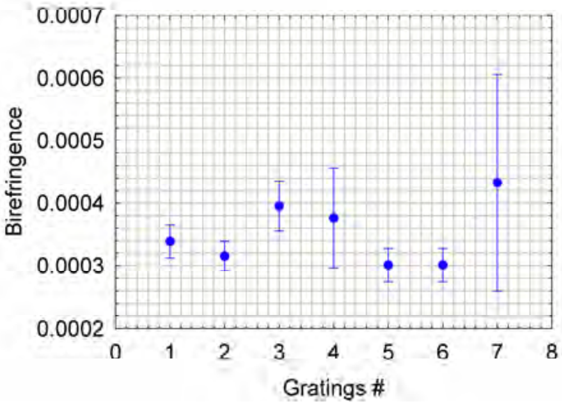

Figure 9.12 Birefringence of the flat fibre core layer with mean birefringence of ~3.3×10^{-4}.

The low birefringence and flat core layer of the flat fibre, coupled with the ability to fabricate long lengths of the sample with high levels of photosensitivity, makes this technology a promising platform for future high density integrated optical devices that would find applications in sensing and distributed processing for example.

9.6 Summary

Flat fibre has been demonstrated as a novel hybrid format that combines the advantages of existing low-cost fibre drawing with the functionality of planar lightwave circuits. Successful demonstration of straight channels, y-splitters and Bragg gratings led us to believe that the technology has potential for practical applications in the future. As mentioned at the beginning of the chapter, most of the initial experiments performed were geared towards proving the feasibility of the technology rather than the more ideal optimisation studies.

The ability to define Bragg gratings across the cross section of the sample allowed the determination of both core uniformity and birefringence. This also proves that the core layer of the sample is sufficiently flat, highlighting the potential of the substrate for integrated optics applications.

There are of course, a number of issues to be explored. Work in reducing the propagation loss of the substrate, by addressing both the optimal fluence values and the elimination of the observed ‘layer boundary’ is already underway. The usefulness of Bragg gratings in determining important substrate parameters was also demonstrated in this chapter and the development of grating based devices such as evanescent field sensors is planned.

In the longer term, work in optimising preform and drawing parameters to produce thinner, flatter, and more flexible substrates is crucial. Incorporation of active ions into the fibre composition, a process well established in MCVD, will be explored to provide active optical functions such as lasing and amplification in these materials. Improvement of the fabrication process, geared towards mass production, including the incorporation of higher levels of germanium into the core, and parallel UV writing, must also be considered.

References:

[1] D. Harwood, "Fabrication of planar substrate by blow moulding a circular tube into a facetted mould," Patent no: GB2369820, UK Patent Office, 2002.

[2] G. D. Emmerson, "Novel direct UV-written devices," PhD thesis, University of Southampton, 2003.

[3] S. R. Nagel, J. B. MacChesney, and K. L. Walker, "Overview of the modified chemical vapor deposition (MCVD) process and performance," *IEEE Journal of Quantum Electronics*, vol. QE-18, pp. 459-476, 1982.

Chapter 10

Conclusions & Future Work

During my PhD, I have demonstrated the following:

i) Small angle (0.8°-5°) direct UV-written X-couplers having maximum and minimum coupling ratios of 95% (±0.8%) and 1.9% (±1%) respectively. The structures also display very low polarisation and wavelength dependence. Typical excess loss of 1.0dB (±0.5dB) was recorded. Device modelling using BPM and an analytical model showed good agreement with experimental results over a broad crossing angle and wavelength range. The above performances were possible due to the ability to fabricate X-couplers with a raised waist index. Using UV writing also meant that the structures are not susceptible to issues relating to under-etching and step coverage. To highlight the versatility of the UV writing approach further, I have presented a study of 2° X-couplers with 20% coupling ratio tuning via refractive index asymmetry, attaining 50:50 power splitting at 1550nm. The devices showed less than 5% coupling ratio variation over 30nm in the C-band and <0.7dB polarisation dependent loss. Finally, I have also quantified the effect of UV multi-exposures through the proximity effect investigation. Photosensitivity increase is evident with initial exposures up to two waveguide widths away, with a maximum index increase of $1.05\text{x}10^{-3}$ at 0µm spacing. Using a set of three gratings overcomes difficulties associated with power coupling between two closely spaced waveguides. The study also supported earlier assumptions made during the simulation of the raised waist index X-couplers, with normalised waist index profile height ranging from 1.10 to 1.25.

ii) A liquid crystal-based integrated optical device with >140GHz electrical tuning for potential applications in dynamic optical networks. Bragg wavelength tuning covering five 25GHz-spaced WDM channels has been achieved with 170V (peak-to-peak) sinusoidal voltages applied across electro-patterned ITO-covered glass electrodes placed 60µm apart. This tunability range was limited only by the initial grating strength and supply voltage level. We also observed distinct threshold behaviours resulting in a hysteresis in the tuning curve for both TE and TM input light. The secondary threshold, which takes place at higher voltages during the increasing voltage sequence, has never been reported before. Following a separate experiment, it is believed that the threshold points are related to the formation and bleaching of disclination defects. Preliminary thermal investigation results do not point to heating effects causing the observed behaviour. One issue still remains regarding the similar tuning behaviour displayed by both TE and TM polarised light, both shifting towards shorter wavelengths.

iii) UV writing into a novel flat fibre substrate, demonstrating the potential of the substrate for applications in integrated optics. I have successfully UV-written single channel waveguides, y-splitters and Bragg gratings into a substrate with ~350μm cladding layer thickness. Utilising a series of Bragg gratings enabled assessment of the core layer uniformity and birefringence. A cut-back propagation loss measurement was also conducted.

Finally, I have also undertaken the task of upgrading the in-house FHD system here in the ORC, and performed some deposition work in the Photonics Laboratory in the University of Malaya, Malaysia.

10.1 Future Work

There are of course a number of additional investigations to extend the work presented in this thesis. Among them are:

i) Sample development: the final stages of the procurement of a new FHD system are under way. Once the system is commissioned, an investigation into selective area solution doping of silica samples should re-commence. This, coupled with the current effort in producing phase-shifted Bragg gratings by Mario Ramirez (a group member), can lead to the demonstration of the first UV-written distributed feedback (DFB) laser.

We have also recently formed collaboration with a research group in Spain (led by Dr. Daniel Jaque) to study the accurate profiling of the index structure of our samples. Such accurate index profiling will be instrumental in increasing the accuracy of simulated waveguide behaviours. The method utilised to obtain such data is a combination of confocal microscopy and micro-luminescence imaging [1]. Preliminary results are shown in Fig. 10.1. What is interesting about these results is the existence of significant levels of green luminescence emitted from the UV beam path through the silica layers, except where the waveguide is, and this requires further investigation (shown in Fig. 10.1(b)).

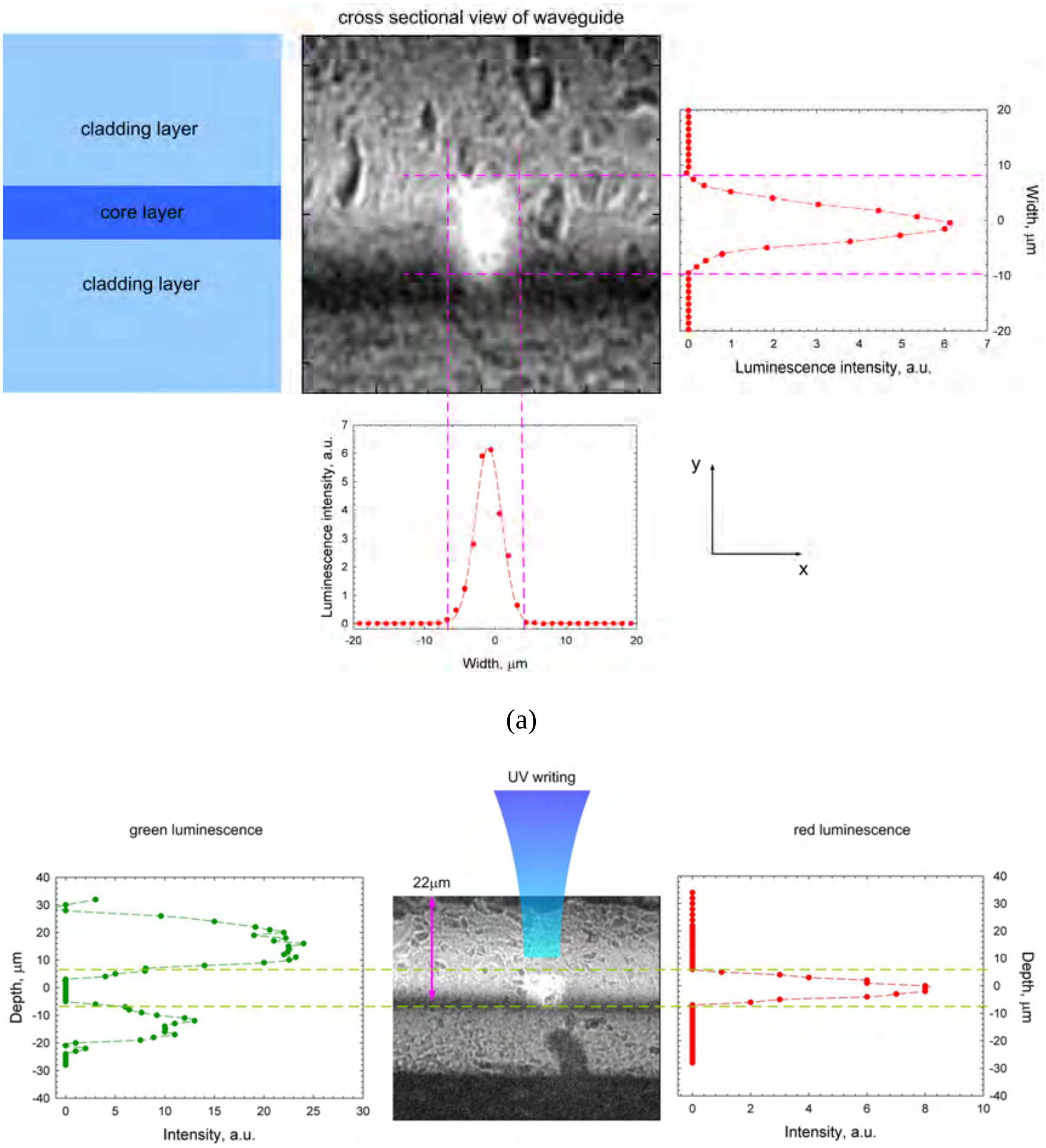

(a)

(b)

Figure 10.1 (a) Waveguide dimensions generated from red luminescence study, (b) detection of green and red luminescence that complement each other along the UV beam path.

To complement the results obtained from the technique above, an investigation into the ~400nm luminescence, emitted upon irradiation of UV light, is also beneficial. Prior observations of different samples showed that some displayed a delay before the onset of such luminescence.

ii) X-couplers: At the time of writing this thesis, a number of experiments, based on the use of these X-coupler structures, are being conducted. These include novel devices such as the ‘bubble switch’ and distributed stress/strain sensors. The schematic illustration of the two proposed devices is shown in Fig. 10.2.

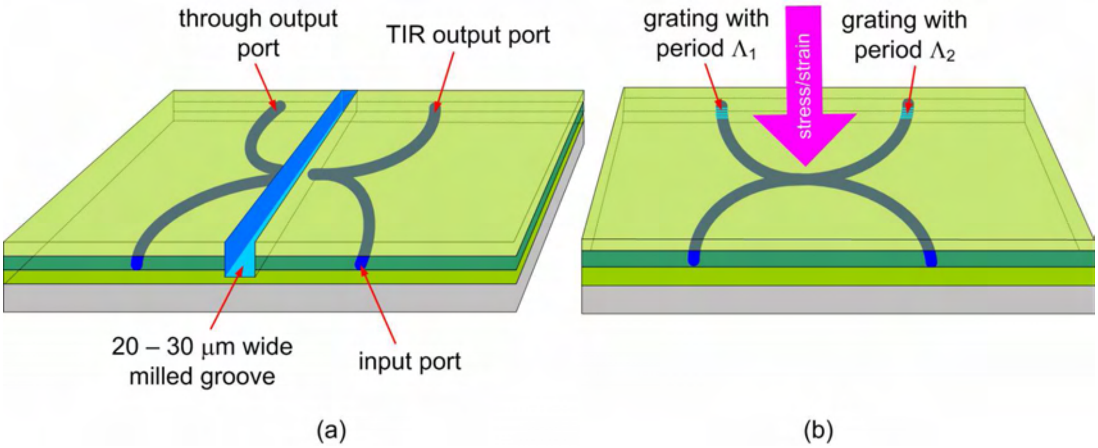

Figure 10.2 (a) Bubble switch architecture employing X-coupler and groove geometry. The idea is to be able to switch the output of the X-coupler by inserting substances with various refractive index values into the groove, thus controlling the X-coupler waist index. (b) A distributed stress/strain sensor where the peak Bragg wavelength (and possibly the reflection amplitude) of the gratings is modified by applying force onto the waist region of the X-coupler.

In the ‘bubble switch’ approach, we will attempt to prove the ability to switch light from one X-coupler output port to another by modifying the critical angle, θ_c of the light incident onto the novel groove structure. In theory, this could be achieved by filling the groove with a material having a larger refractive index (n_{mat}) compared to air ($n_{mat} > 1$). Successful implementation of such device could prove useful in dynamic, reconfigurable networks.

For the distributed sensor prototype, by applying stress/strain onto the X-coupler waist, it is hoped that a change in coupling ratio would take place, and this will be revealed by the changing reflection amplitudes of the Bragg gratings.

A tunable X-coupler architecture is also currently being investigated. In this case, the overclad layer covering the X-coupler waist is etched away and replaced by an anisotropic material such as liquid crystal, gaining the ability to modify the waist index, hence the capability to tune the coupling ratio behaviour.

iii) Tunable Bragg gratings: the most pertinent task is in explaining the anomaly in the Bragg peak shift displayed by both TE and TM polarised light. To this end, part of the effort planned is in the simulation of field lines across the electrodes. In addition to this, design of a new device with a more uniform field across the sample is also beneficial. The ability to utilise disclination defects in demonstrating a bi-stable device is also under way. Apart from these, a larger tuning range is targeted by use of a voltage supply having larger output capabilities. Use of apodised gratings, recently demonstrated by James Gates (a group member), would also be useful in allowing better Bragg peak resolution.

iv) The flat fibre: as mentioned in the beginning of the chapter on flat fibre, most of the results presented in this thesis are geared towards first proof-of-principle rather than optimisation. We were able to fabricate more samples recently, allowing work in determining the optimised fluence values, and effect of hydrogen loading. At the same time, etching of the cladding layer of a flat fibre sample containing Bragg gratings in order to demonstrate sensing capabilities is also planned. In terms of fabrication, a flatter, more flexible sample with higher germanium content would lead to the demonstration of a fully flexible distributed sensor, the conceptual schematic of which is shown in Fig. 10.3.

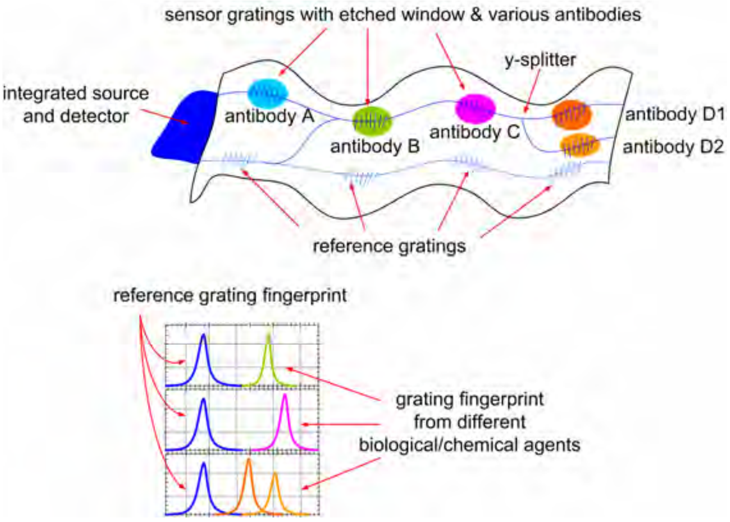

Figure 10.3 Conceptual depiction of a fully flexible flat fibre distributed sensor.

References:

[1] J. Lamella, A. Rodenas, D. Jaque, F. Jaque, G. Torhia, C. Mendez, and L. Roso, "Near field optical and micro luminescence investigations of femtosecond laser micro-structured Nd:YAG crystals," *Optics Express*, vol. 15, pp. 3285-3290, 2007.

Appendix A

ORC FHD System Upgrade

One important aspect of this project is to continue the initial work done on rare-earth solution doping of FHD samples. Following the demonstration of neodymium-doped laser by Guilhot [1], a previous group member, the next aim was to produce novel devices incorporating direct UV written structures. These plans included the development of laser with distributed Bragg reflector configuration, folded planar amplifiers with spiral waveguide topology, and lossless 1xN splitters. Moreover, further work in optimising both deposition parameters and sample dimensions to facilitate lasing with different rare-earth dopants was also planned.

Following the reallocation of laboratory space within the Mountbatten 10k clean room, it was decided in December 2003 that the in-house FHD system was to be relocated to a bigger space. This presented us with an opportunity to conduct much needed maintenance and upgrading work on the system.

A schematic of the FHD system is illustrated in Fig. A.1. The system was built primarily by S.P. Watts, a previous group member, as part of his PhD work. The construction was completed in 2002 and the system consists of a reagent supply system and the FHD rig which houses the FHD burner. The reagent supply system is housed in a glove box and O_2 gas carries the vaporised reagents into the FHD rig through a supply pipe. The reagents are contained in temperature controlled bubblers.

The composition of the sample(s) to be fabricated is determined by varying the carrier gas flow through mass flow controllers (MFC), and the vaporisation rate of the reagents via temperature control. The MFCs and temperature controllers are interfaced to a computer which used MS Visual Basic as the programming platform. A total of 11 Brooks Instruments Smart MFC model 5850S were installed in the system, daisy-chained to one another and configured to communicate via RS485[1] physical interface. RS485 interfacing allows for multi-transmitter full or half-duplex communications for up to a maximum of 32 devices. For a more extensive description of the development and the subsequent demonstration of the in-house FHD system, please refer to the thesis by Watts [2].

---

[1] The prefix 'RS' stands for Recommended Standard and the RS485 specification is published as EIA standard EIA 530 pt 87.

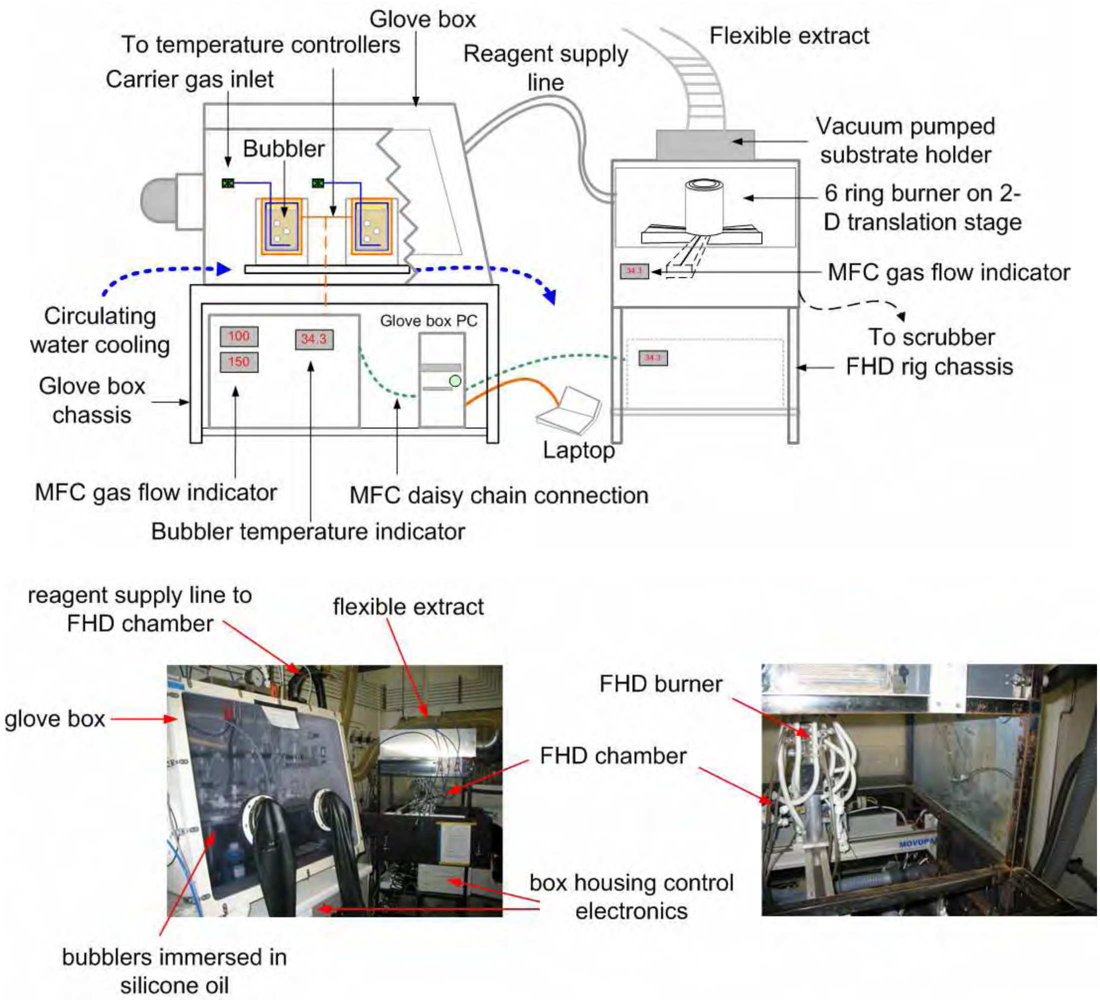

Figure A.1 Schematic representation of the FHD system.

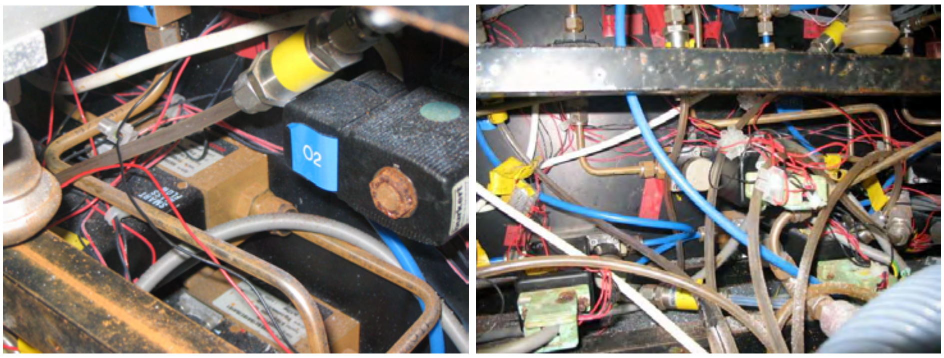

Figure A.2 Corrosion in the FHD chamber.

Once the FHD system had been relocated, the necessary fittings and a new flexible extract were installed. In addition to this, we decided to redesign the FHD deposition chamber with the focus of isolating the electronics and steel piping (where possible) from the corrosive deposition environment of the chamber. These corrosive effects are shown in Fig. A.2.

The design aims of the new control box were 1) to isolate as many electrical components and gas piping from the FHD deposition chamber and 2) to simplify wiring scheme, and 3) to position the devices (MFCs, solenoid valves) in a manner that would allow better access and understanding of the system for future maintenance purposes.

The control box would be fitted to the side of the current FHD chamber and must adhere to a maximum size due to the space constraint of the FHD system floor plan within the clean room area. To insure adherence to safety requirements, steel piping were employed for O_2 and H_2 transport whereas flexible PVC piping were used to transport N_2. Fig. A.3 illustrates the gas piping (a) and electrical layout (b) of the new control box. The new isolated FHD chamber MFC box was assembled by Niel Fagan and Trevor Austin (ORC technicians). It was then installed into the FHD system and successful communication with, and manual control of the MFCs was achieved. Some programming bugs within the original Visual Basic program were also rectified with the help of Huw Major (a group member), solving the problem relating to an earlier observed jerky stepper motor motion.

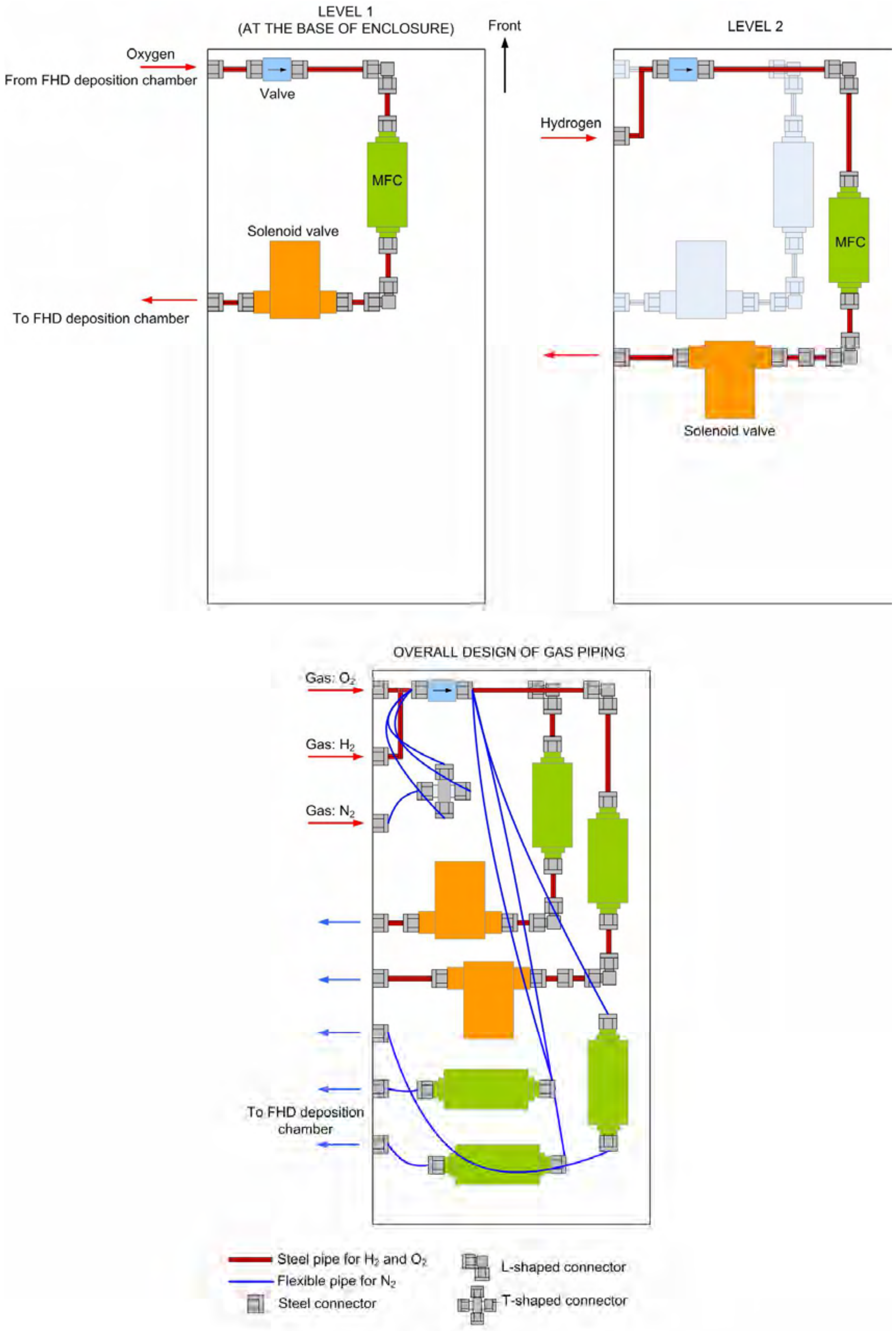
LEVEL 1
(AT THE BASE OF ENCLOSURE)
Front
LEVEL 2
Oxygen
From FHD deposition chamber
Valve
MFC
Solenoid valve
To FHD deposition chamber
Hydrogen
MFC
Solenoid valve
OVERALL DESIGN OF GAS PIPING
Gas: O_2
Gas: H_2
Gas: N_2
To FHD deposition chamber
Steel pipe for H_2 and O_2
Flexible pipe for N_2
Steel connector
L-shaped connector
T-shaped connector

(a)

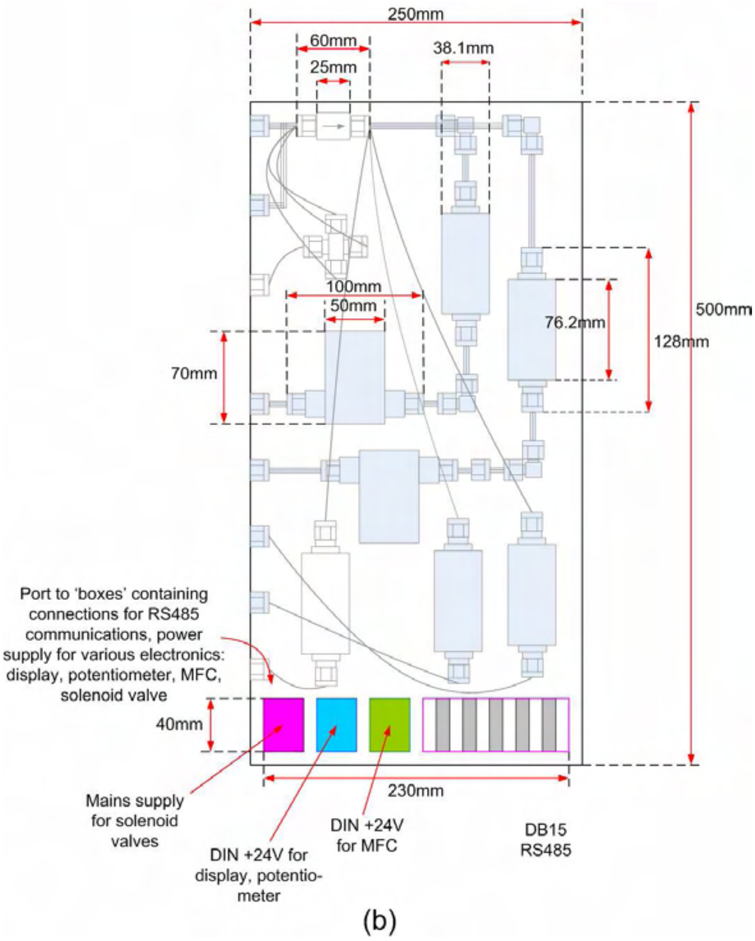

Figure A.3 Top view of gas piping and electrical connections of the new FHD chamber control box.

References:

[1] D. A. Guilhot, G. D. Emmerson, C. B. E. Gawith, S. P. Watts, D. P. Shepherd, R. B. Williams, and P. G. R. Smith, "Single-mode direct-ultraviolet-written channel waveguide laser in neodymium-doped silica on silicon," *Optics Letters*, vol. 29, pp. 947-949, 2004.

[2] S. P. Watts, "Flame hydrolysis deposition of photosensitive silicate layers suitable for the definition of waveguiding structures through direct ultraviolet writing," PhD thesis, University of Southampton, 2001.

Appendix B

FHD in Malaysia

Sufficient amounts of photosensitive silica-on-silicon samples were needed to ensure that overall progress in other aspects of this research is not disrupted while the FHD system is being upgraded. To this end, some deposition work was conducted in collaboration with the Photonics Laboratory in the University of Malaya (Malaysia) where I am currently a member of staff. I was involved in the initial procurement of the system before leaving for the ORC in October 2003.

The system was installed in August 2004 and I was invited to take part in the first few trial fabrication runs. This presented an opportunity for me to conduct some fabrication work with the aim of subsequently using the samples for UV writing work back in the ORC. I spent 4 weeks fabricating nine 4-inch silica-on-silicon samples. Out of the nine, six were consolidated using a staggered temperature ramping up technique in order to allow gradual out-gassing of volatile materials within the deposited soot.

The FHD process involved is similar to that practiced in the ORC. However, there are a number of differences in terms of choice of FHD components used and certain aspects of the processes. These include:

i. Quartz burner/torch. This would eliminate corrosion problems associated with stainless steel torch, the kind used in the FHD system here in the ORC. However, a quartz burner is susceptible to crystallisation of reagents on its walls and therefore needs frequent cleaning. Cleaning a quartz burner is tricky as it involves scraping the crystallised material off a burner wall that is fragile.

ii. Staggered ramping-up of consolidation temperature and free-cooling. A typical consolidation cycle takes 22 hours to complete resulting in a deposition limit of one deposited layer per day compared to the up to three consolidated layers per day rate of the FHD system in the ORC. Such long consolidation time results in volatilisation of deposited material, leading to visible pores on consolidated layers. This process also increases the susceptibility to crystallisation.

iii. Turn-table that could house three 4-inch silicon wafers with air-suspended wafer jack and heated at 200ºC. This prevents the usage of cleaved silicon wafers. From an experimental point of view, the inability to use cleaved silicon wafers leads to wastage and in addition to this, the long cycle time taken to produce layers means that a fabrication study takes longer to conclude compared to the same exercise performed here in the ORC.

iv. Helium gas for reagent transport due to its inert nature. In the ORC, oxygen is used as the carrier gas to increase direct oxidation efficiency.

B.1 Sample Characterisation

Refractive index measurement of the fabricated layers was done via prism coupling. For this experiment, single layers of cladding and core were deposited onto silicon substrates and measurements were carried out using a commercial equipment. The results yielded the following: average underclad refractive index of 1.445 and thickness of 22μm. The corresponding values for the core layer are 1.451 and 7.5μm respectively.

A total of nine 3-layer samples were fabricated and all of them contained visible pores and some displays dust-like features. These defects are shown in Fig. B.1 and there are a number of possible reasons that might cause such features. Due to the slow ramping of consolidation temperature and the free cooling of consolidated layers, the possibility of out-gassing of volatile materials, especially phosphorous and boron, and also crystallisation is high. Dust-like features are also indicative of contaminants acquired during the whole deposition exercise. Some of these features show propagation through all three consolidated layers as depicted by Fig. B.1(d).

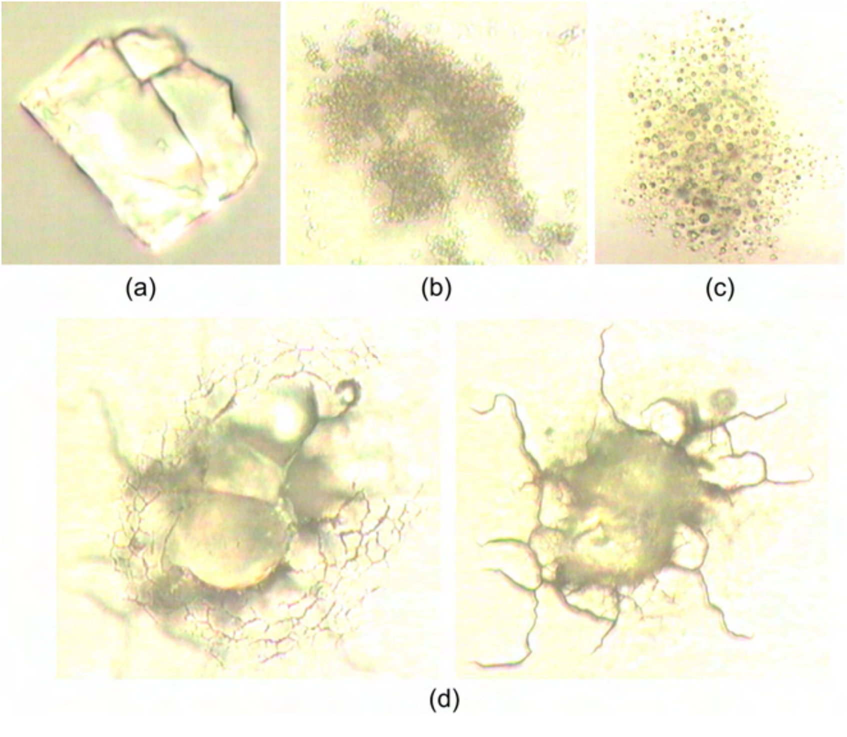

Figure B.1 Various defects/pores found on the fabricated 3-layer samples.

As this was a new source of material, and had not previously been used for UV writing, a fluence test was conducted to assess the photosensitivity of the samples. Fluence, F which is an expression for the energy exposed to the sample during the UV writing process, given by:

$$F = \frac{I_{UV}.a}{v_{scan}} \qquad [B.1]$$

where F is the fluence (kJ cm^{-2}), I_{UV} is the average power density in the writing spot (kJ cm^{-2} s^{-1}), a is the writing spot diameter (cm) and v_{scan} is the stage translation speed (cm s^{-1}). Two sets of straight channels were written at different fluence values by varying the stage translation speed during the writing process. The 4-inch samples were diced into smaller ones measuring typically 15x20mm^2 and their end facets were polished to optical quality before being hydrogen loaded at 150bar prior to UV writing. The straight channels were written 1mm apart to prevent any coupling and proximity[1] effects.

The resulting channel numerical aperture (NA) was measured using the set up in Fig. B.2(a). Numerical aperture is a measure of the light guiding capability of an optical waveguide. The higher the NA, the higher the light confinement is. NA is given by $(n^2_{core} - n^2_{cladding})^{1/2}$ where n_{core} and $n_{cladding}$ are the core and cladding refractive index respectively.

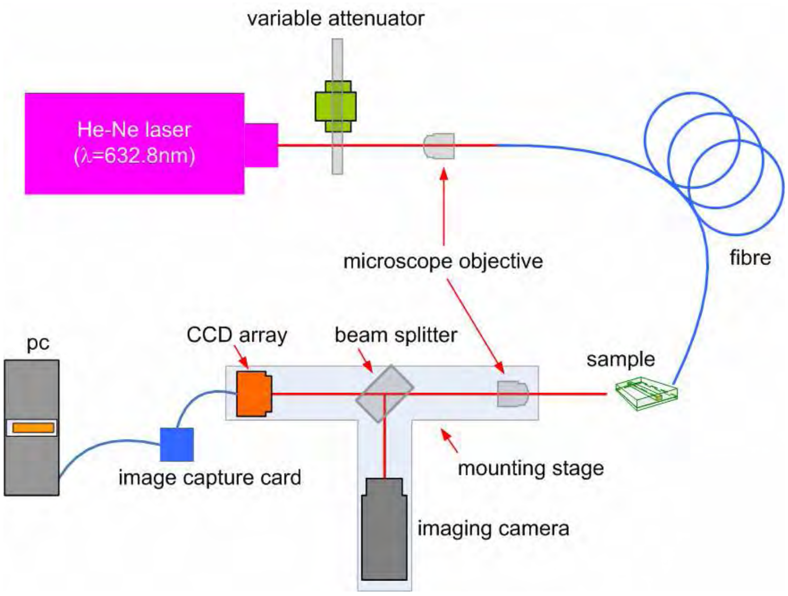

(a)

---

[1] Proximity effect is the increase of photosensitivity within the vicinity of earlier written channels. This is discussed further in Chapter 7.

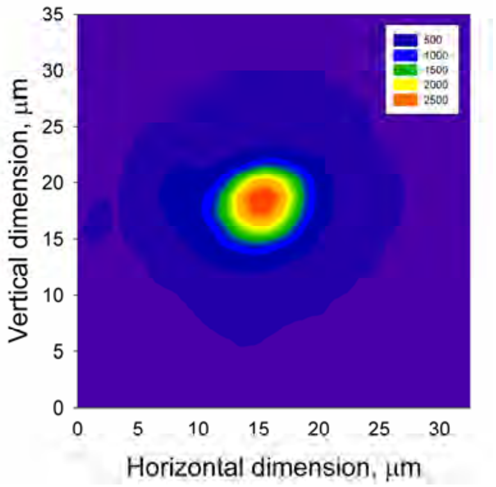

(b)

Figure B.2 (a) HeNe set up for NA measurements and mode profiling, and (b) shows a typical mode profile of a waveguide with the data generated by the HeNe curve fitting program (the colours represent intensity levels).

The set up to measure NA employs a CCD array that could be translated relative to the output facet of the sample and used to capture light intensity output from a particular channel. Measuring the divergence of the output light in relation to the distance of the CCD array from the sample output facet determines the acceptance angle and hence, the channel NA. The camera facilitates optimal alignment of the launch fibre to the input facet of the channel being characterised. The intensity of the captured light is fed into imaging software that outputs data into formatted, scaled tables for subsequent analysis. Repeat measurements were taken to allow for errors.

Fig. B.3 depicts the numerical aperture of channels written at various fluence levels. The compound effects of both vertical and horizontal numerical aperture is expressed in quadrature i.e. $NA_{mean} = \sqrt{(NA^2_{horizontal} + NA^2_{vertical})}$. It is worth pointing out that an index structure already existed prior to UV writing due to non-index matched[2] layers design and as such, $NA_{horizontal}$ is usually a better indicator of photosensitivity.

---

[2] Index matched FHD samples have the same refractive index values (within 10^{-4}) for all three layers – overclad, core and underclad – for a given wavelength. As such, there is no index structure prior to UV writing. Using such samples for UV writing would lead to a symmetrical index increase, hence mode profile, improving coupling to fibres efficiency.

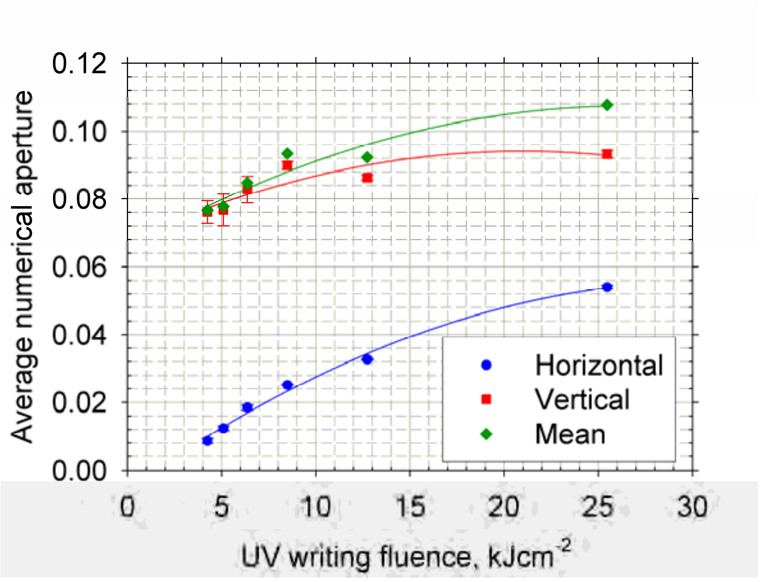

Figure B.3 Numerical aperture of UV written channels with increasing UV writing fluence levels (solid line: curve of best fit).

Increase in NA with fluence is expected and the levelling off of the curves suggests saturation effects. As can be seen from the graph, NA values are dominated by the vertical index structure. A maximum $NA_{horizontal}$ of 0.054 for fluence as high 25.5kJcm^{-2} suggest low photosensitivity. This is further reinforced by the low photoluminescence observed during UV writing (see Chapter 4). As such, higher fluence must be used in defining strong channel waveguides and due to hydrogen out-diffusion, the maximum number of structures that could be UV written per sample is limited.

Fire Related Issues

The Mountbatten fire of October 30th 2005 destroyed my office, the in-house flame hydrolysis deposition system, and the characterisation set-ups in lab 1083.

The original objectives of this PhD were as follows:

i) To undertake investigation into high density integrated devices. The goal was to increase the functionality of a silica-on-silicon chip while maintaining its current form factor.

ii) To continue the progress made in the development of rare-earth doped devices via solution doping. Specifically, a method in achieving selective area doping, was to be investigated.

iii) Following on from ii), fabrication of lasing, and amplifying architectures incorporating direct UV-written structures were to be pursued. Investigations into novel topologies such as spiral erbium-doped waveguide amplifiers, and distributed Bragg reflector architectures that are based on direct UV-written planar Bragg gratings were planned.

Structures involving folded architectures (spirals for example), and high density devices in general, inevitably contain crossing waveguides and bends. As such, characterisation of these structures is pertinent to facilitate optimal device performance. In addition to this, in keeping with the progress made by the group here in the Optoelectronics Research Centre, the overall objective of fabricating a number of novel grating based devices was also important.

Progress in some of the objectives listed above was prevented due to the lack of clean-room facilities, a direct consequence of the Mountbatten fire. My research direction was adapted to cope with this situation, as reflected by the work presented in this thesis.

The people

and many more who are not in this collage..

List of Publications

Journal Papers

1. F.R.M. Adikan, J.C. Gates, H.E. Major, C.B.E. Gawith, P.G.R. Smith, A. Dyadyusha, M. Kaczmarek, I.J.G. Sparrow, and G.D. Emmerson, ‘100 GHz electrically tunable liquid crystal Bragg gratings for dynamic optical networks’, Optics Letters, vol. 32, no. 11, pp. 1542-1544, 2007.

2. A.S. Webb, F. R. Mahamd Adikan, J. K. Sahu, R.J. Standish, C. B. E. Gawith, P.G.R. Smith, and D.N. Payne, 'Fabrication of MCVD Planar Substrates for UV-Written Waveguide Devices', Electronics Letters, vol. 43, no. 9, pp. 517-519, 2007.

3. F.R. Mahamd Adikan, J.C. Gates, C.B.E. Gawith and P.G.R. Smith, “Coupling ratio tuning of direct UV-written X-couplers for cascaded power splitters in WDM networks”, Electronics Letters, vol. 42, no. 24, pp.1397-1398, 2006.

4. F.R. Mahamd Adikan, C.B.E. Gawith, P.G.R. Smith, I.J.G. Sparrow, G.D. Emmerson, C. Riziotis and H. Ahmad, “Design and demonstration of direct UV-written small angle X-couplers in silica-on-silicon for broadband operation”, Applied Optics, vol. 45, no. 24, pp. 6113-6118, 2006.

Conference

1. D. Jaque, F.R. Mahamd Adikan, J.C. Gates, C.B.E. Gawith, P.G.R. Smith, 'Imaging of single-step UV-laser-written channel waveguides by confocal micro-luminescence', Conference on Laser Ablation (COLA) 2007, Tenerife, Spain.

2. P.G.R. Smith, C.B.E. Gawith, J.C. Gates, D. Kundys, F.R. Mahamd Adikan, C. Holmes, H.E. Major, M. Garcia-Ramirez, B.D. Snow, ‘UV written waveguide devices - Bragg gratings and applications in sensors’, ICAMN 2007 Langkawi, Malaysia 29 May - 1 Jun 2007.

3. B.D. Snow, F.R.M. Adikan, A. Dyadyusha, J.C. Gates, H.E. Major, C.B.E. Gawith, M. Kaczmarek, and P.G.R. Smith, "Towards high-speed liquid crystal electrically tunable planar Bragg gratings for integrated optical networks", BLCS 2007 Sheffield 28-30 Mar 2007.

4. F.R.M. Adikan, J.C. Gates, B.D. Snow, A. Dyadyusha, H.E. Major, C.B.E. Gawith, M. Kaczmarek, and P.G.R. Smith ,"100 GHz electrically tunable planar Bragg gratings via liquid crystal overlay", CLEO-Europe/IQEC 2007 Munich 17-22 Jun 2007.

5. F.R.M. Adikan, J.C. Gates, C.B.E. Gawith, and P.G.R. Smith, "Quantitative determination of photosensitivity proximity effects in multi-exposure direct UV writing for high density integrated optics", CLEO-Europe/IQEC 2007 Munich 17-22 Jun 2007.

6. J.C. Gates, F.R.M. Adikan, C. Holmes, C.B.E. Gawith, and P.G.R. Smith, "Lateral groove geometry for planar UV written evanescent devices - new flexibility new devices", CLEO-Europe/IQEC Munich 17-22 Jun 2007.

7. F.R. Mahamd Adikan, J.C. Gates, A.S. Webb, H.E. Major, C. Holmes, M. A. G. Ramirez, B. D. Snow, D. O. Kundys, C.B.E. Gawith, and P.G.R. Smith, "Recent developments in direct-UV-written planar waveguides, gratings, sensors, and substrates", ECIO 2007, April 2007, Denmark.

8. J. Gates, C. Holmes, F.R. Mahamd Adikan, C.B.E. Gawith, and P.G.R. Smith, "New geometry for planar UV written refractive index sensors", SPIE Europe Optics and Optoelectronics Prague 16-20 Apr 2007.

9. F.R. Mahamd Adikan, J.C. Gates, H.E. Major, C.B.E. Gawith, P.G.R. Smith, A. Dyadyusha, M. Kaczmarek, and I.J.G. Sparrow, "100 GHz electrically tunable planar Bragg grating via nematic liquid crystal overlay towards reconfigurable WDM networks", SPIE Europe Optics & Optoelectronics Conference Prague 16-20 Apr 2007.

10. C.B.E. Gawith, A.S. Webb, F.R. Mahamd Adikan, J.C. Gates, J.K. Sahu, and P.G.R. Smith, "Flat fiber - the flexible format for distributed lab-on-a-chip", SPIE Europe Optics & Optoelectronics Conference Prague 16-20 Apr 2007.

11. F.R. M. Adikan, A.S. Webb, R.J. Standish, J.K. Sahu, C. Holmes, H.E. Major, D. Kundys, J.C. Gates, C.B.E. Gawith, P.G.R. Smith, and D.N. Payne, “Sense & Fibrelity: Next Generation Optical Biosensors”, Presentations at the House of Commons in 2006 by Britain’s Early-stage Engineers on UK Engineering Research and R&D (***Winner of the Section Prize for Best Engineering Research***).

12. F.R. Mahamd Adikan, A.S, Webb, C.B.E. Gawith, J.C. Gates, J.K. Sahu, P.G.R. Smith, and D.N.Payne, “First Demonstration of Direct UV written Bragg Gratings in Collapsed Fibre Planar Samples”, European Conference on Optical Communications 2006 (ECOC2006), Cannes We3.P.69.

13. R. Adikan, C. Holmes, H. Major, C.B.E. Gawith, J. Gates, H. Ahmad, and P.G.R. Smith, “Direct UV written optical planar devices”, Malaysian Research Group International Conference 2006 (MRG-IC2006) Manchester 19-21 Jun 2006.

14. F.R. Mahamd Adikan, C.B.E. Gawith, P.G.R. Smith, I.J.G. Sparrow, G.D. Emmerson, and C. Riziotis, “Demonstration and Accurate Beam Propagation Method Modeling of Direct UV Written Shallow Angle X-couplers,” CLEO/QELS 2006 Long Beach, California May 21-26 2006.

15. F.R. Mahamd Adikan, C.B.E. Gawith, P.G.R. Smith, I.J.G. Sparrow, G.D. Emmerson, and C. Riziotis, "Single-step Fabrication of Raised Index X-Couplers via Direct UV Writing", OFC 2006 Anaheim, California 5-10 Mar 2006.

16. P.G.R. Smith, G.D. Emmerson, C.B.E. Gawith, S.P. Watts, R.B. Williams, D.A. Guilhot, I.J.G. Sparrow, and F.R. Mahamd Adikan, “All-UV written integrated glass devices including planar Bragg gratings and lasers,” ICOL 2005 Uttaranchal India 12-15 Dec 2005 IT-FIO-4 (Invited).

17. F.R. Mahamd Adikan, I.J.G. Sparrow, C.B.E. Gawith, G.D. Emmerson, H. Ahmad, and P.G.R. Smith, “Small-angle (<5°) direct-UV-written crossed-waveguide on silica-on-silicon with potential for power switching applications’” CLEO/IQEC-Pacific Rim 2005 Tokyo 11-15 Jul 2005.

18. F.R. Mahamd Adikan, I.J.G. Sparrow, G.D. Emmerson, C.B.E. Gawith, P. Poopalan, W.Y. Chong, T. Subramaniam, H. Ahmad, and P.G.R. Smith, “Direct UV writing for channel definition on FHD Silica-on-Silicon”, Semiconductor and Integrated Optoelectronics (SIOE '05), Cardiff March 21-23 2005.

19. P.G.R. Smith, G.D. Emmerson, C.B.E. Gawith, S.P. Watts, R.B. Williams, D.A. Guilhot, I.J.G. Sparrow, and F.R. Mahamd Adikan, “All-UV written integrated glass devices including planar Bragg gratings and lasers”, XX International Congress on Glass (ICGXX), Kyoto 26 Sep – 1, Oct 2004 90026 (Invited).